



Climbing to the Top of the ATLAS 13 TeV data

The ATLAS Collaboration

The large amount of data recorded with the ATLAS detector at the Large Hadron Collider, corresponding to 140 fb^{-1} of pp collisions at a centre-of-mass energy of $\sqrt{s} = 13 \text{ TeV}$, has brought our knowledge of the top quark to the next level. The measurement of the top–antitop quark pair-production cross-section has reached a precision of 1.8% and the cross-section was measured differentially up to several TeV in several observables including the top-quark transverse momentum and top-quark-pair invariant mass. Single-top-quark production was studied in all production modes. Rare production processes where the top quark is associated with a vector boson, and four-top-quark production, have become accessible and precision measurements of several of these processes have reached cross-section uncertainties of around 10% or smaller. Innovative measurements of the top-quark mass and properties have also emerged, including the observation of quantum entanglement in the top-quark sector and tests of lepton-flavour universality using top-quark decays. Searches for flavour-changing neutral currents in the top-quark sector have been significantly improved, reaching branching-ratio exclusion limits ranging from 10^{-3} to 10^{-5} . Many of these analyses have been used to set limits on Wilson coefficients within the effective field theory framework.

Contents

| | | |
|-----------|---|-----------|
| 1 | Introduction | 3 |
| 2 | Event selection, statistical analysis and systematic uncertainties | 5 |
| 2.1 | Data samples | 5 |
| 2.2 | Object reconstruction and event selection | 5 |
| 2.3 | Statistical methods | 6 |
| 2.4 | Systematic uncertainties and Monte Carlo modelling | 7 |
| 3 | Top-quark pair production | 9 |
| 3.1 | Inclusive top-quark pair cross-section measurements | 10 |
| 3.2 | Differential top-quark pair cross-section measurements | 13 |
| 3.3 | Studies of b -jet production in top-quark-pair events | 14 |
| 4 | Single-top-quark production | 15 |
| 4.1 | Measurements in the t -channel | 16 |
| 4.2 | Measurements in the tW channel | 17 |
| 4.3 | Measurement in the s -channel | 19 |
| 5 | Associated production of top quarks | 20 |
| 5.1 | Top-quark production in association with a W or Z boson | 21 |
| 5.2 | Top-quark production in association with a photon | 24 |
| 5.3 | Four-top-quark production | 25 |
| 6 | Top-quark mass | 27 |
| 6.1 | Direct top-quark mass measurements | 28 |
| 6.2 | Indirect top-quark mass measurements | 31 |
| 7 | Top-quark properties | 31 |
| 7.1 | Top-quark decay angular properties | 32 |
| 7.2 | Asymmetry measurements | 35 |
| 7.3 | Tests of QCD | 37 |
| 7.4 | Test of lepton-flavour universality | 40 |
| 8 | Search for flavour-changing neutral currents in the top-quark sector | 41 |
| 8.1 | Searches for top-quark FCNC processes involving a Higgs boson | 42 |
| 8.2 | Searches for top-quark FCNC processes involving neutral gauge bosons | 43 |
| 8.3 | Summary of FCNC process constraints | 46 |
| 9 | Limits on Wilson coefficients within effective field theory | 46 |
| 10 | Conclusion | 51 |

1 Introduction

The top quark is the heaviest known elementary particle, with a mass of about 172.5 GeV. Discovered at the Tevatron proton–antiproton collider at Fermilab in 1995 [1, 2], it was the subject of a large number of measurements by the ATLAS [3] and CMS [4] experiments at the Large Hadron Collider (LHC) during both the first data-taking phase called Run 1, with proton–proton (pp) collisions at centre-of-mass energies of $\sqrt{s} = 7$ and 8 TeV, and the subsequent higher-energy phase, referred to as Run 2. During Run 2, from 2015 to 2018, the ATLAS detector collected data from $\sqrt{s} = 13$ TeV pp collisions with a total integrated luminosity of 140 fb^{-1} . This dataset corresponds to about 100 million produced top-quark pairs. With this unprecedented integrated luminosity and pp collision energy, the ATLAS Collaboration has had the opportunity to intensify its efforts to understand the nature of the top quark.

At hadron colliders, the top quark can be produced either via the strong interaction, as quark–antiquark pairs ($t\bar{t}$), or through electroweak (EW) processes, giving rise to single-top-quark events. Strong $t\bar{t}$ production can be initiated, at leading order (LO) in QCD, by either gluon–gluon fusion processes or quark–antiquark annihilation processes (see Figure 1), with the former dominating in pp collisions at LHC energies. Single top quarks are produced mostly through three modes, which are labelled according to the virtuality of the W boson: the so-called t -channel, s -channel and tW production modes (see Figure 2). At the LHC, single top production is subdominant relative to $t\bar{t}$ production.

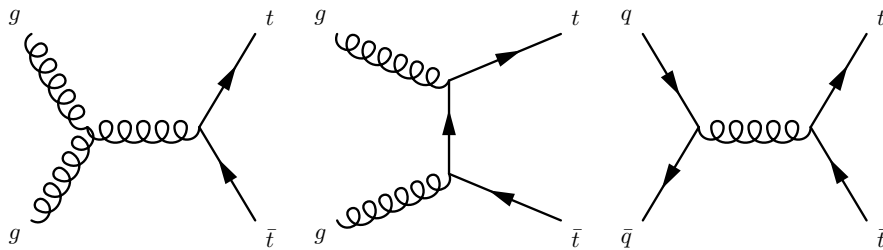


Figure 1: Representative Feynman diagrams for $t\bar{t}$ production at LO in QCD: gluon-initiated fusion in the s -channel (left) and t -channel (middle), and quark–antiquark annihilation (right).

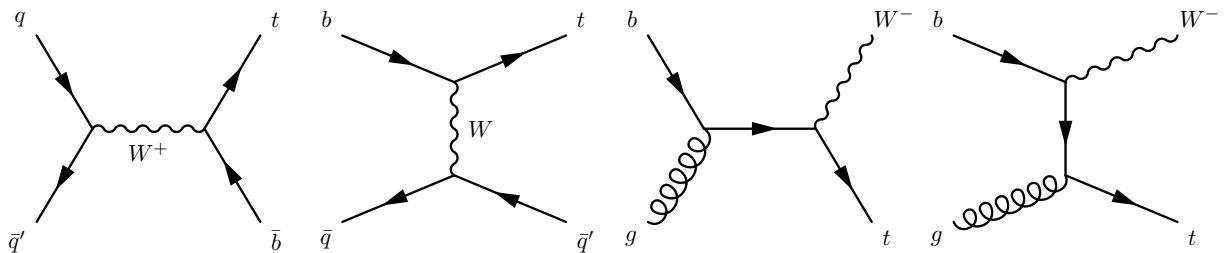


Figure 2: Representative Feynman diagrams for single top-quark production at LO: from left to right, s -channel, t -channel, and the two diagrams for the tW channel.

According to the Standard Model (SM), the top quark decays almost exclusively into a W boson and a bottom quark, b . The top-quark lifetime is shorter than the typical hadronisation time scale, so it doesn't form a bound state with other quarks. Final-state topologies in top-quark production events are then mainly

determined by the W -boson decay modes, with the b -quark manifesting itself as a hadronic jet. Top-quark pair-production events can give rise to three different types of final states. The fully hadronic final state is characterised by the production of two b -quarks and four light-flavour quarks, coming from the decays of the top quarks and W bosons respectively, typically giving rise to six hadronic jets. The dilepton final state is distinguished by two charged leptons (electrons or muons) and two undetected neutrinos produced in association with a pair of jets originating from the b -quarks (referred to as b -jets in the following). Finally, the semileptonic final state, often referred to as single-lepton or lepton-plus-jet, typically has four hadronic jets (two of which are b -jets), an electron or a muon, and a neutrino. The W -boson decay can also lead to the production of a τ -lepton that is either reconstructed through a hadronic decay or enters one of the two leptonic channels if it decays leptonically. Analogously, s - and t -channel single-top-production events can give rise to either fully hadronic or single-lepton final states, with tW -production events having dilepton final states as well.

Besides these dominant production mechanisms, pp collisions at the LHC can give rise to other processes involving the production of top quarks that were mostly not observed at the Tevatron or in Run 1. The SM predicts the production of $t\bar{t}$ pairs in association with photons, W or Z bosons, Higgs bosons or even another $t\bar{t}$ pair, while single top production can proceed via $t\gamma$, tZ or tH processes, in addition to the main modes mentioned above.

The interest in studying top-quark physics at the LHC, with the benefits brought by the Run 2 dataset's size and collision energy, is manifold. The top quark is the heaviest and most recently discovered quark. Its mass is a particularly important fundamental parameter of the SM, linked to its vacuum stability [5, 6], and the LHC is the best place to measure it precisely. Moreover, precise measurements of its couplings, as well as its production and decay properties, are essential in order to fully establish its nature and its role in the SM. In addition, a number of proposed theories beyond the SM (BSM theories) predict new or modified top-quark production and decay mechanisms, resulting in altered kinematic distributions or even significant enhancements in the rates of very rare processes, such as those mediated by a flavour-changing neutral current (FCNC). In the SM, FCNC decays such as $t \rightarrow qZ$, $t \rightarrow q\gamma$ or $t \rightarrow qH$ (q being a first- or second-generation up-type quark: u or c) are highly suppressed and below the experimental sensitivity. Direct searches for BSM phenomena are described in Ref. [7].

Experimentally, the identification and study of top-quark events with the ATLAS experiment relies not only on the reconstruction of hadronic jets, and identifying those coming from the fragmentation of b -quarks through dedicated b -tagging algorithms, but also on the identification of electrons and muons, and the measurement of the missing transverse momentum associated with the presence of undetected neutrinos. For the all-hadronic final states, which take advantage of the larger hadronic branching fraction of the W boson but are more challenging in terms of background contamination, combinations of multijet and b -jet triggers [8–10] are used, while for channels with at least one electron or muon, the online event selection is based on single-lepton triggers [11, 12]. High-performance reconstruction and identification algorithms for all these physics objects are essential ingredients for maximising the precision of top-quark measurements. In Run 2, the performance of these algorithms was significantly improved relative to Run 1, thanks to detector upgrades as well as new identification algorithms and calibration techniques. In particular, the addition of a new innermost detector layer, the Pixel detector's Insertable B-Layer (IBL) [13, 14], together with the adoption of new machine-learning (ML) techniques, allowed the b -tagging performance to be dramatically improved (around 10% efficiency increase for b -jets at the same light-flavour-jet rejection rate) [15, 16]. On the other hand, new calibration techniques allowed the systematic uncertainties associated with c -jet and light-flavour-jet rejection to be reduced [17, 18]. Similarly, improvements in the jet reconstruction algorithms and energy calibration (with about a factor of two reduction in the jet energy

scale’s uncertainty) [19–21] contributed to the overall gain in measurement precision, beyond that coming from the increase in sample size due to the larger integrated luminosity and production cross-sections. At the same time, improved trigger algorithms, allowing the single-lepton transverse momentum thresholds to be kept at reasonable levels (below 27 GeV) despite the increase in instantaneous luminosity, as well as the introduction of new techniques to mitigate the stronger impact from additional pp collisions in the same or a nearby bunch crossing (pile-up), such as the so-called jet-vertex-tagger (JVT) [22], provided the means to cope with the increased pile-up activity in Run 2. Improved electron and muon identification [23–25] also provided pile-up mitigation. Finally, innovative analysis techniques, often relying on modern ML algorithms, as well as refined Monte Carlo (MC) simulation tools were gradually introduced and adopted for the top-quark measurements and searches performed over the past years.

This report is organised as follows. Section 2 describes general experimental aspects of the ATLAS Run 2 top-quark physics analyses, such as typical event and physics object selection criteria, statistical analysis techniques and systematic uncertainties. The following sections are each devoted to a particular set of measurements. Section 3 reports the $t\bar{t}$ cross-section measurements, while Section 4 describes the single-top-quark measurements. Section 5 describes the measurements of top quarks produced in association with a boson, as well as four-top-quark production. Section 6 discusses the top-quark mass results and Section 7 the determination of other top-quark properties. Section 8 presents the searches for flavour-changing neutral currents in the top-quark sector, and Section 9 presents limits on Wilson coefficients within effective field theory. Section 10 gives the conclusions of this report.

2 Event selection, statistical analysis and systematic uncertainties

2.1 Data samples

A set of early Run 2 top-quark measurements, based on the 2015 pp collision dataset and corresponding to an integrated luminosity of 3.2 fb^{-1} , were essential for validating the updated detector and software set-ups, as well as the new Monte Carlo simulation settings for the $t\bar{t}$ process and the applicability of the lepton and jet calibrations. At the completion of the 2016 pp data-taking, the integrated luminosity collected by ATLAS in Run 2 had increased by a factor of ten to 36 fb^{-1} , allowing an extensive set of new measurements in all the top-quark physics sectors. With the inclusion of the 2017 pp collision dataset, the integrated luminosity reached 80 fb^{-1} . Finally, with the addition of the data collected in 2018, the full Run 2 dataset reached an integrated luminosity of 140 fb^{-1} . The quoted integrated luminosity for measurements released earlier than December 2022 [26] is 139 fb^{-1} , and was updated to 140 fb^{-1} in accord with the final Run 2 13 TeV pp luminosity measurement [27]. This full dataset was used to produce refined results for most of the measurements.

2.2 Object reconstruction and event selection

Events containing top quarks typically produce final states including high-momentum jets, charged leptons and missing transverse momentum.

In Run 2, electrons and muons [24, 25, 28] were typically required to have a transverse momentum (p_T) exceeding a threshold between 25 and 30 GeV, and to be reconstructed within the geometrical acceptance

of the inner detector (i.e. with absolute pseudorapidity¹ $|\eta| < 2.5$). They were required to pass the identification and isolation requirements in Refs. [24, 28] to improve the rejection of misidentified hadrons faking their signatures and non-prompt leptons from hadron decays or photon conversions, as well as to ensure sufficient precision in the measurement of their energy and momentum. A multivariate discriminant was developed to further reject non-prompt leptons. This discriminant uses as input the energy deposits and charged-particle tracks in a cone around the lepton direction, as well as lifetime variables [29].

Hadronic jets were reconstructed either from calorimeter energy-deposit clusters, referred to as topological cell clusters [30], or from combined information from the calorimeters and the inner detector. The latter was assembled by a dedicated particle-flow algorithm [31] used for most of the latest measurements. The jet constituents were then clustered with the anti- k_t algorithm [32, 33], using a radius parameter $R = 0.4$, to form so-called ‘small- R jets’ (or simply ‘jets’ in the following). Kinematic requirements on such small- R jets include a minimum p_T of 20 or 25 GeV and $|\eta| < 4.5$ (although most analyses restrict jets to $|\eta| < 2.5$). A cut was imposed on the JVT output for jets reconstructed within the acceptance of the inner detector and below a p_T threshold of 60 GeV, to reduce the contamination from jets not coming from the hard interaction (pile-up jets).

In addition, analyses targeting particularly high-momentum or ‘boosted’ top quarks that decay hadronically, with decay products that are highly collimated and thus difficult to reconstruct as separate small- R jets, relied on the clustering of calorimeter energy deposits, or the reclustering of small- R jets [34], into larger-radius jets, with the R parameter typically set to 1.0. Such large- R jets were then tagged, relying on jet substructure variables, and grooming procedures based on trimming or soft-drop were applied [35–38] to mitigate the effect of pile-up and the underlying event.

To identify jets originating from b -quarks, dedicated b -tagging algorithms were implemented and calibrated. Several gradually improved implementations were used by ATLAS Run 2 analyses, all relying on ML techniques based mainly on secondary-vertex reconstruction and charged-track impact parameter measurements [15, 16]. For each tagger, a certain number of working points were defined, characterised by b -tagging efficiencies between 85% and 60% and increasing rejection power against c -jets (between 2 and ~ 40) and light-flavour jets (between 40 and ~ 1000).

Missing transverse momentum in an event could indicate the production of neutrinos, which leave no signal in the detector. It is calculated as the negative vector sum of the p_T of the reconstructed and calibrated objects in the event [39]. This sum also includes the momenta of the tracks that are matched to the primary vertex but are not associated with any other reconstructed objects.

2.3 Statistical methods

Many of the Run 2 ATLAS measurements used unfolding techniques to correct the detector-level observed distributions in order to obtain results at parton or particle level. Differential cross-sections were generally measured at particle level in fiducial phase spaces, and often extrapolated to obtain parton-level results in the full phase space as well. Particle-level objects were defined as stable particles (those with lifetimes

¹ ATLAS uses a right-handed coordinate system with its origin at the nominal interaction point (IP) in the centre of the detector and the z -axis along the beam line. Observables labelled as transverse are projected onto the x - y plane. The x -axis points from the IP to the centre of the LHC ring, and the y -axis points upwards. Cylindrical coordinates (r, ϕ) are used in the transverse plane, ϕ being the azimuthal angle around the beam line. The pseudorapidity is defined in terms of the polar angle θ as $\eta = -\ln \tan(\theta/2)$, and the rapidity is defined as $y = (1/2)[(E + p_z)/(E - p_z)]$. The angular distance ΔR is defined as $\Delta R \equiv \sqrt{(\Delta\eta)^2 + (\Delta\phi)^2}$. The transverse momentum is $p_T = p/\cosh(\eta)$.

longer than 30 ps) produced by the MC generators, and fiducial phase spaces were defined with selection requirements close to those used to select events in the data analysis. In contrast, parton-level results, relying on observables based on top-quark four-momenta available in MC simulation samples or fixed-order theoretical calculations, were extrapolated from the selected region to the full phase space without any experimental cuts, again by means of MC simulation. Particle-level results are thus less affected by modelling systematic uncertainties and avoid extrapolations to unmeasured regions of phase space, while parton-level results allow direct comparisons with the most precise predictions. Besides differential cross-sections, some of the inclusive cross-sections were also measured in fiducial phase spaces, in order to avoid extrapolating the result beyond the event topology and kinematic selection used in the analysis.

In terms of statistical analysis, most of the differential cross-section and top-quark property measurements were based on the well-established regularised unfolding technique known as iterative Bayesian unfolding (IBU) [40, 41], while a small number of more recent measurements adopted fully Bayesian unfolding (FBU) [42] or binned profile-likelihood-based unfolding (PLU) [43]. In the last two techniques, systematic uncertainties are encoded in the statistical model as constrained nuisance parameters [44], while in IBU the systematic uncertainties in the unfolded distributions are evaluated by repeating the unfolding procedure for each systematic variation. Moreover, FBU and PLU facilitate the combination of several signal regions to extract a single differential cross-section, as well as the inclusion of control regions to constrain the main background contributions simultaneously with the unfolding.

For most of the inclusive cross-section measurements, as well as for the extraction of parameters controlling the shape of the signal-process distribution (such as the top-quark mass), maximum-likelihood fits were performed. Both binned and unbinned likelihood models were used, with an increasing number of measurements being based on binned profile-likelihood fits. Exclusion limits for BSM processes such as those induced by a FCNC were also based on binned profile likelihoods and computed using the CL_s method [45] with the asymptotic approximation [46].

2.4 Systematic uncertainties and Monte Carlo modelling

With the available dataset being larger than in Run 1, and the consequent reduction of the statistical uncertainty in most of the measurements, systematic uncertainties became more and more important.

In terms of instrumental systematic effects, most of the top-quark measurements and searches are particularly sensitive to uncertainties in jet energy corrections and in the efficiencies of b -tagging algorithms. In Run 2, the jet energy was corrected for pile-up effects and further calibrated, based on both MC simulation and data [20]. Uncertainties in the jet energy scale and resolution were then extracted, based on these correction procedures and on considerations of jet flavour, kinematic and generator dependence. Efficiencies and misidentification rates for the b -tagging algorithms were calibrated in data by analysing $t\bar{t}$ and Z +jet events [17, 18, 47]. The uncertainties in such measurements were then propagated to each analysis and decomposed into sets of uncorrelated sources of uncertainty, including uncertainties assigned to extrapolations to inaccessible kinematic regimes in the calibrations. Depending on the specific analysis, other uncertainties may also be relevant; these include uncertainties in the LHC luminosity, beam energy and pile-up conditions, in lepton selection efficiencies and energy–momentum corrections, and in the determination of the missing transverse momentum.

Apart from these instrumental systematic effects, uncertainties in the details of the MC event-generation process, referred to as ‘modelling’ systematic uncertainties, became more and more important and were

subjected to deeper and deeper studies. In particular, Run 2 ATLAS physics measurements adopted a refined approach, learning from the past data results and benefiting from improvements in MC generators [48].

During Run 2, the modelling of $t\bar{t}$ and single-top processes relied on MC generators that implement the hard process at next-to-leading order (NLO) in QCD and are interfaced with parton-shower generators to implement perturbative and non-perturbative fragmentation processes, as well as with the underlying-event modelling and hadron decays. The nominal predictions were initially obtained with POWHEG BOX v2 [49] interfaced with PYTHIA 6 [50], with the EVTGEN [51] package used to better simulate the decay of heavy-flavour hadrons. After the first set of early Run 2 results, the POWHEG+PYTHIA 6 set-up was replaced by the more recent POWHEG+PYTHIA 8 [52], moving from the Perugia 2012 set of tuned parameters (tune) [53] to the A14 tune [54], derived by the ATLAS Collaboration from a number of its Run 1 measurements at $\sqrt{s} = 7$ TeV. To assess modelling uncertainties in these ‘NLO+PS’ set-ups, a number of alternative predictions were considered, obtained either by varying certain internal parameters in the POWHEG or PYTHIA generators or by replacing one of the two with a different generator.

To account for missing higher orders in the hard-process simulation, QCD scale variations were implemented in POWHEG by scaling the renormalisation and factorisation scales up and down by a factor of two. Initially, such scale variations were included together with variations of the PYTHIA internal parameters controlling the amount of initial-state QCD radiation in the parton shower (specifically ‘Var3c’ in the A14 tune [54], and h_{damp}) to constitute a so-called initial-state radiation (ISR) uncertainty source. This was then refined [48] by splitting the ISR uncertainty source into various components in order to deal with the larger dataset and the consequent risk of artificially overconstraining various fits through insufficient flexibility of the systematic uncertainty model. In addition, uncertainties in the amount of final-state radiation (FSR) were taken into account by varying the effective value of the strong coupling constant, α_s^{FSR} , in the parton shower.

A separate uncertainty was then assigned to the choice of model for the parton-shower evolution and hadronisation processes, quantified by comparing samples from the nominal set-up with those generated after replacing PYTHIA with the HERWIG parton shower. These two parton-shower programs implement different radiation-emission-ordering algorithms as well as different hadronisation models. Similarly to the case of the nominal POWHEG+PYTHIA simulation samples, the definition of this systematic variation was gradually refined during Run 2, by moving from the HERWIG++ parton shower to models based on HERWIG 7 [55], thereby reducing this uncertainty in most measurements.

Finally, an uncertainty related to the choice of matching scheme between the NLO hard-process generator and the parton shower, referred to as an NLO-matching-scheme systematic uncertainty, was considered. It was typically evaluated by comparing the nominal-model samples with samples generated using MADGRAPH5_AMC@NLO [56] in NLO mode (referred to simply as AMC@NLO in the following) instead of POWHEG.² Here also, the exact recipe for the systematic variation evolved during Run 2. The comparison between AMC@NLO+PYTHIA 8 and a modified POWHEG+PYTHIA 8 set-up (suitable for a direct comparison) was replaced by internal systematic variations within the same generator set-up, POWHEG+PYTHIA 8 [58]. For this purpose, the parameter p_T^{hard} , regulating how the PYTHIA 8 radiation phase space is determined, was varied along with the shape of the top-quark mass distribution, accessed by comparing the nominal set-up with a set-up where the top-quark decay is handled by MADSPIN [59].

Some measurements took advantage of the available higher-order predictions for top-quark kinematics, employing next-to-next-to-leading-order (NNLO) fixed-order QCD calculations, possibly combined with

² In some particular cases, the SHERPA [57] event generator was used instead.

NLO electroweak corrections [60], to reweight the $t\bar{t}$ MC sample. This was used either to define an additional uncertainty or to correct the nominal prediction (see Section 3.2).

Uncertainties in parton distribution functions (PDFs) were propagated to the analyses either by considering the envelope of the variations in the NNPDF3.0 PDF set [61], or by implementing the PDF4LHC Run 2 procedure [62], which aims to capture the differences between individual PDF parameterisations as well as the internal variations of individual PDFs. Compared to Run 1, the adoption of these new procedures allowed a factor-of-two reduction of the PDF uncertainty impact in many Run 2 measurements.

Uncertainties in the modelling of multiple partonic interactions (often referred to as the underlying event) and of colour-reconnection effects in top-quark-pair events were also considered for precision measurements. These uncertainties were computed from dedicated variations in the PYTHIA 8 set of tunable parameters [54] and by testing different models for colour reconnection [63–65].

As is noted later in this report, a comprehensive set of such systematic variations, including generator comparisons and parameter value changes that evolved over time to more detailed models, turned out to be just sufficient to cover differences between the prediction and observed data in a wide variety of inspected kinematic quantities.

Within the framework of modelling $t\bar{t}$ and single-top processes with NLO+PS generators, an additional uncertainty concerns the procedure adopted to avoid double counting of diagrams between the generated $t\bar{t}$ and tW samples. These two processes can both lead to $WbWb$ final states and therefore interfere with each other. In $t\bar{t}$ production, the two Wb systems are produced on the top-quark mass shell (also called a doubly resonant process) while the tW process is singly resonant. Two approaches are usually followed to avoid double counting between doubly and singly resonant diagrams [66]: removing NLO diagrams from the tW amplitude if they overlap with $t\bar{t}$ contributions (DR scheme) or adding subtraction terms built to cancel out doubly resonant contributions in the tW amplitude (DS scheme). The nominal tW model adopted the DR scheme, while alternative tW samples generated with the DS scheme were used as systematic variations. As described in Section 4.2, dedicated measurements were performed by ATLAS to assess the merits of the two alternative models, with the goal of reducing this significant source of systematic uncertainty.

The modelling of processes other than $t\bar{t}$ and single top production followed these recipes as closely as possible, although different generator set-ups were used for some processes, and not all systematic variations were always technically implementable [67, 68].

Further improvements in MC modelling are expected in the future, including possible refined parton-shower parameter tunings based on ATLAS $t\bar{t}$ data, the implementation of generators modelling full $t\bar{t}$ production and decay at NLO (the so-called ‘bb4l’ set-up [69]) and the employment of NNLO matrix-element generators matched to parton showers, as is done in the MINNLO_{PS} implementation [70], already compared with the full Run 2 ATLAS data in the differential $t\bar{t}$ cross-section measurement currently being finalised [71].

3 Top-quark pair production

The unprecedented centre-of-mass energy and large pp collision dataset collected in Run 2 gave ATLAS the opportunity to exploit the full potential of the LHC as a ‘top-quark factory’. The $t\bar{t}$ production cross-section in $\sqrt{s} = 13$ TeV pp collisions is ~ 3.5 times larger than at the highest centre-of-mass energy, 8 TeV, in Run 1, and the Run 2 data sample contains over a hundred million $t\bar{t}$ pairs. With such a large data sample, increasingly precise inclusive and differential $t\bar{t}$ cross-section measurements became possible, providing

valuable input for PDF fits, allowing precision tests of QCD predictions, and probing phase-space regions sensitive to new physics processes.

3.1 Inclusive top-quark pair cross-section measurements

Increasingly precise predictions for the total $t\bar{t}$ cross-section have been produced in the past years, reaching NNLO accuracy in the strong coupling constant α_s [72], and including EW corrections at NLO [73–75] as well as resummation of next-to-next-to-leading logarithmic (NNLL) soft gluon terms [76] and even adding soft gluon corrections up to third order, resulting in approximate-N³LO results [77]. At $\sqrt{s} = 13$ TeV, with the top-quark mass value fixed to 172.5 GeV and using the PDF4LHC21 PDFs [78], the cross-section obtained from the TOP++ 2.0 program [79], at NNLO in QCD and including NNLL resummation, is:

$$832^{+20}_{-29} \text{ (scale)}^{+35}_{-35} \text{ (PDF}+\alpha_s) \text{ pb,}$$

where uncertainties from factorisation and renormalisation scale variations and the impact of uncertainties in the PDFs (calculated using the PDF4LHC prescription [62]) and α_s are quoted separately. An additional uncertainty of ± 23 pb arises from the uncertainty in the top-quark mass.³

The most precise measurements of the inclusive $t\bar{t}$ cross-section were performed by using the cleanest final state, with an opposite-sign electron–muon pair plus at least one b -tagged jet. The measurement using the 2015 dataset [80] adopted the analysis technique inherited from the corresponding Run 1 measurements [81], based on the so-called b -tag counting method. In order to minimise the impact of systematic uncertainties related to hadronic-jet selection (including b -tagging), the $t\bar{t}$ cross-section was extracted simultaneously with an effective value for the b -jet selection efficiency by taking as input the numbers of events with exactly one and exactly two b -tagged jets. The cross-section was determined by solving a system of two equations with two unknowns. The event selection requirements were kept as loose as possible, in order to minimise the impact of many systematic uncertainties. Finally, by restricting the event topology to opposite-sign $e\mu$ pairs, the contribution from background processes was minimised, with Z +jet, W +jet, t - and s -channel single-top, and diboson production contributing very little, and single-top tW events being almost the only ones contributing significantly. This first measurement, already achieving a precision of 4.4%, was updated with the larger 36 fb^{-1} dataset [82], lowering the uncertainty to 2.4%, and again with the full Run 2 dataset [83], reaching an outstanding precision of 1.8%. The last improvement comes almost entirely from the decrease in the luminosity uncertainty [27], resulting from improvements in the ATLAS pp luminosity calibration transfer and long-term stability analyses, as well as changes to the van der Meer calibration procedures. The measured values, and the corresponding statistical and systematic uncertainties, are reported in Figure 3, together with the other ATLAS Run 2 inclusive $t\bar{t}$ cross-section measurements performed in other channels. Good agreement with the theory prediction can be seen. The statistical uncertainty was already subdominant with the 2015 dataset, despite the small acceptance for the $e\mu$ channel. Among the systematic uncertainties, the most important contributions were those from uncertainties in the luminosity determination, LHC beam energy, and $t\bar{t}$ process modelling. In addition to the reduction in the luminosity uncertainty, the beam energy uncertainty was also reduced significantly since the first Run 2 measurement, already reaching a precision of 0.1% for the measurement based on the 2015+2016 dataset [84]. Among the $t\bar{t}$ process modelling systematic uncertainties, those associated with the choice of parton-shower and hadronisation model constitute one of the most important sources of uncertainty for all the measurements, even with the most up-to-date tuned PYTHIA 8 and HERWIG 7 generators.

³ The uncertainty corresponds to a ∓ 1 GeV shift in the m_t value set in the computation.

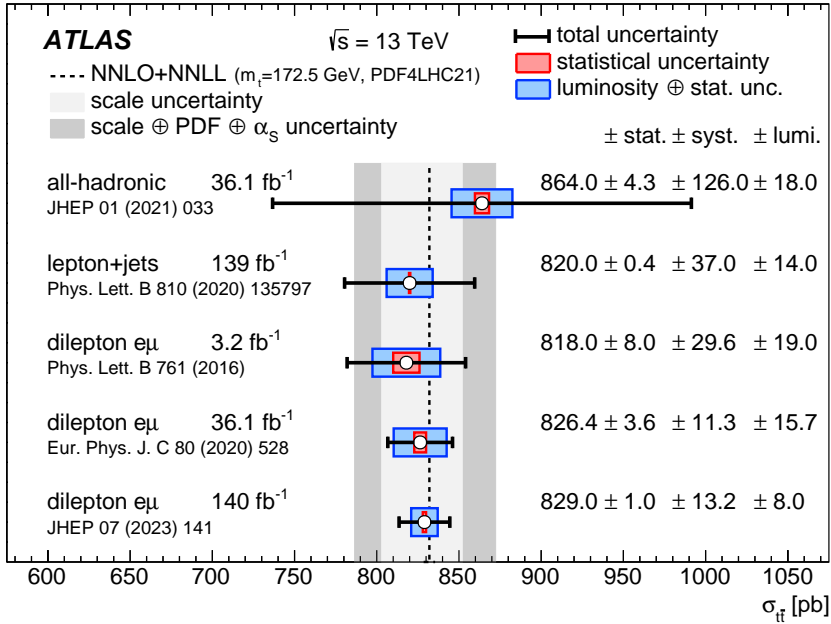


Figure 3: Summary of ATLAS inclusive $t\bar{t}$ cross-section measurements at $\sqrt{s} = 13$ TeV based on Run 2 data, compared with the exact NNLO QCD calculation complemented with NNLL resummation (Top++ 2.0). The theory band represents uncertainties due to renormalisation and factorisation scales, parton distribution functions and the strong coupling constant. The uncertainties in the experimental measurements are broken down into their statistical and systematic components, quoting the uncertainty related to the integrated luminosity separately. The measurements and the theory calculation are quoted for $m_t = 172.5$ GeV.

These inclusive $t\bar{t}$ cross-section measurements were used as one of the inputs for high-precision determinations of ratios of $t\bar{t}$ and Z production cross-sections at the three centre-of-mass energies where ATLAS measurements are available: $\sqrt{s} = 13, 8, 7$ TeV. This was already done with the first measurement based on 3.2 fb^{-1} of Run 2 data [85]: single ratios, at a given \sqrt{s} for the two processes and at different \sqrt{s} values for each process, as well as double ratios of the two processes at different \sqrt{s} values, were evaluated and then compared with NNLO calculations using recent PDF sets, demonstrating significant power to constrain both the gluon distribution function for Bjorken- x values near 0.1 and the light-quark sea for $x < 0.02$. The second $t\bar{t}$ cross-section paper, based on 36 fb^{-1} of Run 2 data [82], included updated computations of these ratios and double ratios of $t\bar{t}$ and Z cross-sections at different energies. This inclusive $t\bar{t}$ cross-section measurement was also used to extract the top-quark mass with an uncertainty of approximately 2 GeV, as detailed in Section 6.

The inclusive $t\bar{t}$ cross-section was also measured in other final states, despite not reaching the same precision. In particular, the total cross-section was measured in the lepton-plus-jet channel [86], by a simultaneous profile-likelihood fit of three different binned observables in three different event categories, characterised by different numbers of jets and b -tagged jets. An additional uncertainty, estimated as the difference between the results obtained with the nominal MC generator and a sample reweighted to the NNLO (QCD) + NLO (EW) parton-level prediction [60], was applied (as discussed in Section 3.2). Moreover, an inclusive $t\bar{t}$ cross-section was measured in all-hadronic final states [87], but with significantly larger uncertainties. These results are reported and compared with those obtained in the dilepton channel in Figure 3. As can be seen, all the measurements are in good agreement with each other and with the

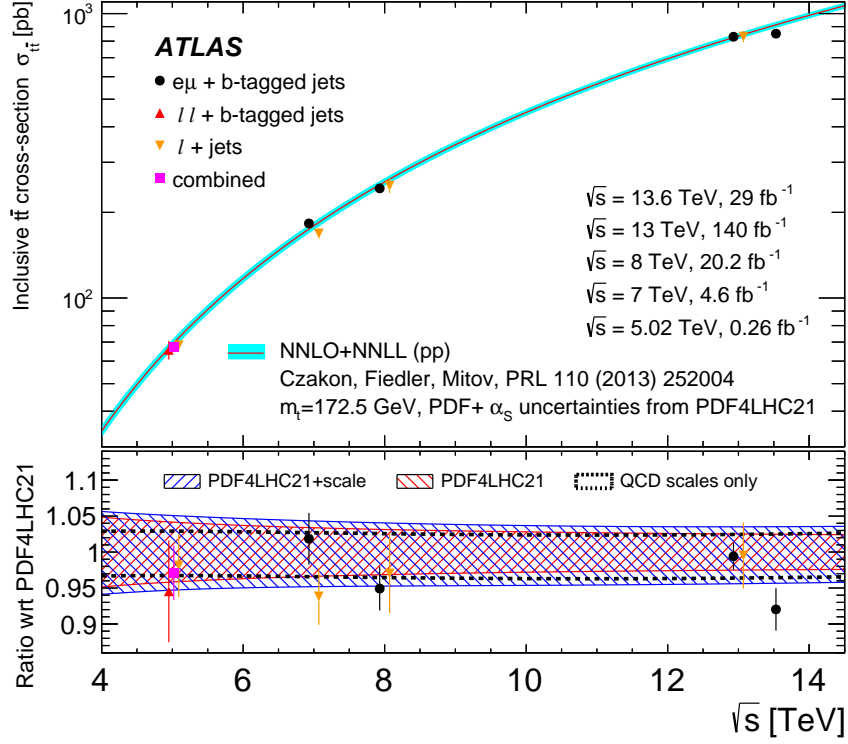


Figure 4: Summary of ATLAS measurements of the top-quark pair production cross-section as a function of the centre-of-mass energy and comparison with the NNLO QCD calculation complemented with NNLL resummation (Top++ 2.0). The theory band represents uncertainties due to renormalisation and factorisation scales, parton distribution functions and the strong coupling constant. The measurements and the theory calculation are quoted for $m_t = 172.5$ GeV. Measurements made at the same centre-of-mass energy are offset slightly for clarity. The figure was originally published in Ref. [90].

theoretical predictions, with the precision of the experimental determination exceeding that of the QCD NNLO+NNLL computation.

Inclusive $t\bar{t}$ cross-section measurements were performed by ATLAS with similar techniques at the different LHC pp centre-of-mass energies. In Run 1, measurements were performed in both the $e\mu$ dilepton channel [81] and the lepton-plus-jet channel [88, 89] at $\sqrt{s} = 7$ and 8 TeV. The inclusive $t\bar{t}$ cross-section was also measured by ATLAS at $\sqrt{s} = 5.02$ TeV, analysing the ~ 260 pb $^{-1}$ of pp data collected during Run 2 at this reduced centre-of-mass energy in low-pile-up conditions. This measurement was obtained by combining the lepton-plus-jet and dilepton channels [89]. Finally, at the new energy of $\sqrt{s} = 13.6$ TeV achieved in Run 3, a measurement was made in the $e\mu$ dilepton channel using the first 29 fb $^{-1}$ of collected data [90]. In Figure 4, all these measurements, together with the most precise ones performed at $\sqrt{s} = 13$ TeV, are shown and compared with QCD NNLO+NNLL predictions as a function of the centre-of-mass energy. Agreement between the various measurements and the theoretical predictions is remarkable over the whole range of centre-of-mass energies.

3.2 Differential top-quark pair cross-section measurements

Besides the inclusive measurements, ATLAS used the Run 2 data to measure a large variety of differential $t\bar{t}$ cross-sections in different final states and kinematic regimes. Shortly after the first inclusive cross-section measurement at $\sqrt{s} = 13$ TeV, differential distributions were measured, with the same 3.2 fb^{-1} dataset, in both the dilepton channel [91, 92] and the lepton-plus-jet channel [93, 94]. With the larger 36 fb^{-1} dataset, a new set of measurements were performed, increasing the number of measured observables and improving the precision in the dilepton [82] and lepton-plus-jet [95] topologies, as well as including all-hadronic final states [87, 96]. Finally, the total Run 2 dataset was used to refine and update the differential cross-section measurements in all three channels [83, 97, 98].

Measurements in the different channels can benefit from different opportunities offered by specific topologies. The $t\bar{t}$ dilepton channel was used to achieve high-precision measurements as well as to study properties of $t\bar{t}$ production in an environment characterised by lower hadronic activity than in the other channels. In Ref. [91], quantities sensitive to jet activity in the $t\bar{t}$ process were measured in events with an $e\mu$ opposite-sign lepton pair and two b -tagged jets. These include the multiplicity of additional jets, their p_T distributions, as well as the so-called ‘gap fraction’, i.e. the fraction of signal events not containing additional jets in a given rapidity region. All these quantities are highly sensitive to details of the parton-shower models and it is therefore important to measure them in order to validate the MC generator predictions. The gap fraction was measured as a function of the p_T threshold for additional jets and for different invariant-mass regions of the $e\mu b\bar{b}$ system. In Ref. [92], using the same sample of $t\bar{t}$ events, differential cross-sections were measured as a function of the transverse momentum and absolute rapidity of the top quark, and of the transverse momentum, absolute rapidity and invariant mass of the $t\bar{t}$ system. These measurements, unfolded to parton level, provide valuable input for testing higher-order QCD predictions. In order to perform the measurements, the top-quark pair four-momenta were reconstructed using the Neutrino Weighting technique [99], which uses top-quark and W -boson mass constraints to infer the two neutrinos’ kinematics from only a measurement of the sum of their transverse momenta, given by the event’s missing transverse momentum E_T^{miss} . The most recent measurements in the dilepton $e\mu$ channel [82, 83], published together with the corresponding inclusive cross-section determinations, followed an alternative and complementary strategy. No attempt was made to reconstruct the top quarks from their partially invisible decay products, and instead only leptonic kinematic variables were unfolded, at particle level in a fiducial phase space, both individually and as double-differential distributions, resulting in very clean and precise measurements. Such an approach was pursued previously in Run 1 data [100], allowing an indirect determination of the top-quark mass. The technique used for the inclusive measurement was applied to extract the cross-section in each of the bins.

The lepton-plus-jet and all-hadronic channels offered the advantage of easier reconstruction of the top-quark four-momenta, thanks to the presence of at most one neutrino among the $t\bar{t}$ decay products. In addition, they offered the opportunity to probe extreme kinematic regimes by providing a larger number of events and the possibility of adopting ‘boosted top-tagging’ techniques to reconstruct highly collimated, hadronically decaying top quarks. In particular, the all-hadronic channel, despite being affected by larger backgrounds, allows full reconstruction of the kinematics of both top quarks in the event without relying on a measurement of the missing transverse momentum. Moreover, it ensures a higher selection efficiency for high-energy events, where both top quarks have a large boost and their decay products are collimated.⁴ Differential

⁴ Dilepton and lepton-plus-jet channel measurements typically need to identify at least one isolated electron or muon, while leptons in boosted topologies tend to be produced at small angular separations from the b -jet coming from the same parent top quark, resulting in non-isolated charged-lepton signatures, which are hard to identify correctly in hadronic environments.

cross-sections were measured in the lepton-plus-jet channel in both the ‘resolved’ [93–95] and ‘boosted’ topologies [93, 97], as well as in the all-hadronic channel for resolved [87] and boosted regimes [96, 98]. A large number of distributions were unfolded at particle level to fiducial phase spaces, and at parton level to the total phase space. These distributions included top-quark transverse momentum and rapidity (y); $t\bar{t}$ system invariant mass, p_T and y ; and other observables related to top-quark kinematics, initial- and final-state radiation emission and the PDFs. Double-differential distributions were also extracted, in both the resolved and boosted topologies. Top-quark four-momenta were obtained in boosted topologies by reconstructing large- R jets, with possible identification using top-tagging techniques. For the resolved topology, top-quark kinematics were retrieved in different ways in the different measurements. In the lepton-plus-jet channel, the so-called pseudo-top algorithm [101] was used; it relies on invariant-mass constraints from the known mass of each of the two W bosons and on angular distances between jets and leptons, allowing the hadronically and leptonically decaying top quarks to be reconstructed with very similar efficiency at both detector level and particle level. Alternatively, measurements performed at parton level used the so-called KLFitter [102] package, which provides a constrained fitting algorithm that uses transfer functions to relate the energies of the reconstructed objects to those of the parton-level objects. In the all-hadronic channel, a χ^2 minimisation, relying on top-quark and W -boson mass constraints, was used to reconstruct top quarks in the resolved topology. In both the lepton-plus-jet and dilepton channels, cross-sections were measured with a precision of about 10%–20% for top-quark p_T up to ~ 1.5 TeV and $m_{t\bar{t}}$ up to ~ 3 TeV.

All these measurements were compared with a large set of predictions. Particle-level results were used to test MC predictions from various generator set-ups, while parton-level ones could also be compared with fixed-order calculations. The early measurements turned out to be very useful for testing and validating MC generator set-ups for $t\bar{t}$ production. In particular, it became possible to rule out certain set-ups because they gave a poor description of the data: for instance, the prediction from POWHEG BOX interfaced with HERWIG++ gave a poor description of most of the inspected distributions, especially the additional-jet multiplicity, and was later replaced with a prediction making use of the more recent HERWIG 7 program. Measurements based on larger datasets started to systematically reveal limitations in the modelling of certain kinematic distributions by most of the MC generators. The modelling of the top-quark transverse momentum as well as that of the $t\bar{t}$ system was found to be particularly poor, with most of the NLO+PS predictions, including those from the most recent refined MC generator set-ups, overestimating the cross-section at high momenta, especially in boosted topologies (see Figure 5 (a)). Agreement was improved when comparing parton-level measurements with NNLO QCD fixed-order predictions or by reweighting the MC samples to match these predictions for the top-quark kinematics, as can be seen in Figure 5 (b).

3.3 Studies of b -jet production in top-quark-pair events

In addition to inclusive and differential $t\bar{t}$ cross-section extractions, measurements of the $t\bar{t}$ production process with extra b -jets were performed with Run 2 data. Cross-sections for $t\bar{t} + b\bar{b}$ production were measured [103] with the 36 fb^{-1} dataset. Inclusive and differential cross-sections were measured in the single-lepton and dilepton channels, specifically for $t\bar{t}$ events with additional b -quark jets defined at particle level in dedicated fiducial phase spaces. These measurements were compared with predictions from various MC generator set-ups, and validated the background models for measurements of $t\bar{t}H$ production in the $H \rightarrow b\bar{b}$ decay channel as well as for new-physics searches in similar final states. Figure 6 (a) shows the results of the measurement, in terms of inclusive fiducial cross-sections for the two channels, separately for fiducial phase spaces with ≥ 3 b -jets or ≥ 4 b -jets. These measured inclusive cross-sections are higher than

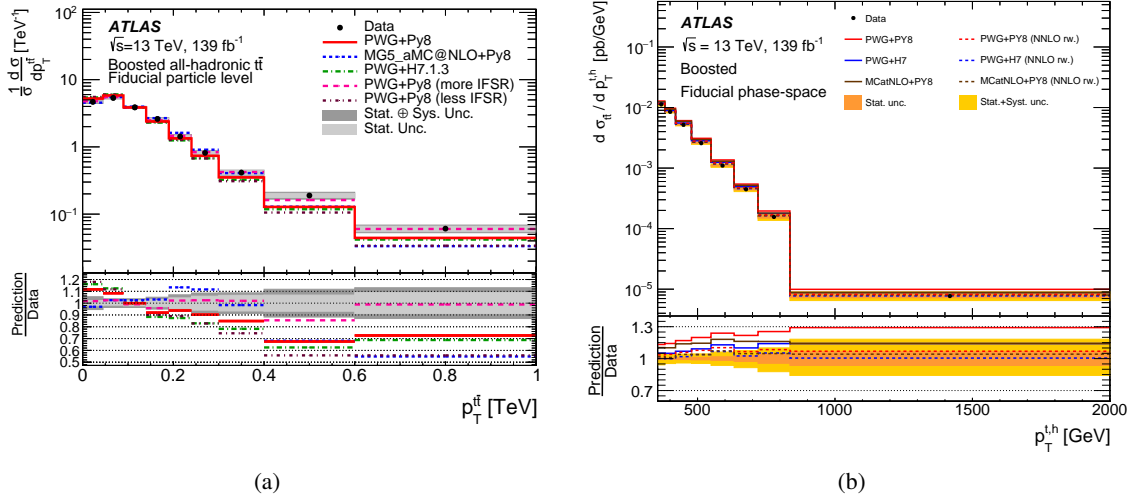


Figure 5: Two examples of ATLAS differential $t\bar{t}$ cross-section measurements. (a) Normalised particle-level $t\bar{t}$ -system transverse momentum distribution extracted in all-hadronic boosted final states, compared with a number of NLO+PS MC predictions [98]. (b) Particle-level transverse momentum distribution of hadronically decaying top quarks measured in the lepton-plus-jet boosted channel, compared with MC predictions, including predictions where a reweighting of top-quark kinematics is performed to match higher-order fixed-order calculations (see text for more details) [97].

the predictions from the dedicated $t\bar{t} + b\bar{b}$ NLO generators matched to parton-shower programs, but still within the uncertainties. The differential distribution comparisons do not show significant mismodelling by most of these generators, beyond the experimental uncertainties of the unfolded results.

Finally, the same dataset was used to study b -jets in $t\bar{t}$ events [104]. A number of observables sensitive to quark fragmentation were measured in jets identified as originating from top-quark decays, thus providing an almost completely pure b -quark jet sample. Top-quark-pair events were selected in the dilepton $e\mu$ channel, and the set of charged-particle tracks associated with jets were separated into those from the primary pp interaction vertex and those from the displaced b -hadron decay secondary vertex, in order to construct observables characterising the longitudinal and transverse momentum distributions of b -hadrons within b -quark jets. These measurements complement the measurements performed at e^+e^- colliders, in which the b -quarks originate from a colour-singlet (Z/γ^*), allowing the universality of the fragmentation models to be tested. Figure 6 (b) shows one of the measured distributions, compared with various MC predictions. Despite being in overall agreement with the models tuned at e^+e^- colliders, the measured distributions are still affected by large experimental uncertainties or limited by the amount of data in several bins, preventing the current results from constraining the MC models.

4 Single-top-quark production

In the SM, the dominant single-top-quark production process at hadron colliders occurs through the tWb vertex according to three distinct diagrams at LO in QCD (see Figure 2): the exchange of a virtual W boson in the t -channel, a W -boson exchange in the s -channel, and the associated production of a top quark and a W boson (named tW). In pp collisions at LHC energies, the t -channel process is dominant. The cross-section

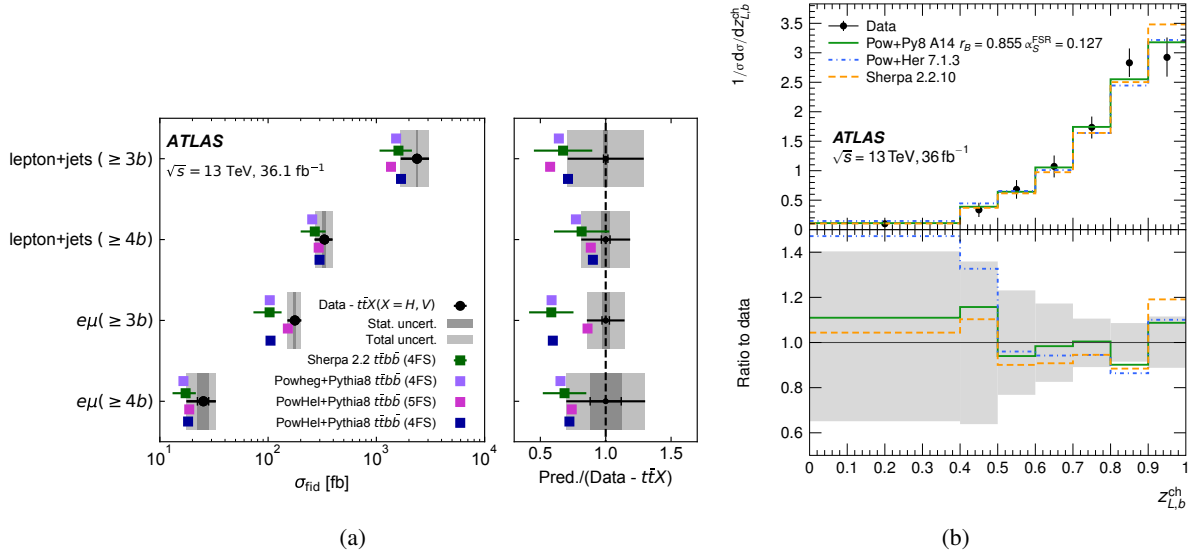


Figure 6: (a) Measured fiducial $t\bar{t} + b$ -jet cross-sections [103], with $t\bar{t}H$ and $t\bar{t}$ -plus-vector-boson contributions subtracted from the data, compared with predictions from different generator set-ups. (b) Particle-level differential cross-section as a function of $z_{L,b}^{\text{ch}}$ [104], compared with predictions from different generator set-ups. The quantity $z_{L,b}^{\text{ch}}$ is defined as the fraction of the total charged-particle momentum in a jet carried by the b -hadron decay products along the direction of the jet.

for each of the three single-top-quark production channels is sensitive to the coupling between the W boson and the top quark at the Wtb vertex. Single top-quark production therefore presents an opportunity to test the structure of this coupling in the SM, as well as to probe classes of new-physics models that can affect the Wtb vertex. The different single-top production modes are sensitive to different BSM models, so it is important to study them separately [105, 106].

4.1 Measurements in the t -channel

In the t -channel, a light-flavour valence quark from one of the colliding protons interacts with a b -quark which can originate from the proton sea (in the so-called five-flavour scheme, where all the quark flavours except the top are included in the proton PDFs) or from gluon splitting (in the five-flavour scheme and also in the four-flavour scheme, where only the four lightest quarks are included in the proton PDFs). After the exchange of a space-like virtual W boson, the produced top quark or antiquark recoils against a light-flavour quark, referred to as the spectator quark. This quark is preferentially emitted in the forward direction. Since the density of valence u -quarks in the proton is about twice as large as that of valence d -quarks, the single-top-quark production cross-section, $\sigma(tq)$, is about twice as large as the single-top-antiquark production cross-section, $\sigma(\bar{t}q)$. For pp collisions at $\sqrt{s} = 13$ TeV, the predicted t -channel production cross-sections (for $m_t = 172.5$ GeV) are $\sigma(tq) = 134.2 \pm 2.2$ pb and $\sigma(\bar{t}q) = 80.0 \pm 1.6$ pb, computed at NNLO in perturbative QCD with the MCFM program [107]. This corresponds to an increase by around a factor of 2.5 compared to the SM t -channel cross-sections at $\sqrt{s} = 8$ TeV. Measurements of t -channel production were made first with 3.2 fb^{-1} of Run 2 data [108] and later with the full dataset [109]. Separate measurements of top-quark or top-antiquark production were conducted because they provide sensitivity

to different PDFs (the u -quark and d -quark PDFs). Measurements of their ratio, $R_t = \sigma(tq)/\sigma(\bar{t}q)$, also profit from systematic uncertainties partially cancelling out, allowing even higher sensitivity to the PDFs. Events were required to have a single isolated electron or muon from the leptonic decay of the top quark or antiquark, and exactly two jets, among which exactly one is b -tagged. The t -channel signal was separated from the background by using a neural network (NN). A binned maximum-likelihood fit to the NN discriminant distribution in the channel with positively or negatively charged leptons was performed to extract the top-quark or top-antiquark inclusive cross-section, respectively. The fits yield $\sigma(tq) = 137 \pm 8$ pb, $\sigma(\bar{t}q) = 84_{-5}^{+6}$ pb and $R_t = 1.636_{-0.034}^{+0.036}$, in agreement with SM predictions.

Because of the vector minus axial-vector ($V - A$) structure of the Wtb vertex, the single top quarks are highly polarised along the direction of the momentum of the spectator quark (or opposite to it in the case of single top antiquark production). ATLAS used the full Run 2 dataset and t -channel single top production to probe the polarisation of the top quark and top antiquark [110]. The event selection was similar to that used to measure the t -channel production cross-section. Among the two required jets, the non- b -tagged jet was assumed to originate from the spectator quark. The charged lepton from the top-quark decay is the most sensitive probe of the top-quark spin, so the angular distributions of the charged leptons were used to extract the components of the polarisation vectors. The polarisation vector was expressed in three orthogonal directions, where the z' direction was chosen to be the momentum direction of the spectator quark [111]. The W boson from the top-quark decay was reconstructed from the lepton kinematics and the reconstructed missing transverse momentum, imposing a W -boson mass constraint. The top-quark candidate was then reconstructed by combining the four-momentum of the W boson with that of the b -tagged jet. Finally, the charged lepton's momentum was boosted into the top-quark rest frame to define its polar angles in the polarisation coordinate system. The differential distributions of these polar angles could then be used to extract the three polarisation components $P_{x'}$, $P_{y'}$ and $P_{z'}$ of the top-quark and top-antiquark polarisation vectors, using a template fit to these distributions in the top-quark rest frame. The results demonstrate a very high degree of polarisation in t -channel production, along the direction of the spectator quark (for top-quark events), or opposite to that direction (for top-antiquark events), in agreement with NNLO QCD predictions. The polar-angle differential distributions were also unfolded to particle level in a fiducial region. The normalised unfolded distributions show good agreement with the SM prediction, with a p -value close to 1 (see Figure 7 (a)), and were used to derive competitive bounds on anomalous tW couplings (see Section 9).

4.2 Measurements in the tW channel

At the LHC, the second largest single-top-quark production cross-section is the one for single top production in association with a W boson, i.e. tW , which accounts for approximately 24% of the total single-top-quark production rate at $\sqrt{s} = 13$ TeV. This process was beyond the reach of the Tevatron, and was first observed in $\sqrt{s} = 8$ TeV data at the LHC [113, 114], with cross-section measurements in good agreement with theoretical predictions. The expected $\sqrt{s} = 13$ TeV SM tW cross-section at NLO including next-to-next-to-leading logarithms is $\sigma(tW) = 79.3_{-1.8}^{+1.9}$ (scale) ± 2.2 (PDF+ α_s) pb [115]. ATLAS measured this process using 3.2 fb^{-1} of data collected in 2015 [116] in the final state with exactly two oppositely charged leptons and at least one b -tagged jet, using the same boosted decision tree (BDT) technique as in the $\sqrt{s} = 8$ TeV measurement. Accurately estimating the kinematic distributions of the tW process is difficult since this process is not well-defined at higher order in QCD because of interference with $t\bar{t}$ production (see Section 2.4). The difference between results obtained with the DR and DS treatments is then taken as an uncertainty and is sizeable in many analyses. The $\sqrt{s} = 13$ TeV dataset made it possible to perform

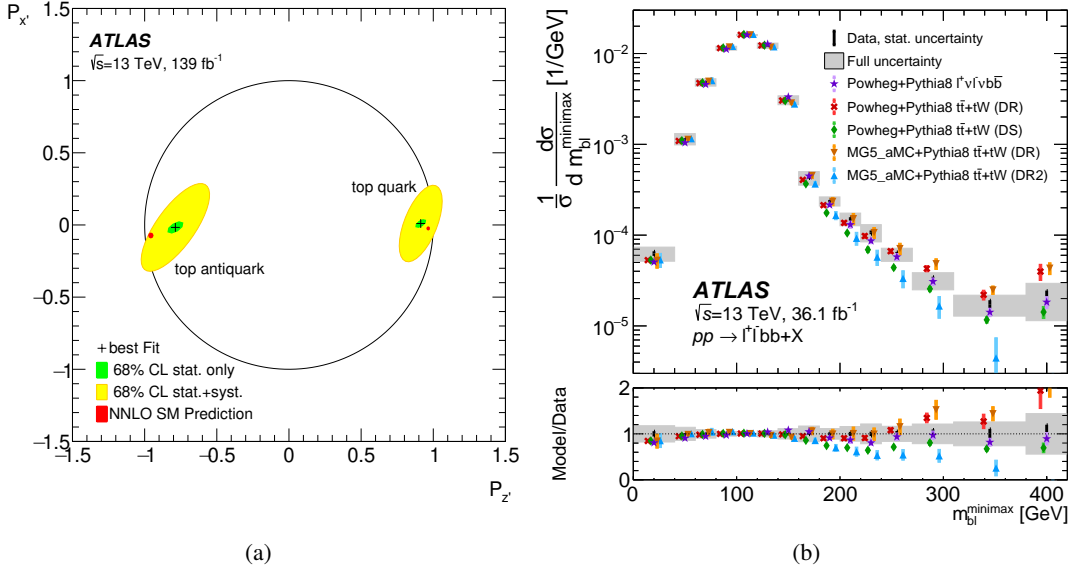


Figure 7: (a) Observed best-fit polarisation measurements with their statistical (green) and statistical+systematic (yellow) uncertainty contours at 68% CL, plotted on the two-dimensional polarisation parameter space (P_z', P_x') [110]. (b) Unfolded normalized differential $m_{b\ell}^{minimax}$ cross-section compared with various theoretical models [112].

measurements that test this modelling, and ATLAS exploited this in two ways: measuring the differential tW cross-section distributions [117] and using specific variables sensitive to the interference [112].

The differential cross-section was measured [117] in the dilepton final state, using 36 fb $^{-1}$ of data and requiring the presence of exactly one b -tagged jet and no additional jets. A BDT was constructed to separate the tW signal from the large $t\bar{t}$ background. The regions with only untagged jets or more b -tagged jets were used as validation regions. In this channel, the top quark or the W boson cannot be reconstructed directly because of the undetected neutrinos. However, some observables are correlated with the kinematic properties of the tW process and its modelling. The unfolding to particle level was performed within a fiducial phase space and the obtained distributions were normalised. The largest uncertainties come from the limited size of the data sample as well as $t\bar{t}$ and tW MC modelling. In general, most of the MC models show fair agreement with the measured cross-section distributions, although the predicted distributions are softer than the observed ones. Both the statistical and systematic uncertainties have a significant impact on the result, with total uncertainties ranging from 10% to 50% depending on the bins. The differential tW cross-section measurement is therefore expected to improve significantly as more data is used.

Interference between tW and $t\bar{t}$ production was specifically probed in the dilepton final state using 36 fb $^{-1}$ of data in a phase space with exactly two b -tagged jets (and no additional jets passing a looser b -tagging requirement) [112]. The contributions from doubly and singly resonant amplitudes depend on the invariant mass of the bW pairs in the event. Since the charged-lepton kinematics are correlated with those of the W boson, the invariant mass of the b -jet and the charged lepton is an interesting observable for testing the interference. As there are some ambiguities in forming this mass, the differential cross-section was measured as a function of $m_{b\ell}^{minimax} = \min\{\max(m_{b_1\ell_1}, m_{b_2\ell_2}), \max(m_{b_1\ell_2}, m_{b_2\ell_1})\}$, an observable inspired by Refs. [118, 119], with b_i and ℓ_i being the two b -tagged jets and leptons respectively. The doubly resonant contribution is suppressed above $\sqrt{m_t^2 - m_W^2}$ (where m_t and m_W are the top-quark and W -boson masses), so the differential cross-section above this kinematic endpoint has more sensitivity to interference

effects. The $m_{b\ell}^{\text{minimax}}$ distribution was unfolded to particle level using an iterative Bayesian unfolding and the normalised unfolded distribution was compared with the predictions (see Figure 7 (b)). The modelling systematic uncertainties, which impact the results the most, range from 1% to 22% of the unfolded yields, while the statistical uncertainty is as large as 20%. The predictions using the DR scheme give a better description of the normalisation of the region $m_{b\ell}^{\text{minimax}} \geq m_t$ but the DS scheme models the $m_{b\ell}^{\text{minimax}}$ shape better in the same region. In general, the DR and DS predictions bracket the data in the region of large $m_{b\ell}^{\text{minimax}}$, justifying the application of their difference as a systematic uncertainty. Later studies showed that this difference could be narrowed by using dynamic scales. The full $\ell^+\nu\ell^-\bar{\nu}b\bar{b}$ predictions implemented in POWHEG BOX RES [120, 121], which includes off-shell top-quark effects at NLO and the interference term, gives the best predictions of $m_{b\ell}^{\text{minimax}}$ over the full distribution. It is expected to eventually replace the model where the $t\bar{t}$ and tW production processes are generated separately.

4.3 Measurement in the s -channel

Among the three single-top-quark production channels mediated by tW vertices, the weakest one at the LHC is the s -channel, in which a top quark is produced with a bottom antiquark via an s -channel W -boson exchange. This process contributed a larger fraction of the single-top events at the Tevatron, where it was observed in proton–antiproton collisions by the CDF and D0 collaborations [122]. At the LHC, ATLAS found evidence for this process in pp collisions at $\sqrt{s} = 8$ TeV with an observed (expected) significance of 3.2 (3.9) standard deviations relative to the background-only hypothesis [123]. Between $\sqrt{s} = 8$ TeV and 13 TeV, the ratio of the s -channel single-top cross-section to the dominant $t\bar{t}$ background’s cross-section decreases from 2.1% to 1.2%, making the analysis more challenging at $\sqrt{s} = 13$ TeV. In the SM, the s -channel single-top production cross-section in pp collisions at $\sqrt{s} = 13$ TeV is $\sigma_{s\text{-channel}} = 10.32^{+0.40}_{-0.36}$ pb, calculated at NLO in QCD with HATHOR 2.1 [124].

Despite these challenges, ATLAS measured this cross-section at $\sqrt{s} = 13$ TeV in the final state with one lepton and exactly two b -tagged jets [125]. To extract the signal from the large background composed of $t\bar{t}$, W +jets and t -channel single-top events, a discriminant based on the matrix-element method [126, 127] was used. This discriminant was built from the likelihood values computed for the hypothesis that a measured event came from a given process. The likelihood values were computed by integrating the matrix elements for the signal or background processes. The s -channel single-top production cross-section was measured from a binned profile-likelihood fit of this discriminant, which also allowed the normalisation of both the $t\bar{t}$ and W +jets background processes to vary freely. The analysis yields $\sigma_{s\text{-channel}} = 8.2 \pm 0.6$ (stat.) $^{+3.4}_{-2.8}$ (syst.) pb in agreement with the SM prediction. The largest systematic uncertainty comes from the $t\bar{t}$ normalisation, followed by those from the jet energy scale and signal modelling. This corresponds to an observed (expected) significance of 3.3 (3.9) standard deviations for s -channel production relative to the background-only hypothesis. The significance is similar to that in the $\sqrt{s} = 8$ TeV analysis, despite the larger data sample, because of the lower signal-to-background ratio at $\sqrt{s} = 13$ TeV.

The $\sqrt{s} = 13$ TeV inclusive single-top cross-section measurements are summarised in Figure 8. The t -channel cross-section measurement was used to determine that the coupling at the Wtb vertex is $f_{LV} \cdot |V_{tb}| = 1.015 \pm 0.031$ [109], where V_{tb} is the corresponding element of the Cabibbo–Kobayashi–Maskawa matrix [128, 129], and f_{LV} is a possible additional left-handed form factor [130] (in the SM, $f_{LV} = 1$). Bounds were also placed on possible anomalous couplings within the framework of effective field theory (see Section 9).

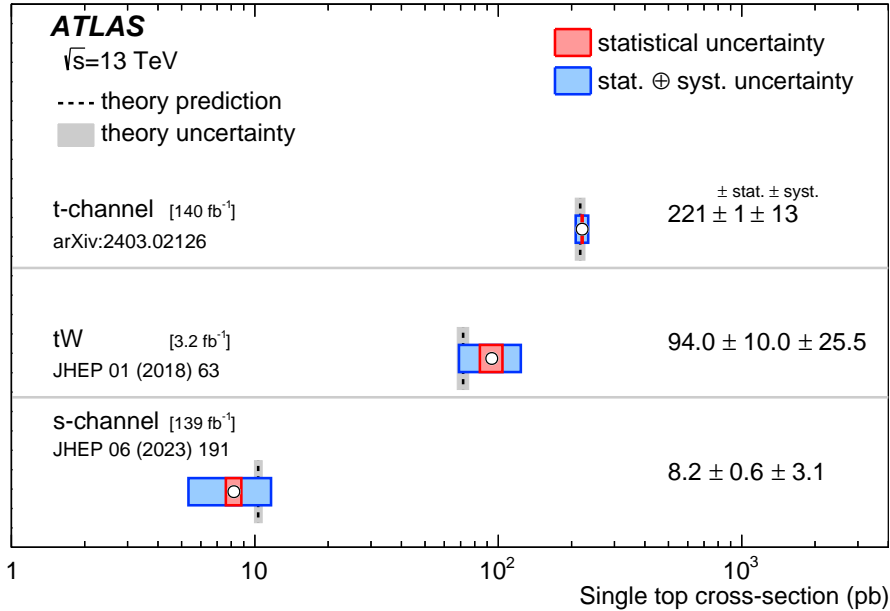


Figure 8: Summary of the $\sqrt{s} = 13$ TeV single-top-quark cross-section measurements, compared with the corresponding theoretical expectations. The values are quoted for $m_t = 172.5$ GeV. The theory predictions are taken from Refs. [107] (t -channel), [131] (tW) and [124] (s -channel).

5 Associated production of top quarks

The high centre-of-mass energy and large Run 2 data sample have brought the study of rare top-quark production processes to a new level. Such processes include the production of a top quark or $t\bar{t}$ pair in association with a Z , W or γ (the process where a $t\bar{t}$ pair is produced with a Higgs boson, $t\bar{t}H$, is described in Ref. [132]). The cross-section of each of these rare associated-production processes (‘top+ V ’ processes, where V is a vector boson) is significantly larger in Run 2 than at $\sqrt{s} = 8$ TeV, where they were first explored. These cross-sections can be related to the coupling of the top quark to the associated boson, allowing the measurement of the top quark’s neutral-current coupling or the top quark’s Yukawa coupling. The top+ V production cross-sections could be altered by physics beyond the SM, such as a vector-like quark [133, 134], a strongly coupled Higgs boson [135], or a heavy scalar or pseudoscalar boson [136–138]. Even if such new physics is beyond the energy reach of the LHC for direct observation, it can manifest itself by changing the top+ V cross-sections through virtual contributions involving new particles. Their effect can be parameterised in the context of an effective field theory (EFT) framework as dimension-six operators that extend the SM Lagrangian [139, 140] (see Section 9). At $\sqrt{s} = 13$ TeV, the simultaneous production of four top quarks has a cross-section large enough to make its observation feasible.

As in the case of $t\bar{t}$ production, the experimental challenges differ depending on the decays of the W bosons coming from the top quarks. The ‘golden channel’ used to explore many of the top+ V processes considers two same-sign (SS) leptons, three leptons or even four leptons. These typically occur when at least one top quark decays leptonically and another lepton comes from the associated boson’s decay. This so-called multilepton channel benefits from low backgrounds from SM processes, which compensates for the small branching fraction. However, it has rare backgrounds that are challenging to evaluate, coming from non-prompt leptons produced in hadron decays or jets misidentified as leptons (collectively called

‘fake leptons’) and also from prompt electrons that have a misassigned charge (for the channel with SS leptons). The muon charge-misassignment rate is negligible.

The fake-lepton background in the multilepton channel is usually evaluated using data-driven techniques. A common procedure is to use the ‘matrix method’ [141]. It uses two types of events: events with ‘loose’ selected leptons and events with ‘tight’ selected leptons, where loose leptons are defined by loosening or inverting some of the selection criteria so as to increase the fraction of fake leptons. This method is based on the fact that the numbers of events selected by using either the loose or tight lepton criteria can be expressed as linear combinations of the numbers of events with either prompt or fake leptons, using the fraction of prompt loose leptons meeting the tight criteria (tight lepton efficiency) and the fraction of fake loose leptons also meeting the tight criteria (lepton fake rate). Knowing this efficiency and fake rate (as well as the numbers of selected loose and tight leptons), the numbers of prompt and fake leptons can be extracted by inverting these relations. The efficiency and fake rate are measured in data using control regions enriched in either prompt or fake leptons. When using this method, the key step is to select control regions that are kinematically representative of the signal region so that the measured efficiency and fake rate can be applied in the signal region. Another way to estimate the non-prompt-lepton background is the ‘template method’ [142]. This method relies on the simulation to model the kinematic distributions of fake-lepton background processes and on control regions enriched in fake leptons to determine their normalisations. There are usually several control regions, enriched in fake leptons from different sources (such as electrons from photon conversions or leptons from heavy-flavour hadron decays). These control regions are then included, together with the signal region, in the fit that extracts the signal, and normalisation factors for the fake-lepton backgrounds are determined simultaneously with the signal strength (defined as the ratio of the measured cross-section to the SM prediction).

The other background usually evaluated from data is the one where the reconstruction assigns the wrong charge sign to an electron in the case where events with two SS leptons are selected. This happens when the electron undergoes a hard bremsstrahlung followed by an asymmetric photon conversion or when the sign of the electron track’s curvature is mismeasured. To suppress this background, another multivariate BDT was used, taking as input the track and energy-cluster properties of the electron candidate [29]. The charge misassignment rate was measured from the fraction of reconstructed $Z \rightarrow ee$ data events with a same-charge electron pair. It was parameterised as a function of the electron p_T and η and then applied to data events satisfying the signal selection where two leptons with opposite charges are required.

5.1 Top-quark production in association with a W or Z boson

Studying the $t\bar{t}Z$ process provides a direct probe of the weak couplings of the top quark. The coupling of the top quark to the Z boson is not yet well constrained, leaving room for potential new-physics contributions. Top-quark pair production in association with a W boson is an irreducible source of SS dilepton pairs. It is charge asymmetric in pp collisions because it is initiated by quark–antiquark initial states, and is unusually complex to predict because of the importance of higher-order QCD and EW corrections. Although the $t\bar{t}Z$ and $t\bar{t}W$ processes were not observed individually in Run 1, the $t\bar{t} + V$ production process (with $V = Z$ or W) was observed at $\sqrt{s} = 8$ TeV [143], reaching a precision of $\sim 30\%$. At $\sqrt{s} = 13$ TeV, the expected SM $t\bar{t}Z$ ($t\bar{t}W$) production cross-section increases by a factor of more than 3 (2). The Run 2 data sample made precise measurements possible, and also opened the door to differential measurements exploring $t\bar{t}Z$ and $t\bar{t}W$ kinematic modelling for the first time. ATLAS performed measurements in the multilepton channel coherently for both the $t\bar{t}Z$ and $t\bar{t}W$ signals, first using 3.2 fb^{-1} of $\sqrt{s} = 13$ TeV data [144] and then using 36 fb^{-1} [145]. The full Run 2 dataset was later used to study these processes differentially [146, 147].

Using 36 fb^{-1} of $\sqrt{s} = 13 \text{ TeV}$ data, the $t\bar{t}Z$ and $t\bar{t}W$ cross-sections were measured simultaneously [145] using SS dilepton events, trilepton events (3L), opposite-sign (OS) dilepton events and four-lepton events (4L). The OS dilepton region targets $t\bar{t}Z$ events where both top quarks decay hadronically and the Z boson decays into a pair of leptons. It suffers from a large background of Z +jets and $t\bar{t}$ events. BDTs were used to separate signal from background. The SS dilepton region targets the $t\bar{t}W$ process, with one top quark and the W boson decaying leptonically. It was split according to the charge of the selected lepton pairs since $t\bar{t}W$ events are preferentially produced with a positively charged W boson. The 3L channel is sensitive to both $t\bar{t}Z$ and $t\bar{t}W$ events. The 4L channel targets $t\bar{t}Z$ events where both the $t\bar{t}$ pair and the Z boson decay leptonically. The $t\bar{t}Z$ and $t\bar{t}W$ signal strengths were extracted simultaneously using a binned maximum-likelihood fit to all the control and signal regions. Since they are important backgrounds, the normalisations of the WZ , ZZ and Z +heavy-flavour-jets processes are determined from data control regions. The results are $\sigma_{t\bar{t}Z} = 950 \pm 80 \text{ (stat.)} \pm 100 \text{ (syst.)} = 950 \pm 130 \text{ fb}$ and $\sigma_{t\bar{t}W} = 870 \pm 130 \text{ (stat.)} \pm 140 \text{ (syst.)} = 870 \pm 190 \text{ fb}$ in agreement with SM predictions of $\sigma_{t\bar{t}Z} = 863^{+78}_{-89} \text{ fb}$ from NLO QCD including EW corrections and NNLL resummation [148] and $\sigma_{t\bar{t}W} = 745.3 \pm 54.9 \text{ fb}$ [149] from NNLO QCD with NLO EW corrections.

With the full Run 2 dataset, differential $t\bar{t}Z$ [147, 150] and $t\bar{t}W$ [146] measurements were carried out in independent analyses. The latest $t\bar{t}Z$ measurement was performed in three final states: the dilepton, 3L and 4L channels. The Z +jets background was estimated using simulation. However, since the modelling of Z +jets with heavy-flavour jets is challenging, the normalisations of the $Z + b$ and $Z + c$ components were obtained in data, simultaneously with the extraction of the signal strength. The $t\bar{t}$ background was estimated using a fully data-driven method, relying on the high $t\bar{t}$ purity of a sample requiring one electron and one muon. A deep neural network (DNN) was trained in each of the regions to extract the $t\bar{t}Z$ signal. Some of the input variables for this DNN were built using the output of the $t\bar{t}$ -system reconstruction. In all channels, the background from fake/non-prompt leptons was estimated using the template method. The inclusive signal strength was extracted by fitting the DNN output distributions simultaneously in all three channels using a profile-likelihood technique. The cross-section was measured to be:

$$\sigma_{t\bar{t}Z} = 860 \pm 40 \text{ (stat.)} \pm 40 \text{ (syst.)} = 860 \pm 60 \text{ fb},$$

where the largest systematic uncertainty comes from background normalisations. In addition, normalised and absolute differential distributions sensitive to the $t\bar{t}Z$ vertex (and hence interesting for constraining some EFT operators) were extracted in the 3L and 4L channels. The dilepton channel was not used because of its large background contamination. To correct for acceptance and detector effects, the differential distributions were unfolded using a profile-likelihood unfolding technique. The differential observables include the transverse momentum and absolute rapidity of the Z boson (see Figure 9 (a)), the transverse momentum or invariant mass of the top or $t\bar{t}$ system, and the azimuthal angle $\Delta\phi$ or rapidity difference between the Z boson and the leptonically decaying top quark. Most observables were measured at both parton and particle level. The compatibility of the unfolded measurements with various predictions was assessed by computing a χ^2 per degree of freedom and its corresponding p -value. In all cases, the p -values indicate good agreement between the unfolded data and the predictions. The particle-level distributions were used to constrain EFT effects in $t\bar{t}Z$ production (see Section 9). Furthermore, detector-level observables sensitive to polarisation and spin correlation of the top quarks were combined to explore spin correlations in $t\bar{t}Z$ production. Simulated templates of $t\bar{t}Z$ events with and without spin correlation were used to extract a ratio of the measured spin correlation to the SM prediction in $t\bar{t}Z$ events of $f_{\text{SM}} = 1.20 \pm 0.68$. The total uncertainty is dominated mainly by its statistical component. This result is in agreement with the SM, and represents a 1.8σ departure from a scenario without spin correlations.

The full Run 2 dataset was also used to explore the $t\bar{t}W$ process differentially for the first time, studying the kinematics of $t\bar{t}W$ final-state particles and of any associated jets [146] in the channel with SS dilepton events and the 3L channel. Beyond the interest in measuring this rare process more precisely, a better understanding of $t\bar{t}W$ production is important since indirect measurements in analyses targeting $t\bar{t}H$ or $t\bar{t}\bar{t}\bar{t}$ production have consistently observed larger $t\bar{t}W$ yields than the SM predicts in the $t\bar{t}W$ phase space with additional jets. The signal regions were split by lepton charge. An inclusive cross-section was extracted by further splitting them by lepton flavour and both the jet and b -tagged-jet multiplicities. Control regions were defined in order to adjust the normalisation of the fake-lepton backgrounds, as well as the diboson and $t\bar{t}Z$ backgrounds. These control regions were defined to be orthogonal to the signal regions by applying looser lepton isolation criteria or requiring a different number of jets or b -tagged jets. The normalisations obtained from the fit are compatible with unity. The inclusive cross-section was measured to be:

$$\sigma_{t\bar{t}W} = 880 \pm 50 \text{ (stat.)} \pm 70 \text{ (syst.)} = 880 \pm 80 \text{ fb,}$$

with the largest systematic uncertainty coming from the modelling of the $t\bar{t}W$ signal. This result is higher than the SM prediction in Ref. [149], but compatible with it at the level of 1.4 standard deviations. Separate $t\bar{t}W^+$ and $t\bar{t}W^-$ cross-sections were also measured, together with their ratio and the relative charge asymmetry. Differential $t\bar{t}W$ measurements were performed as a function of observables where discrepancies were observed previously or that are sensitive to NLO corrections. These include the number of jets (see Figure 9 (b)), the scalar sum of the transverse momenta of jets, and separately of leptons, and the azimuthal angle and rapidity difference between the two same-sign leptons. The corrections to particle level were obtained using a profile-likelihood unfolding. As expected from the inclusive case, the absolute differential measurements exceed the theoretical predictions. The normalised distributions, however, show rather good χ^2 compatibility with the MC generator predictions. The total uncertainty, dominated by data statistics, does not currently allow the modelling performed in the MC simulation to be constrained significantly.

The process with a single Z boson and a top quark in the final state (tZq) is another way to probe the coupling of the top quark to the Z boson. Despite an expected cross-section ten times smaller than that for $t\bar{t}Z$, this process probes two electroweak couplings in a single process: the t - Z and W - Z couplings. Evidence for tZq production was seen with the 36 fb^{-1} data sample [151], while the full Run 2 dataset allowed a definitive observation [152] as described in the following. The expected tZq SM cross-section at NLO in QCD (with a dilepton invariant mass $m_{\ell\ell} > 30 \text{ GeV}$) is 102^{+5}_{-2} fb , computed using MCFM [153]. The tZq process was searched for in the 3L channel, requiring one b -tagged jet and one additional non- b -tagged jet, which is expected to be emitted preferentially at high absolute pseudorapidity. A third jet coming from radiation was also allowed. To help separate the signal from the diboson, Z +jets and $t\bar{t}$ backgrounds, both the Z -boson and the top-quark invariant masses were reconstructed. Diboson, $t\bar{t}Z$ and $t\bar{t}$ control regions were defined in order to adjust the background normalisations or to help constrain their uncertainties. The contribution from non-prompt-lepton background was estimated by replacing one b -tagged jet by a lepton in the $t\bar{t}$ and Z +jets MC event samples. The signal was separated from the background by using a neural network where the most discriminating input variable is the largest invariant mass formed by the b -tagged jet and one of the untagged jets. The signal strength was extracted from a maximum-likelihood fit together with the normalisations of the $t\bar{t}$ and Z +jets backgrounds and leads to:

$$\sigma_{tZq} = 97 \pm 13 \text{ (stat.)} \pm 7 \text{ (syst.)} = 97 \pm 15 \text{ fb,}$$

for $m_{\ell\ell} > 30 \text{ GeV}$, in agreement with the SM prediction. The statistical significance of the result is well above five standard deviations relative to the background-only hypothesis, which establishes observation of this rare process using $\sqrt{s} = 13 \text{ TeV}$ data.

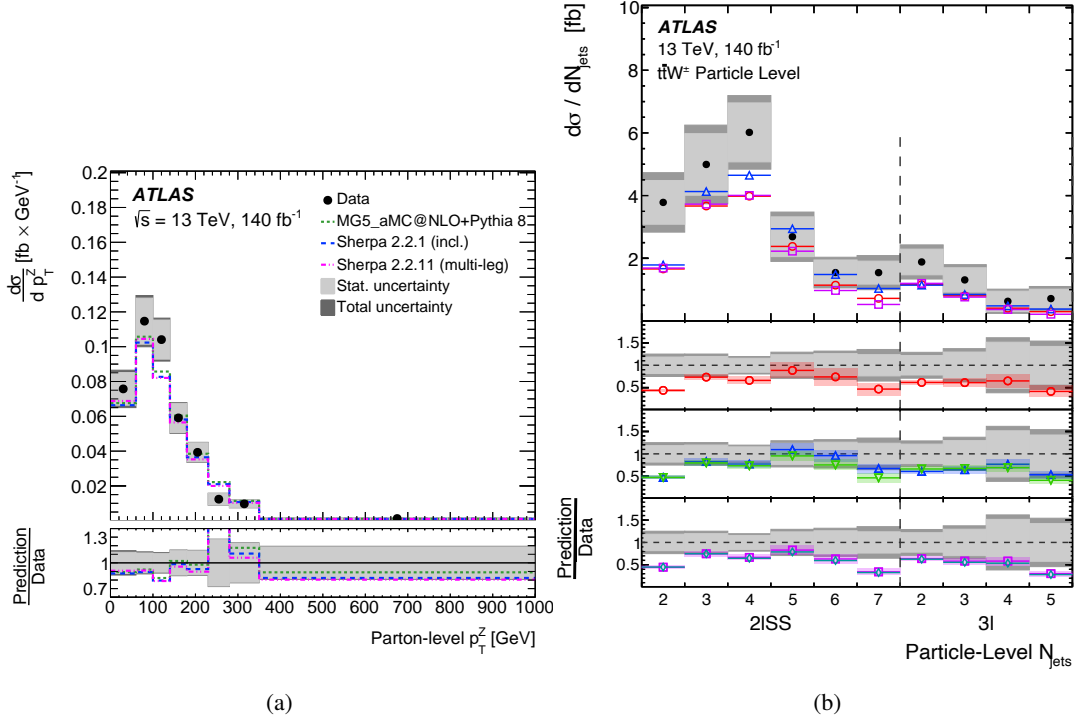


Figure 9: (a) Absolute differential $t\bar{t}Z$ cross-section measurement as a function of the transverse momentum of the Z boson [147]. (b) Unfolded distribution of the absolute $t\bar{t}W$ cross-section as a function of jet multiplicity [146].

5.2 Top-quark production in association with a photon

The top quark's coupling to a photon is tested through the measurement of $t\bar{t}\gamma$ production and its kinematic properties. For instance, the transverse momentum of the photon would be affected by anomalous dipole moments of the top quark [154–156] or by EFT operators. At the LHC, $t\bar{t}\gamma$ production was already observed in $\sqrt{s} = 7$ TeV pp collisions [157] and the first differential measurements were performed at $\sqrt{s} = 8$ TeV [158]. At $\sqrt{s} = 13$ TeV, benefiting from larger data samples, further differential distributions were explored, first using 36 fb^{-1} of data [159] and then the full Run 2 dataset [160]. One challenge in the $t\bar{t}\gamma$ analyses is due to the fact that the photon can originate not only from the top quark but also from its charged decay products, which would dilute the information about the $t\gamma$ coupling. Although separating these sources is difficult, some kinematic variables such as the angular separation between a lepton and photon in the event can help. Another challenge in such analyses is the accurate simulation of the signal. Samples could be produced either inclusively without explicitly including a photon in the final state (but where photons are generated through initial- or final-state radiation), or with photons at the matrix-element level, taking the whole decay chain into account at LO. The overlap between these two kinds of samples then needs to be removed. The $t\bar{t}\gamma$ process also interferes with the singly resonant $tW\gamma$ process, similarly to the interference of the $t\bar{t}$ and tW processes. NLO calculations are available in dedicated phase spaces, i.e. with specific photon kinematic requirements [161–163]. Hence, in order to accurately compare the data with theory computations, the analyses need to be performed in the same phase space. The first Run 2 analysis, using 36 fb^{-1} , exploited both the semileptonic and dileptonic decays of the $t\bar{t}$ pair. The analysis using the full 139 fb^{-1} dataset [160] focused on the clean $e\mu$ final state so that no multivariate technique had to be used to extract the signal. It also measured the combined resonant $t\bar{t}\gamma$ and non-resonant $tW\gamma$

production cross-section in order to compare it with the NLO QCD predictions in Refs. [162, 163]. Apart from the backgrounds with prompt photons (such as $W\gamma$ and $Z\gamma$), there are two sources of background with misidentified photons: hadron-fakes (photons mimicked by hadronic energy deposits, or non-prompt photons from hadron decays) and electron-fakes (electrons mimicking photon signatures). In this analysis, they were both estimated using MC samples since the studies performed with data-driven techniques in the 36 fb^{-1} analysis [159] showed that possible data-driven corrections have a negligible effect on the distribution shapes of relevant observables. The background from electron-fakes is a minor background contribution in the analysis. The fiducial inclusive cross-section was extracted using a profile-likelihood fit of the distribution of the scalar sum of all transverse momenta in the event, including leptons, photons, jets and missing transverse momentum. This observable was found to provide good separation between signal and background without too much sensitivity to systematic uncertainties. The fiducial region's definition required one electron and one muon, as well as two b -jets, and one photon with $E_T > 20 \text{ GeV}$ and $|\eta| < 2.37$ at parton level. The combined $t\bar{t}\gamma/tW\gamma$ cross-section was measured to be:

$$\sigma_{\text{fid}}(t\bar{t}\gamma \rightarrow e\mu b\bar{b}\gamma) = 39.6 \pm 0.8 \text{ (stat.) } {}^{+2.6}_{-2.2} \text{ (syst.) fb} = 39.6 {}^{+2.7}_{-2.3} \text{ fb},$$

in good agreement with the dedicated theoretical calculation: $38.5 {}^{+1.2}_{-2.5} \text{ fb}$ [162, 163]. The systematic uncertainties with the largest impact come from the uncertainties in modelling the signal. The absolute and normalised differential cross-sections were measured as a function of the kinematics of the photon, the angular separation between the photon and the leptons, and the pseudorapidity difference and azimuthal angle between the two leptons. The last two of these are particularly sensitive to $t\bar{t}$ spin correlations. The unfolded distributions generally agree well with the predictions, except for the shape of the angular separation between the leptons and the photon or the azimuthal angle between the two leptons, which are not well modelled by the LO MC predictions. The NLO prediction provides a better description of these distributions. The dominant uncertainty in these differential measurements still comes from the size of the data sample, at a level slightly below 10%.

Analogously to the t - Z coupling, the coupling between the top quark and a photon can also be studied in the single-top process $tq\gamma$, featuring a forward light-quark jet characteristic of t -channel production. Analysing the full $\sqrt{s} = 13 \text{ TeV}$ dataset led to the first observation of this process [164]. The $tq\gamma$ cross-section was measured in a fiducial phase space either at parton level, excluding contributions where photons are radiated from the charged decay products, or at particle level, including these contributions. Two signal regions were defined according to the presence or absence of a forward jet. Control regions were included to normalise the large background from $t\bar{t}\gamma$ production and the $W\gamma$ background. A neural network was trained to separate signal from background by using the reconstructed top-quark mass as the most discriminating input variable. The measured fiducial cross-section (requiring one electron or muon, one b -jet, and one photon with p_T greater than 20 GeV) is:

$$\sigma_{\text{fid}}(tq\gamma) = 688 \pm 23 \text{ (stat.) } {}^{+75}_{-71} \text{ (syst.) fb} = 688 {}^{+78}_{-75} \text{ fb},$$

which is 2.1 standard deviations above the SM NLO QCD prediction of $515 {}^{+36}_{-42} \text{ fb}$ from MADGRAPH5_AMC@NLO. The largest systematic uncertainty comes from the modelling of the $t\bar{t}\gamma$ background. The observed (expected) significance of the $tq\gamma$ signal relative to the background-only hypothesis is 9.3 (6.8) standard deviations, establishing observation of this process.

5.3 Four-top-quark production

The Run 2 data sample also gave access to four-top-quark production, which is one of the rarest and heaviest-final-state processes now accessible at the LHC, with a combined particle rest mass of almost

700 GeV. The Run 2 dataset is expected to contain around 1700 four-top-quark events. This multiparticle SM process presents a promising avenue to search for signals of new physics beyond the SM. For example, the $t\bar{t}t\bar{t}$ cross-section could be enhanced in top-quark-compositeness models [165] or by gluino pair production in supersymmetric theories [166, 167]. Within the EFT approach, four-top-quark production is uniquely sensitive to four-top-quark operators. Because of the existence of electroweak $t\bar{t}t\bar{t}$ Feynman diagrams where the production of a pair of top quarks is mediated by a Higgs boson, $t\bar{t}t\bar{t}$ production is also sensitive to the top-quark Yukawa coupling and its CP properties [168, 169]. Measuring the four-top-quark production cross-section is interesting in its own right since experimental results will challenge the state-of-the-art perturbative QCD calculation techniques. Within the SM the predicted $t\bar{t}t\bar{t}$ cross-section in pp collisions at a centre-of-mass energy of $\sqrt{s} = 13$ TeV is $\sigma_{t\bar{t}t\bar{t}} = 12.0 \pm 2.4$ fb [170–172] at NLO in QCD including NLO electroweak corrections. This value does not include the effect of threshold resummation at next-to-leading-logarithm accuracy, which increases the total production cross-section by approximately 12% and reduces the scale uncertainty [173]. This corresponds to about a factor of 10 enhancement relative to the $t\bar{t}t\bar{t}$ cross-section at $\sqrt{s} = 8$ TeV, demonstrating the new perspective offered by 13 TeV collisions.

The analysis was first performed in the channel with two SS leptons or at least three leptons. This channel corresponds to 12% of the total $t\bar{t}t\bar{t}$ production cross-section, and offers the best discovery potential. First, a search for new phenomena targeted vector-like quark and SS top-quark pair production, and placed an upper limit on SM $t\bar{t}t\bar{t}$ production using 36 fb^{-1} of Run 2 data [174]. Later, dedicated analyses focusing on SM production were developed, finding first evidence for $t\bar{t}t\bar{t}$ production using the full 139 fb^{-1} Run 2 dataset [175]. With the same dataset but with improvements in object reconstruction, calibration and selection criteria, new analysis techniques and a better understanding of major background processes and systematic uncertainties, this process was first observed [176] as described in the following. Backgrounds in the multilepton-channel $t\bar{t}t\bar{t}$ analysis arise almost entirely from previously described top+ V processes (i.e. $t\bar{t}W$, $t\bar{t}Z$, and $t\bar{t}H$ production) when they produce additional jets. These backgrounds with prompt leptons were estimated using MC simulation. Because the theoretical modelling of the $t\bar{t}W$ background at high jet multiplicity suffers from large uncertainties and since, as described above, the measured inclusive $t\bar{t}W$ cross-section is higher than the SM expectation, a data-driven estimation of this important background was implemented. The overall normalisation of the $t\bar{t}W$ background and the parameters of the scaling as a function of jet multiplicity were determined from dedicated control regions together with the signal. The fake-lepton backgrounds were evaluated using the template method. The $t\bar{t}t\bar{t}$ signal was separated from the background events using a multivariate discriminant built with a graph neural network (GNN). The $t\bar{t}t\bar{t}$ production cross-section and the normalisation factors for the backgrounds were determined via a binned likelihood fit to the GNN score distribution in the signal region while also using control regions, with systematic uncertainties included as nuisance parameters. The measured $t\bar{t}t\bar{t}$ production cross-section is:

$$\sigma(t\bar{t}t\bar{t}) = 22.5^{+4.7}_{-4.3} \text{ (stat.) }^{+4.6}_{-3.4} \text{ (syst.) fb} = 22.5^{+6.6}_{-5.5} \text{ fb.}$$

The significance of the observed (expected) signal is found to be 6.1 (4.3) standard deviations relative to the background-only hypothesis, providing the first observation of this process [176].

The measured production cross-section is consistent with the SM prediction to within 1.8 standard deviations. Several limits on four-heavy-flavour-fermion EFT operators were also set using this measurement (see Section 9). In addition to $t\bar{t}t\bar{t}$ production being dependent on the top Yukawa coupling, the $t\bar{t}H$ background is a function of the same coupling. The GNN distribution was therefore used to extract limits on the top Yukawa coupling's strength modifier κ_t , leading to $\kappa_t < 1.8$ (assuming a CP -even coupling). This limit is less stringent than the ones derived from specific Higgs boson studies [177, 178] but is less model

dependent, without any assumption about the Higgs boson’s width. This $t\bar{t}\bar{t}$ analysis also derived 95% confidence level (CL) intervals for the cross-section of the $t\bar{t}$ process, which has an experimental signature and kinematic properties very similar to those of $t\bar{t}t$ events. This process, composed of two components $t\bar{t}q$ and $t\bar{t}W$, has an expected SM cross-section that is about 10 times smaller than for $t\bar{t}t$, and has not yet been observed. More data and more dedicated analyses will be needed to constrain this very rare process.

Although it is significantly less sensitive, a $t\bar{t}t$ measurement was also performed in events with a single lepton or two OS leptons, first as a search for heavy new particles [179] using 36 fb^{-1} , and then targeting the SM process with the full $\sqrt{s} = 13 \text{ TeV}$ dataset [180]. These final states have much higher branching fractions (about 57% of the $t\bar{t}t$ events) but considerable background from top-quark pair production with additional jets. Since the background in the high jet-multiplicity regions was found to be mismodelled by MC simulation, a strategy was developed to use data to sequentially reweight the $t\bar{t}$ MC generation in several observables to obtain a reliable $t\bar{t}$ +jets estimate. The different $t\bar{t}$ +jets components after reweighting ($t\bar{t}$ +light, $t\bar{t}+\geq 1c$ and $t\bar{t}+\geq 1b$ jets) were further adjusted and constrained in a binned profile-likelihood fit which extracted the signal strength. In the region most sensitive to $t\bar{t}t$ production, BDTs were used to discriminate between signal and background events. The systematic uncertainties in the $t\bar{t}$ background prediction were evaluated with special care since these uncertainties have the largest impact on the measurement sensitivity. The $t\bar{t}t$ cross-section was measured to be $\sigma(t\bar{t}t) = 26 \pm 8 \text{ (stat.)}_{-13}^{+15} \text{ (syst.) fb} = 26_{-15}^{+17} \text{ fb}$, which corresponds to an observed significance of 1.9 standard deviations relative to the background-only hypothesis (while 1.0 standard deviations was expected). This result is compatible with the result in the multilepton channel.

Now that the $t\bar{t}t$ process has been observed, the next step, as already taken for $t\bar{t}Z$ and $t\bar{t}W$ production, will be to test the SM predictions differentially with $t\bar{t}t$ events and to better constrain the small but hard to separate $t\bar{t}$ process.

The $\sqrt{s} = 13 \text{ TeV}$ inclusive top+ X cross-section measurements are summarised in Figure 10. As described above, a lot of the top+ V processes are intertwined, so a strategy to evaluate all of their cross-sections coherently is needed to generically constrain new physics [181]. In order to combine the analyses in the future, this would require the different analyses to harmonise how they define the reconstructed objects used in their selection criteria, harmonise their systematic uncertainties, and harmonise the phase spaces defining their control and signal regions.

6 Top-quark mass

The large value of its mass, m_t , is probably the most peculiar property of the top quark. It is close to the electroweak scale and thus plays an important role in much of the dynamics of elementary particles via loop diagrams. In particular, it significantly affects the radiative corrections to both the Higgs boson’s mass and the W boson’s mass, providing a relationship that can be used for precision tests of the consistency of the SM [182].

Measurements of the top-quark mass are typically categorised into two families, often called ‘direct’ and ‘indirect’ measurements. Measurements relying on the reconstruction of the decay products of the top quark, building partial or total invariant-mass observables, are usually assigned to the first category, and are therefore sometimes referred to as ‘measurements from decay’. In contrast, extractions from total or differential cross-section measurements, relying on the dependence of theoretical predictions on the m_t parameter in the SM Lagrangian, belong to the second category, also referred to as ‘measurements

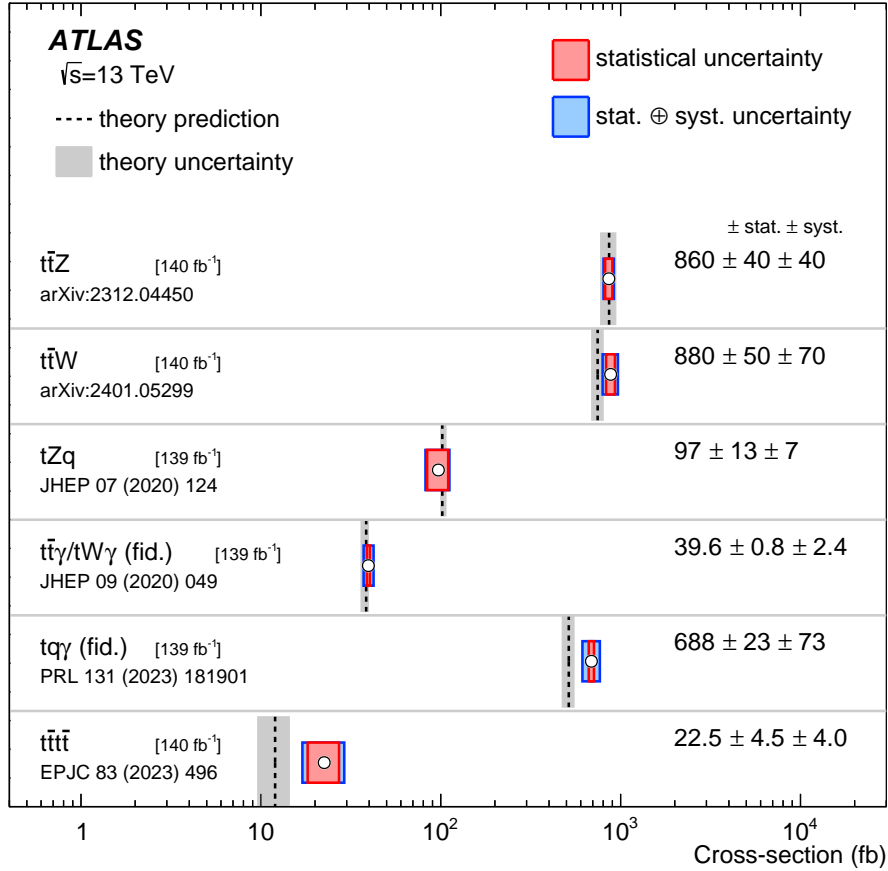


Figure 10: Summary of the $\sqrt{s} = 13$ TeV top+ X cross-section measurements and comparison with the corresponding theoretical expectations. The fiducial region used to measure the $t\bar{t}\gamma$ cross-section requires one electron, one muon, two b -jets and one photon at parton level. The $tq\gamma$ fiducial region is defined by requiring one electron or muon, at least one photon and at least one b -tagged jet at particle level.

from production’. The direct measurements typically have smaller uncertainties but inevitably rely on predictions from MC generators to relate the considered observable to a top-quark mass value. Interpreting these measurements in a well-defined renormalisation scheme is subject to additional uncertainties that are challenging to evaluate [183, 184]. In addition, the most precise direct top-quark mass measurements are affected by the relatively large uncertainties in the measurement of hadronic jet energies [185–187]. Alternatively, indirect measurements can be interpreted in a theoretically cleaner way, but are often affected by even larger uncertainties of both experimental and theoretical nature.

6.1 Direct top-quark mass measurements

The most precise experimental m_t determination by the ATLAS Collaboration was obtained through a combination of its Run 1 direct measurements, with the dominant contributions coming from the 8 TeV measurements in the dilepton [188] and lepton+jets [185] channels. In order to minimise the impact of the large jet-energy scale and $t\bar{t}$ modelling systematic uncertainties, the design of the two measurements took

orthogonal directions to some extent. In the dilepton channel, no attempt was made to fully reconstruct the top quark through its decay products, in order to avoid relying on the determination of the missing transverse momentum for the reconstruction of the two escaping neutrinos in each of the selected events. The m_t value was then extracted with an unbinned maximum-likelihood fit to the partial top-quark invariant mass formed by a charged lepton and the corresponding b -tagged jet, $m_{\ell b}$, after imposing a lower bound on the lepton- b -tagged-jet system's transverse momentum, optimised to minimise the uncertainty in the measurement. On the other hand, the measurement performed in the lepton-plus-jet channel relied on a simultaneous fit of three distributions: the top-quark and W -boson mass distributions as reconstructed by a kinematic fit in each event, and the distribution of the ratio of b -jet to light-jet transverse momenta. Thanks to these three variables, m_t could be extracted at the same time as two overall jet-energy correction factors for b -jets and light jets, with a consequent reduction of jet energy scale uncertainties via such in situ constraints. The combination of the two measurements, which were affected in different ways and in different directions by some of the most relevant sources of systematic uncertainty, could then benefit from this difference in design. The result is:

$$m_t = 172.69 \pm 0.25 \text{ (stat.)} \pm 0.41 \text{ (syst.) GeV,}$$

corresponding to a total uncertainty of 0.48 GeV. Combining this with similar measurements by the CMS Collaboration based on the Run 1 data collected at $\sqrt{s} = 7$ and 8 TeV [189], yields an even smaller uncertainty:

$$m_t = 172.52 \pm 0.14 \text{ (stat.)} \pm 0.30 \text{ (syst.) GeV.}$$

With the LHC providing a larger dataset in Run 2 than in Run 1, ATLAS had the opportunity to repeat some of the most precise measurements performed in Run 1 and also to investigate new methods for measuring the top-quark mass, using observables less sensitive to hadronic-jet energy determination. Using 36 fb^{-1} , ATLAS measured the top-quark mass using a purely leptonic observable, taking advantage of semileptonic decays of b -hadrons in top-quark decays [190]. In this analysis the idea is to select $t\bar{t}$ events where one of the two top quarks decays leptonically ($t \rightarrow Wb \rightarrow \ell\nu b$), and then to require the presence of a relatively soft muon within the hadronic jet formed in the b -quark fragmentation process. In this way, the partial top-quark invariant mass $m_{\ell\mu}$ could be built as the invariant mass of the system composed of the prompt charged lepton ℓ from the W -boson decay (considering either an electron or muon) and the 'soft' muon from the b -jet. Provided that the prompt lepton and soft muon originate from the same leg of the $t\bar{t}$ decay process, the $m_{\ell\mu}$ value is strongly correlated with the top-quark mass, while having only a small dependence on the jet reconstruction and energy determination.⁵ Soft muons were selected by requiring them to have an angular separation of $\Delta R < 0.4$ from a reconstructed jet. In order to reduce the rate of kaons misidentified as muons, as well as the contribution from $b \rightarrow c \rightarrow \mu$ decay chains (where b and c here represent generic b - and c -flavoured hadrons), soft muons were required to satisfy tight identification criteria and to have $p_T > 10$ GeV. The contamination from events where the two leptons come from different legs of the $t\bar{t}$ decay was mitigated by a cut on the angular distance between the prompt lepton and the soft muon. Finally, to control the residual $b \rightarrow c \rightarrow \mu$ contribution, due to its lower sensitivity to m_t , selected events were separated into two categories, depending on whether the two leptons have equal or opposite electric charge. The top-quark mass was then obtained from a simultaneous binned profile-likelihood fit of the $m_{\ell\mu}$ distribution in the two event categories, yielding:

$$m_t = 174.41 \pm 0.39 \text{ (stat.)} \pm 0.66 \text{ (syst.)} \pm 0.25 \text{ (recoil) GeV,}$$

⁵ A residual jet-energy uncertainty still affects the final result, due to the jet-related selection requirements that need to be applied in the analysis, in terms of event selection and soft-muon identification.

where the statistical uncertainty and the contribution from systematic uncertainties are indicated separately. This result is complementary to other more traditional direct top-quark mass measurements, as it is largely unaffected by jet energy scale uncertainties (with an impact of ± 0.13 GeV on m_t). However, uncertainties in both the perturbative and non-perturbative parts of the b -fragmentation process (i.e. in the so-called parton-shower evolution and fragmentation function) have a larger impact on the final result (~ 0.2 GeV), despite having been reduced by carefully retuning the parton-shower and hadronisation model in the MC simulation to the most precise e^+e^- data from LEP and SLD. Moreover, uncertainties in the b -hadron decay fractions to different final states make the largest contribution to the total uncertainty in m_t (± 0.4 GeV). In addition, studies have been performed, in contact with the theory community and MC experts, on the impact of the choice of recoil scheme in the simulation of the top-quark decay and successive QCD radiation off the b -quark. The impact of changing the default gluon-recoil scheme, from recoiling against the b -quark to recoiling against the W boson or against the top quark, was found to be sizeable. This affects the modelling of the second and subsequent gluon emissions from quarks produced by coloured-resonance decays and therefore changes both the fraction of jet energy carried by b -hadrons and the amount of radiation that fails to be clustered in b -jets. These studies were used to derive a corresponding uncertainty (named the recoil uncertainty), reported as the third contribution to the total uncertainty in the result quoted above. This uncertainty was not included in Run 1 measurements.

In parallel, ATLAS further developed the technique used for the most precise Run 1 m_t measurement, namely its extraction from the unbinned maximum-likelihood fit in the dilepton channel [191]. By taking advantage of the full 140 fb^{-1} Run 2 dataset, the analysis could be refined by optimising both the final-state reconstruction and the event selection in order to maximise the resolution of the defined observable and to minimise the impact of jet energy scale and $t\bar{t}$ modelling systematic uncertainties. In particular, a deep neural network (DNN) was trained to identify the best b -jet candidate to be assigned to each of the two charged leptons for the partial top-quark reconstruction. After this DNN-based lepton- b -jet (ℓb) pairing selects the two pairs, only the one with higher p_T is used to build the final observable, following the same rationale as was behind the optimised event selection in the Run 1 analysis. Similarly to Run 1, top-quark-mass templates were built from simulated $t\bar{t}$ events for the $m_{\ell b}$ observable. An unbinned maximum-likelihood fit to the observed data events was used to extract the central value of m_t , with systematic uncertainties being estimated by repeating the fit on varied pseudo-data samples. The resulting measurement is:

$$m_t = 172.21 \pm 0.20 \text{ (stat.)} \pm 0.67 \text{ (syst.)} \pm 0.39 \text{ (recoil) GeV,}$$

with the last component of the uncertainty representing the impact of the choice of recoil scheme in the top-quark decay, as in the previously discussed analysis. The other systematic uncertainties are dominated by jet energy scale and resolution uncertainties (with an impact of ~ 0.41 GeV on m_t) and by uncertainties in the matching scheme used between the NLO hard-scattering and parton-shower MC generators (± 0.4 GeV). Other important uncertainties are those from the initial- and final-state QCD radiation (± 0.17 GeV) and colour-reconnection modelling (± 0.27 GeV). The impact of the choice of recoil modelling is large and similar to the case of the previously described analysis, as it directly affects the fraction of energy carried by the undetected neutrino in the leptonic top-quark decay.

Figure 11 shows a comparison of the ATLAS Run 2 m_t measurements with the results of the combination of the ATLAS direct m_t measurements in Run 1 and of the combination of the ATLAS and CMS measurements. It can be seen how these Run 2 ATLAS measurements are affected by mostly uncorrelated sources of uncertainty. A possible gain can be foreseen from repeating the measurements on larger datasets or in different final states, as well as from performing an updated combination, including Run 1 measurements.

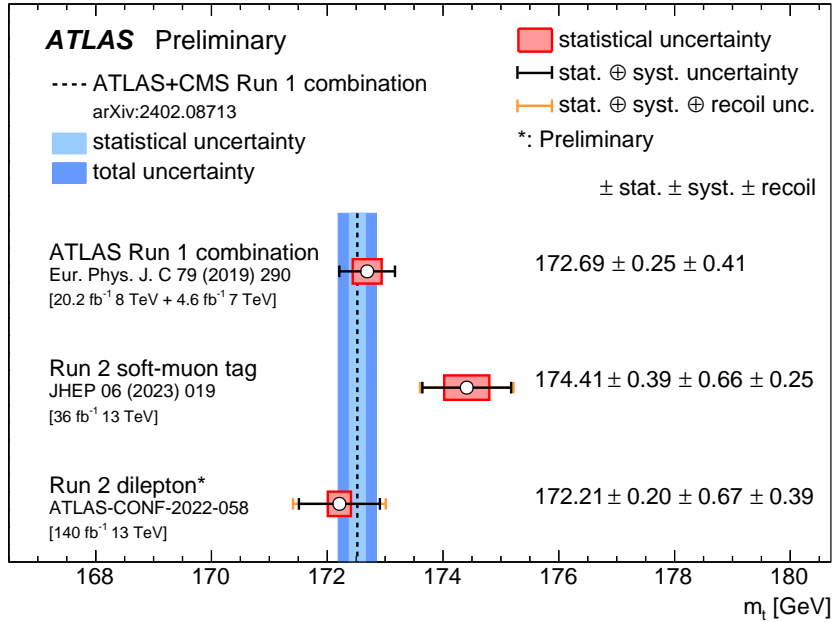


Figure 11: Summary of the most precise top-quark mass measurements performed by ATLAS in Run 1 and Run 2. The reference value shown by the vertical dashed line, with the blue bands indicating the statistical and total uncertainties, comes from the combination of the ATLAS and CMS Run 1 top-quark mass measurements. For each of the measurements, the uncertainty is broken down into a statistical uncertainty and a systematic uncertainty component, with the effect of the recoil modelling indicated separately for the Run 2 measurements (see text for more details).

6.2 Indirect top-quark mass measurements

For the indirect measurements, ATLAS took advantage of the improved precision in the determination of the inclusive $t\bar{t}$ cross-section (see Section 3) relative to Run 1. As reported in Ref. [82], the inclusive $t\bar{t}$ cross-section measurement in the dilepton $e\mu$ channel based on 36 fb^{-1} of Run 2 data was used to extract the top-quark pole mass via its effect on the predicted cross-section, yielding $m_t^{\text{pole}} = 173.1_{-2.1}^{+2.0} \text{ GeV}$. The result, obtained with CT14 as the reference PDF set, is dominated by uncertainties in the theoretical cross-section evaluated through PDF+ α_s and QCD-scale variations. Therefore, improved experimental measurement precision (such as that achieved in the updated cross-section measurement based on the full Run 2 dataset) would not have significant effects on this determination. Instead, extractions from differential cross-section measurements, especially when using the same technique as in the Run 1 top-quark mass measurement from $t\bar{t}+1$ -jet production [192] which obtained a precision of $\sim 1 \text{ GeV}$, have the potential to improve the precision of indirect determinations.

7 Top-quark properties

In addition to its very large mass, the top quark has other unique properties. Its decay width ($\Gamma_t \approx 1.4 \text{ GeV}$ [193]) is larger than the QCD hadronisation scale $\Lambda \approx 250 \text{ MeV}$, so the top quark decays before it

can form bound states, unlike other quarks. This unique feature allows its properties to be studied through its decay products.

Precisely predicted properties of top-quark decays are measured as a stringent test of the SM and as a probe of contributions from BSM physics. These include the polarisation of the W bosons produced in top-quark decays, the spin correlations and entanglement of top-quark pairs, and their forward–backward asymmetry. Additionally, top-quark decays are used both to test the modelling of QCD effects such as colour connection and as a source of W bosons to test the universality of their couplings to different lepton families.

These properties were studied extensively in Run 2 data, benefiting from a data sample much larger than the one from Run 1. As it is cleaner than the other channels, the dilepton channel was often used for these studies despite the reconstruction of top-quark kinematics being more complex there.

7.1 Top-quark decay angular properties

Since the top quark decays almost exclusively into a W boson and a b -quark, its decay products are naturally useful for studying the Wtb interaction vertex. This vertex and the masses of the interacting particles define the fractions of W bosons with longitudinal (f_0), left-handed (f_L), and right-handed (f_R) polarisation from the top-quark decays. Because of the vector minus axial-vector ($V - A$) nature of the Wtb interaction, f_R is expected to be very small, making it particularly sensitive to signs of new physics. The helicity fractions are predicted at NNLO in QCD to be $f_0 = 0.687 \pm 0.005$, $f_L = 0.311 \pm 0.005$ and $f_R = 0.0017 \pm 0.0001$ [194], with $f_0 + f_L + f_R = 1$. These fractions could be altered by new physics processes, and deviations from the SM expectation can be parameterised in terms of dimension-six EFT operators affecting the Wtb vertex. The full Run 2 data sample was used to measure these fractions [195] in the dilepton $t\bar{t}$ final state. They are accessible through the normalised differential distribution of the cosine of the polar angle θ^* , defined as the angle between the momentum of the charged lepton from the W -boson decay and the reversed momentum of the b -quark from the top-quark decay, both calculated in the W boson’s rest frame. Measuring $\cos \theta^*$ requires the reconstruction of the $t\bar{t}$ kinematics, which is achieved by using the Neutrino Weighting method. Using top-quark and W -boson mass constraints, this method scans over the neutrino pseudorapidities to find two possible kinematic solutions that are the most compatible with the measured E_T^{miss} of the event. Unlike the $\sqrt{s} = 8$ TeV results, which were obtained using a template method applied to detector-level distributions, the W helicity fractions in the $\sqrt{s} = 13$ TeV analysis were extracted by unfolding the normalised differential $\cos \theta^*$ distribution to parton level and fitting the unfolded cross-section distribution, minimising the χ^2 value. In the fit, the f_0 parameter was set to $f_0 = 1 - f_L - f_R$. The results are $f_0 = 0.684 \pm 0.005(\text{stat.}) \pm 0.014(\text{syst.})$, $f_L = 0.318 \pm 0.003(\text{stat.}) \pm 0.008(\text{syst.})$, and $f_R = -0.002 \pm 0.002(\text{stat.}) \pm 0.014(\text{syst.})$ in agreement with the SM predictions to within one standard deviation. The systematic uncertainty dominates the total uncertainty for all three helicity fractions. The largest systematic uncertainty arises from the uncertainty in $t\bar{t}$ modelling, so better understanding of the $t\bar{t}$ MC simulation would be needed to improve this measurement.

Top-quark pair production at the LHC is mostly mediated by the parity-invariant strong interaction, so the top quarks and antiquarks are predicted to be produced unpolarised in the SM, while the spins of the top quark and top antiquark are expected to be correlated. Since the spin correlation is transferred to their decay products, and almost maximally to the two leptons [196], the study can be performed with the leptons from the top-quark and top-antiquark decays. The dilepton channel is particularly relevant for measuring spin correlations because, in addition to their sensitivity to spin correlations, charged leptons are easy to identify in hadron collisions. This correlation has been observed experimentally at the LHC using both

$\sqrt{s} = 7$ TeV [197, 198] and 8 TeV [199, 200] collisions, showing slightly stronger correlation than expected, although with rather large experimental uncertainties. Studies of spin correlation at $\sqrt{s} = 13$ TeV with large datasets are therefore particularly relevant. Using 36 fb^{-1} of $\sqrt{s} = 13$ TeV data, ATLAS performed a measurement in the channel with one electron and one muon [201]. The full spin information of the top quarks is encoded in the spin density matrix [202]. The simplest observable sensitive to spin correlation is the azimuthal opening angle $\Delta\phi$ between the electron and the muon in the transverse plane, measured in the laboratory frame. The spin correlation measurement can be performed inclusively, but also in different $t\bar{t}$ invariant-mass bins since the degree of correlation is expected to vary with the $t\bar{t}$ invariant mass. The $\sqrt{s} = 13$ TeV analysis also utilised the difference between the pseudorapidities of the two charged leptons as an additional observable, $\Delta\eta$. This observable is less sensitive to spin correlation than $\Delta\phi$ but, in addition to $\Delta\phi$, is useful when searching for the presence of supersymmetric top squarks with a mass close to the top-quark mass. The $t\bar{t}$ invariant mass was reconstructed using the Neutrino Weighting method. The $\Delta\phi$ and $\Delta\eta$ distributions were corrected to parton level and particle level using an iterative Bayesian unfolding, and the resulting absolute and normalised cross-sections were compared with predictions from NLO MC generators. The dominant systematic uncertainty in this measurement comes from the modelling of initial- and final-state radiation. The comparison revealed several shape effects, with data tending to be higher than the expectation at low $\Delta\phi$ or high $\Delta\eta$ (see Figure 12 (a)). The compatibility with the SM prediction was assessed using a template fit to the normalised parton-level cross-sections, with one template from dilepton $t\bar{t}$ events with SM spin correlation and one where spin correlation had been removed. Using the inclusive $\Delta\phi$ distribution, the extracted spin-correlation fraction is $f_{\text{SM}} = 1.249 \pm 0.024$ (stat.) ± 0.061 (syst.) $^{+0.067}_{-0.090}$ (theo.). When including the template's theoretical uncertainties, the measurement is 2.2 standard deviations higher than the SM expectation of $f_{\text{SM}} = 1$. The value of f_{SM} is observed to increase slightly as a function of the $t\bar{t}$ invariant mass, $m_{t\bar{t}}$, but no bin shows a significant deviation from the prediction, due to the still large statistical and systematic uncertainties, and the relatively poor $m_{t\bar{t}}$ resolution. Several cross-checks were performed to understand the sensitivity of the result to the limitations of the $t\bar{t}$ modelling, such as the impact of the narrow-width approximation, the impact of NNLO corrections, or the use of expanded NLO predictions. None of these alternative predictions agree completely with the measurements, even though including higher-order effects brings the predictions closer to the data. Studies with the full Run 2 dataset or during the future LHC runs, as well as improvements in the predictions, should shed further light on this difference. The double-differential distributions of $\Delta\phi$ in bins of $\Delta\eta$ were used to search for the pair production of supersymmetric top squarks. In the absence of a signal, top squarks with a mass between 170 GeV and 230 GeV were excluded for most of the allowed neutralino mass range.

Precise measurements of the $t\bar{t}$ spin density matrix in a very restricted phase space were recently proposed as a new laboratory to study quantum information properties, especially entanglement [203–207]. Entanglement is a feature of quantum mechanics, where two entangled particles cannot be described independently of each other. This has been observed in many systems but only at lower energy scales. The LHC provides the opportunity to study this effect at high energies and in systems composed of new elementary particles. The $t\bar{t}$ pair is a two-qubit system of two spin-1/2 fermions. Entanglement in top-quark pairs can be studied via the spin correlation between the produced top quark and top antiquark, using leptons from their decays as spin-analysing particles. When produced close to their production threshold (i.e. $m_{t\bar{t}} \approx 2m_t$), the $t\bar{t}$ pairs produced through gluon–gluon fusion are in a spin-singlet state. In this case, maximum entanglement between the top quark and top antiquark is expected. When the $t\bar{t}$ system has a larger mass, the entanglement is reduced (but restored at very high $t\bar{t}$ mass above around 1 TeV). A simple observable can signal the presence of entanglement close to the production threshold [203]: $D = -3\langle \cos \varphi \rangle$, where φ is the angle between the charged-lepton directions in the respective parent top-quark and top-antiquark

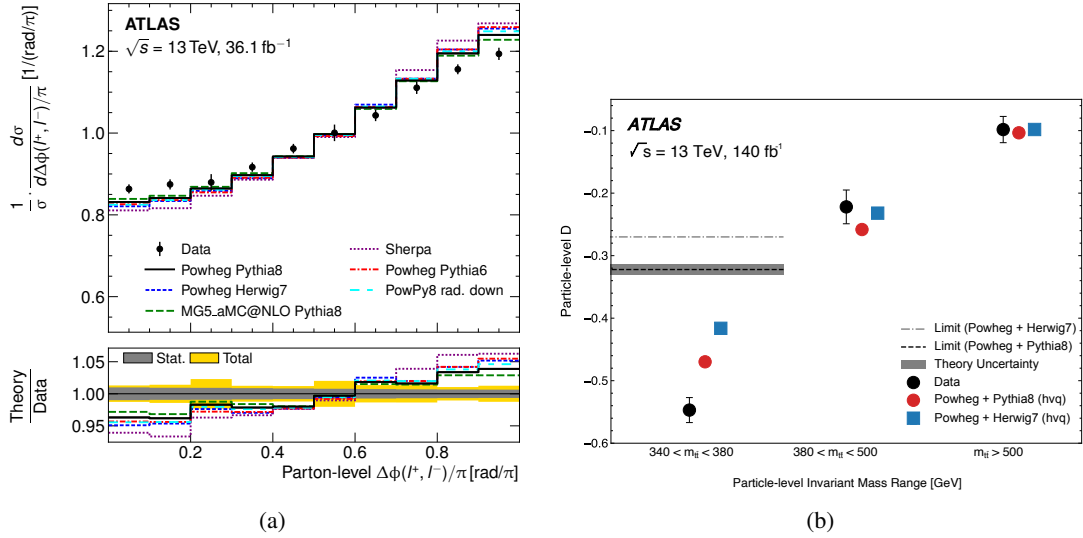


Figure 12: (a) The parton-level normalised $\Delta\phi$ differential cross-section compared with various predictions [201]. (b) Particle-level results for the measurement of the quantum entanglement observable D in the signal and validation regions, compared with various MC models [208].

rest frames. The existence of an entangled state is then demonstrated if $D < -1/3$. ATLAS performed the first study of quantum entanglement at high energy using $t\bar{t}$ events in the channel with one electron and one muon using the full Run 2 dataset at $\sqrt{s} = 13$ TeV [208]. The measurement of D requires the reconstruction of the top-quark and top-antiquark kinematics. The main method used in this analysis was the Ellipse method [209], which analytically calculates the unmeasured neutrino momenta through a geometrical approach. If the Ellipse method failed, the Neutrino Weighting method was used instead. The optimal window for the signal region was determined to be $340 < m_{t\bar{t}} < 380$ GeV at particle level. Two validation regions where entanglement is expected to be small were also defined to validate the method used for the measurement: one close to the threshold region ($380 < m_{t\bar{t}} < 500$ GeV) and one at higher $m_{t\bar{t}}$ ($m_{t\bar{t}} > 500$ GeV). The observed $\cos\varphi$ distribution at reconstruction level was corrected, after background subtraction, for distortions from the detector response and event selection by using a simple calibration curve that relates the reconstructed values to the corresponding particle-level values. The resulting value of D at particle level in a fiducial phase space is $D = -0.547 \pm 0.002$ (stat.) ± 0.021 (syst.). This value is compared with the entanglement limit at particle level, which was obtained by converting the parton-level bound of $D = -1/3$ to the particle-level equivalent taking into account parton-shower effects from the POWHEG+PYTHIA or POWHEG+HERWIG generators (see Figure 12 (b)). A large discrepancy between the predictions from these two generators is observed. However, in both cases the observed D value is well below the entanglement limit, beyond five standard deviations, establishing the discovery of an entangled $t\bar{t}$ state. This constitutes the first observation of entanglement in a quark–antiquark pair. The measurement paves the way for further studies of fundamental quantum mechanics at the LHC, such as measurements of quantum discord or the steering ellipsoid [210] or testing the Bell inequality in $t\bar{t}$ events [204, 211].

7.2 Asymmetry measurements

At leading order in QCD, $t\bar{t}$ production is symmetric under charge conjugation. However, at NLO, an asymmetry occurs between the top quark and the top antiquark. This asymmetry comes from the interference of initial-state and final-state radiation (ISR and FSR) diagrams and from the interference of the Born and box diagrams for quark–antiquark initial states: $q\bar{q} \rightarrow t\bar{t}$. As a result, the top quark (top antiquark) is preferentially emitted in the direction of the incoming quark (antiquark). Production via gluon–gluon fusion, $gg \rightarrow t\bar{t}$, which is dominant at the LHC, is charge symmetric at all orders. The asymmetry in $q\bar{q}$ manifests itself by the top antiquark being produced more centrally while the top quark is produced at more forward rapidities.

The charge asymmetry at the LHC can then be defined as:

$$A_C^{t\bar{t}} = \frac{N(\Delta|y| > 0) - N(\Delta|y| < 0)}{N(\Delta|y| > 0) + N(\Delta|y| < 0)},$$

with $\Delta|y| = |y_t| - |y_{\bar{t}}|$. Since $t\bar{t}$ production by gluon–gluon fusion, which is symmetric, dominates at the LHC, the inclusive asymmetry is expected to be small, of the order of 1%. For events where the top quark and antiquark decay leptonically, the leptons from the top quark or antiquark inherit the directions of their parent quarks, so a similar asymmetry can be defined using the pseudorapidities of the leptons via the $\Delta|\eta| = |\eta_{\ell^+}| - |\eta_{\ell^-}|$ observable. This leptonic charge asymmetry $A_C^{\ell\ell}$ is slightly diluted compared to $A_C^{t\bar{t}}$ but has the advantage of not requiring the kinematic reconstruction of the $t\bar{t}$ pair. It is also interesting to measure the asymmetries differentially as a function of kinematic variables of the $t\bar{t}$ system, such as the transverse momentum $p_T^{t\bar{t}}$, the invariant mass $m_{t\bar{t}}$, and the boost of the $t\bar{t}$ system in the z direction, $\beta_{z,t\bar{t}}$. In the SM, the charge asymmetries are expected to be enhanced for high values of some of these variables. Several BSM models predict a modification of the asymmetry, for instance by anomalous vector or axial-vector couplings (e.g. axigluons or a heavy Z' boson [212–215]). These modifications could also be studied with EFT [216]. In particular, BSM effects are expected to be enhanced in specific kinematic regions, such as in the phase space with large $\beta_{z,t\bar{t}}$ or large $m_{t\bar{t}}$ [217].

Asymmetry measurements in $t\bar{t}$ events were first performed at $\sqrt{s} = 8$ TeV [218], although with rather large uncertainties, around 60% of the predicted asymmetry. The fraction of $q\bar{q}$ -initiated top-quark pair production decreases with increasing centre-of-mass energy, and hence the $t\bar{t}$ charge asymmetry decreases as well. Despite this disadvantage, ATLAS measured $A_C^{t\bar{t}}$ in both the single-lepton and dilepton channels, and $A_C^{\ell\ell}$ in the dilepton channel, at $\sqrt{s} = 13$ TeV [219]. The lepton+jets channel was further split into resolved and boosted topologies. In the resolved case, the assignment of the jets to the corresponding partons from the decaying top quarks was assessed with a BDT that aims to discriminate between signal and the combinatorial background, separately for events with one or two b -tagged jets. In the boosted topology, the selected large-radius jet was taken to be the hadronically decaying top quark. In both cases, the semileptonically decaying top quark’s four-vector was reconstructed from the lepton and a small-radius jet, calculating the neutrino four-vector from the missing transverse momentum and the W -boson mass constraint. In the dilepton channel, the $t\bar{t}$ system was reconstructed using the Neutrino Weighting method. The differential $\Delta|y|$ distributions were corrected for acceptance and detector effects using the FBU method, where systematic uncertainties that affect the measurements are treated as nuisance parameters. The combined inclusive $A_C^{t\bar{t}}$ asymmetry from single-lepton and dilepton events was measured to be $0.0068 \pm 0.0010(\text{stat.}) \pm 0.0010(\text{syst.})$, in agreement with the SM calculation of $0.0064_{-0.0006}^{+0.0005}$ at NNLO accuracy in the strong coupling with NLO electroweak corrections [220]. The SM computation

was performed by expanding the numerator and denominator to a given order in perturbation theory. The measurement differs from zero by 4.7 standard deviations, providing strong evidence for $t\bar{t}$ charge asymmetry at the LHC. The precision of the result is dominated by the lepton+jets channel because of its smaller statistical uncertainty. The $A_C^{\ell\bar{\ell}}$ asymmetry, measured in the dilepton channel only, is $0.0054 \pm 0.0012(\text{stat.}) \pm 0.0023(\text{syst.})$, while the SM calculation at NLO in QCD, including NLO EW corrections, predicts $0.0040_{-0.0001}^{+0.0002}$ [221]. The combined $A_C^{t\bar{t}}$ results were interpreted in terms of EFT using new operators for four-quark interactions with different coupling chiralities (see Section 9). Differential $A_C^{t\bar{t}}$ measurements were performed as a function of $m_{t\bar{t}}$, $p_T^{t\bar{t}}$ and $\beta_{z,t\bar{t}}$, with the binning at larger values being finer than was possible for $\sqrt{s} = 8$ TeV data (see Figure 14 (a)). Differential measurements of $A_C^{\ell\bar{\ell}}$ were presented as a function of the invariant mass, transverse momentum and longitudinal boost of the dilepton pairs. The results were found to be compatible with the SM predictions.

Another way to study the $t\bar{t}$ charge asymmetry is to use an observable linked to the energy difference between the top quarks and antiquarks, $\Delta E = E_t - E_{\bar{t}}$. The energy asymmetry [222] occurs mainly through the $qg \rightarrow t\bar{t}q$ process, which is a more abundant source of events than the $q\bar{q} \rightarrow t\bar{t}$ process at the LHC. It is then expected to be larger than asymmetries based on rapidity. The presence of an additional jet allows QCD effects at leading order to be investigated, while the asymmetry in $q\bar{q} \rightarrow t\bar{t}$ only appears at NLO. In the $pp \rightarrow t\bar{t}j$ process, the energy asymmetry can be defined as a function of the jet angle θ_j :

$$A_E(\theta_j) = \frac{\sigma_{t\bar{t}j}(\theta_j|\Delta E > 0) - \sigma_{t\bar{t}j}(\theta_j|\Delta E < 0)}{\sigma_{t\bar{t}j}(\theta_j|\Delta E > 0) + \sigma_{t\bar{t}j}(\theta_j|\Delta E < 0)},$$

where $\sigma_{t\bar{t}j}(\theta_j)$ is the differential $t\bar{t}j$ cross-section as a function of θ_j . Both ΔE and θ_j are defined in the $t\bar{t}j$ rest frame, which corresponds to the partonic centre-of-mass frame in tree-level processes. ATLAS measured this energy asymmetry differentially using 139 fb^{-1} of $\sqrt{s} = 13$ TeV data [223]. The analysis was performed in the semileptonic $t\bar{t}$ decay channel. The number of events observed at detector level was corrected for detector effects to particle level using the FBU method. The uncertainty in the measurement is dominated by the statistical component. The measured differential distribution was found to be in good agreement with the SM expectation, with a p -value of 0.80. In the first bin, $0 \leq \theta_j \leq \pi/4$, the measured asymmetry differs from zero by 2.1 standard deviations. The sensitivity of this energy asymmetry measurement to new physics was investigated in the context of EFT (see Section 9). The energy asymmetry is particularly sensitive to the chirality and colour charges of the involved operators. It complements the constraints from asymmetries built using rapidities.

The large Run 2 data sample allows asymmetries to be measured in rarer processes where $t\bar{t}$ is produced with an associated gauge boson. Some of these processes are predicted to have a larger asymmetry than in $t\bar{t}$ production. For instance, the $t\bar{t}W$ process is initiated at LO by a $q\bar{q}'$ initial state. These $t\bar{t}W$ events can then serve as an interesting tool for measuring the $t\bar{t}$ charge asymmetry since it is expected to be larger than in $t\bar{t}$ production [224, 225]. In addition, the W boson in this process can be radiated from the $q\bar{q}'$ initial state, thereby serving as a way to polarise the $q\bar{q}'$ pair and thus also the $t\bar{t}$ pair. This polarisation further enhances the asymmetry between the decay products of the top quarks and top antiquarks, leading to an enhanced leptonic asymmetry. The drawback of using the $t\bar{t}W$ process is, however, its much smaller cross-section in comparison with $t\bar{t}$ production. Despite the challenges, ATLAS probed the asymmetry in $t\bar{t}W$ events using the full Run 2 dataset [226]. The measurement was performed in the 3L channel at detector level and also at particle level after unfolding. In order to compute $A_C^{\ell\bar{\ell}}$, the two opposite-sign leptons from the top-quark decays need to be separated from the one from the W decay. This was addressed by using a BDT. The second lepton needed to compute $A_C^{\ell\bar{\ell}}$ was taken to be the lepton with charge opposite

to that of the lepton selected by the BDT. A profile-likelihood fit was used to extract the signal, together with the normalisation of each of the most relevant background processes, i.e. $t\bar{t}Z$, non-prompt electrons and muons, and electrons from γ -conversions. The leptonic charge asymmetry in $t\bar{t}W$ events was measured to be $A_C^{\ell\ell}(t\bar{t}W) = -0.12 \pm 0.14(\text{stat.}) \pm 0.05(\text{syst.})$. The SM prediction from the SHERPA simulation [57] in this phase space is $-0.084_{-0.003}^{+0.005}(\text{scale}) \pm 0.006(\text{MC stat.})$. With the current precision, the result is compatible with zero and not yet sensitive to the SM asymmetry. The asymmetry was also unfolded to particle level in a fiducial phase space. The results are limited by statistical uncertainty, so they are expected to improve in the years to come.

The $t\bar{t}\gamma$ final state is also relevant for asymmetry measurements [227]. When the photon is emitted from the initial state, the process benefits from an enhanced fraction of quark–antiquark-initiated $t\bar{t}$ production relative to symmetric production via gluon–gluon fusion. In this process, the asymmetry arises through the interference of QED initial-state radiation and final-state radiation, which yields a negative asymmetry. The overall asymmetry in $t\bar{t}\gamma$ events at $\sqrt{s} = 13$ TeV is predicted in the SM to be between -1% and -2% depending on the phase space [228, 229]. The main challenge of studying the charge asymmetry in $t\bar{t}\gamma$ events comes from the fact that the asymmetry is only present for events where the photon is radiated from the initial-state parton or from the final-state top quark or antiquark. It is diluted by $t\bar{t}\gamma$ events where the photon is emitted from any of the charged decay products of the $t\bar{t}$ final-state system. ATLAS measured this charge asymmetry in $t\bar{t}\gamma$ production for the first time using the full 139 fb^{-1} dataset recorded at $\sqrt{s} = 13$ TeV [230] and the semileptonic $t\bar{t}$ decay channel. The top-quark and top-antiquark kinematic properties, in particular their rapidities, were reconstructed using the KLFFitter package. The estimation of background events with prompt or misidentified photons followed the methods developed for the measurement of the $t\bar{t}\gamma$ cross-section described in Section 5. A neural network was used to separate the $t\bar{t}\gamma$ signal from the background processes. The asymmetry value was extracted from the $\Delta|y_t| = |y_t| - |y_{\bar{t}}|$ distribution in a fiducial region at particle level after performing a maximum-likelihood unfolding. After the fit, the asymmetry was found to be $A_C^{t\bar{t}\gamma} = -0.003 \pm 0.024(\text{stat.}) \pm 0.017(\text{syst.})$ (assuming a SM charge asymmetry in $t\bar{t}$ events of $A_C^{t\bar{t}} = 0.0064$). The measured value is compatible with the result from NLO simulation in the same phase space: $A_C^{t\bar{t}\gamma} = -0.014 \pm 0.001$. The dependence of the measured $A_C^{t\bar{t}\gamma}$ on the asymmetry in $t\bar{t}$ events was also studied and found to be linear. Here also the result is still limited by the statistical uncertainty and so is expected to be improved in the future.

The different asymmetry measurements are summarised in Figure 13. They are in agreement with the SM predictions. The uncertainties in the SM predictions are much smaller than the current experimental uncertainties, which are dominated by statistical uncertainties, as systematic effects largely cancel out. Therefore, improvements in the experimental set-up, as well as the analysis of the larger datasets available after the completion of LHC Run 3 and at the HL-LHC, will lead to more valuable comparisons.

7.3 Tests of QCD

Top pair production also serves as a unique environment to test QCD and tune the modelling of QCD effects in MC generators. One of the aspects of QCD that can be tested with $t\bar{t}$ events is the modelling of radiation through colour connection and colour propagation, i.e. colour flow, which is modelled by colour strings between quarks and gluons. Experimentally, quarks and gluons appear as jets. The radiation emission pattern between particles, governing the structure of the jets, is affected by their colour connections. In particular, QCD predicts that there is more radiation between particles that are colour-connected. Experimental measurements are needed to validate the phenomenological description of such predictions.

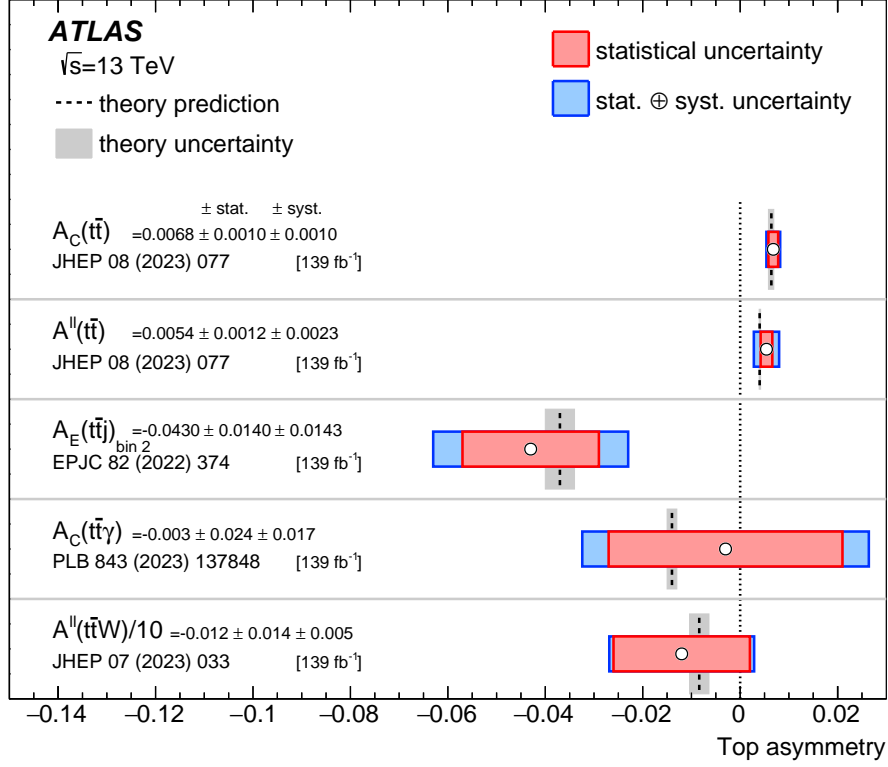


Figure 13: Summary of the $\sqrt{s} = 13$ TeV top asymmetry measurements using the full Run 2 dataset: $\bar{t}t$ asymmetry, lepton-based asymmetry, energy asymmetry in the bin with the largest expected asymmetry, and asymmetry in $\bar{t}t\gamma$ and $\bar{t}tW$ events. Each of the results is compared with their corresponding theoretical expectation. The value of the $\bar{t}t$ asymmetry in $\bar{t}tW$ events is shown divided by 10 for display purposes.

In $\bar{t}t$ production where only one of the top quarks decays leptonically, there are four quarks as decay products. The two quarks from the decay of the W boson, which is a colour-neutral object, are expected to be colour-connected. The two b -quarks from the top-quark decays carry the colour of their parent top quarks but are not expected to share any colour connection. These features can be tested experimentally. Building on the $\sqrt{s} = 8$ TeV analysis [231], ATLAS performed a measurement of colour flow using 36 fb $^{-1}$ of $\sqrt{s} = 13$ TeV data [232]. The observable used to encode the colour information was the so-called jet-pull vector $\vec{\mathcal{P}}$ [233]. It is defined as the sum of the transverse momenta of the jet constituents i weighted by their distance from the jet axis, $\Delta\vec{r}_i = (\Delta y_i, \Delta\phi_i)$, in the y - ϕ space and normalised by the jet p_T : $\vec{\mathcal{P}} = (1/p_T) \sum_i |\Delta\vec{r}_i| p_T^i \Delta\vec{r}_i$. With two jets j_1 and j_2 in the y - ϕ space, one can construct the jet-pull angle $\theta_{\mathcal{P}}$ between the jet-pull vector $\vec{\mathcal{P}}(j_1)$ and the vector connecting j_1 and j_2 . If the two jets j_1 and j_2 are colour-connected, a bias toward $\theta_{\mathcal{P}} \sim 0$ is expected, whereas if they are not connected, the distribution of the jet-pull angle is expected to be uniform. Applied to $\bar{t}t$ events, three of the four observables measured are the jet-pull angles, $\theta_{\mathcal{P}}(j_1^W, j_2^W)$ and $\theta_{\mathcal{P}}(j_2^W, j_1^W)$, of the jets from the W -boson decays, j_1^W and j_2^W , taken to be the two leading non- b -tagged jets, and the magnitude of the pull-vector from j_1^W . These are expected to show colour connections. The jet-pull angle of the two leading b -tagged jets was also measured but is not expected to show colour connection. In this analysis, the jet-pull vectors were calculated only from tracks in the inner detector. All four reconstructed observables were unfolded to particle level using the IBU method and normalised, so as to study only their shape and mitigate the impact of systematic uncertainties.

The results were compared with several generator predictions that differ in their hadronisation modelling (the string model for PYTHIA and the cluster model for HERWIG). Agreement with the HERWIG modelling was found to be better. The unfolded distributions are also used to test the prediction of an exotic model that implements flipped colour flow. The data disfavours this model, with p -values of at most 0.002 for all the tested variables. These unfolded data can be used to tune MC generators to better model the effects of colour connections between partons.

The top-quark sector is also useful for tuning colour models that can not be derived from QCD first principles. In MC generators, the colour information is traced using the leading-colour approximation [234, 235], where each quark is connected to only one other parton, while each gluon, which carries a colour and an anticolour, is connected to two other partons. The multiple parton interactions overlaid on the hard-scattering process add additional colour lines, which could potentially lead to phase-space overlaps. The colour-reconnection models [64] reassign colour connections between partons in order to resolve these overlapping colour lines. There are several mechanisms that could be introduced and that should be tuned to data. The exact involvement of the top quark and its decay products in these processes is not known. The current models involved only the top quark itself in the colour-reconnection mechanisms, and not its decay products, so it was important to test these models on data. With 139 fb^{-1} of $\sqrt{s} = 13 \text{ TeV}$ data, ATLAS used $t\bar{t}$ events in the channel with one electron and one muon, and two or three jets (including exactly two b -tagged jets) to measure distributions sensitive to colour reconnection [236]. The chosen observables were the charged-particle multiplicity outside the jets (excluding leptons from the top-quark decays), the scalar sum of the transverse momenta of these charged particles, and the double-differential cross-section in these two quantities. These observables need to be corrected for tracks from pile-up and from secondary vertices, and for tracking inefficiencies. The corrected observables were unfolded to particle level using the IBU method to obtain normalised differential cross-sections. The measurements have a precision of 2%–10% in the central bins and up to 50% in the outer bins. Agreement between the measured differential cross-sections and various models implemented in MC generators was assessed by means of a χ^2 test. The HERWIG generator describes the data well for the observable built with the p_T scalar sum, while the prediction from PYTHIA is better for the charge-particle multiplicity. The results were also compared with predictions from different models of multiple parton interactions, since the chosen observables are also sensitive to these. The results could be used for future tuning of the MC parameters for both colour reconnection and multiple parton interactions, which should be performed simultaneously.

As discussed in Sections 2.2 and 3.2, hadronically decaying top quarks with sufficiently high transverse momentum can be reconstructed as single large-radius jets. These boosted top-quark jets are characterised by their distinctive substructure, which is often used to separate them from energetic jets arising from lighter quarks or gluons [237–239]. It is therefore important to test the modelling of these features in MC simulation, through a comparison with observed data. Moreover, deviations of top-quark-jet substructure from the SM predictions could also serve as tests of BSM effects that may not be detectable with inclusive cross-section measurements. ATLAS measured substructure properties of jets emerging from hadronically decaying boosted top quarks, using the full Run 2 dataset, in $t\bar{t}$ events in both the semileptonic and all-hadronic channels [240]. Top-quark jets were reconstructed either in the all-hadronic channel as large- R jets, using calorimeter energy deposits as input, or in the semileptonic channel as large- R reclustered jets, using small- R particle-flow jets as input. In both cases, the anti- k_r clustering algorithm with $R = 1$ was used, and top-quark candidate jets were required to have $p_T > 350 \text{ GeV}$. In the all-hadronic channel, in order to discriminate between $t\bar{t}$ events and QCD multijet background events, two large- R jets were selected, with one required to be tagged by a top-quark-tagging algorithm [237] using several substructure variables as input, and a second one without this requirement, to avoid biasing the measured observables. Differential cross-sections were measured as a function of eight substructure variables, defined using

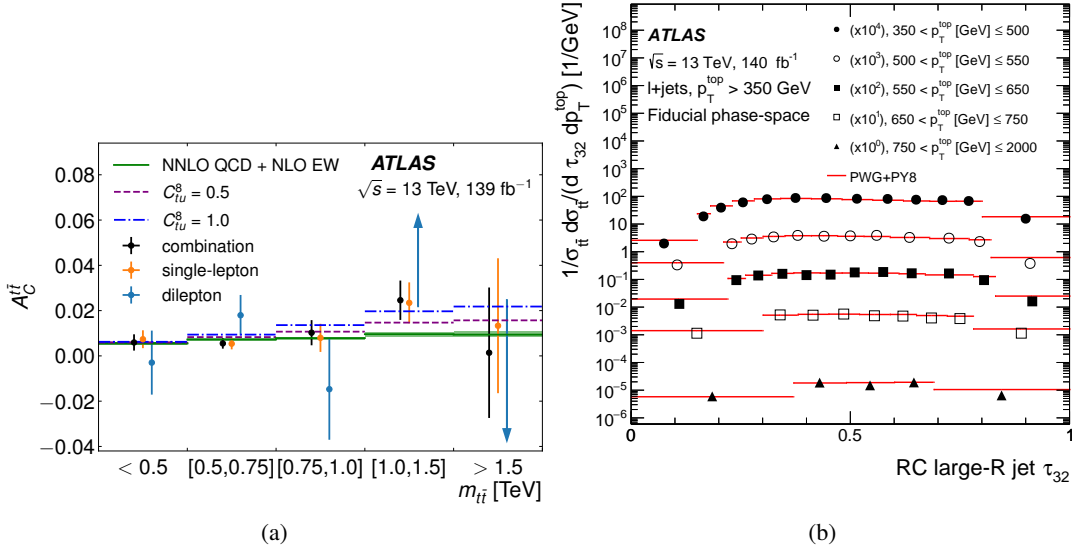


Figure 14: (a) Unfolded differential charge asymmetry $A_C^{t\bar{t}}$ as a function of the invariant mass of the reconstructed top-quark pair [219]. (b) Particle-level differential $t\bar{t}$ production cross-section as a function of τ_{32} for several intervals of top-quark transverse momentum, comparing data measurements with predictions [240].

only the charged components of the jets (see Figure 14 (b)). Double-differential distributions were also measured, with two of these substructure variables (namely τ_{32} and D_2) measured in bins of top-quark-jet p_T and mass. Results unfolded to particle level were compared with a number of MC predictions. The nominal prediction from POWHEG+PYTHIA 8 was found to properly model measurements of the broadness and the two-body structure, but to poorly model variables sensitive to the three-body structure of the top-quark jets, with the predicted jet substructure being more three-body-like than observed. On the other hand, alternative predictions, such as those from AMC@NLO+PYTHIA 8 and POWHEG+HERWIG 7, as well as those from POWHEG+HERWIG 8 with less FSR, were found to better model some of these distributions. Overall, the measurement indicates the need to improve the models used to predict the substructure of boosted top-quark jets.

7.4 Test of lepton-flavour universality

Top-quark production and decay can also be used as a tool to study generic properties of the SM, taking advantage of the large $t\bar{t}$ sample available at $\sqrt{s} = 13$ TeV to perform precise measurements. One interesting example is a test of lepton-flavour universality in top-quark decays. Lepton-flavour universality is the SM axiom stating that the couplings of the electroweak gauge bosons to the three charged leptons are equal. A large and unbiased sample of W bosons can be selected in $t\bar{t}$ events and used to test this axiom by measuring the ratio of W -boson decay rates into different charged leptons, $\ell, \ell' = e, \mu, \tau$: $R_W(\ell/\ell') = B(W \rightarrow \ell\nu_\ell)/B(W \rightarrow \ell'\nu_{\ell'})$.

The ratio $R_W(\mu/\tau)$ is particularly relevant because a measurement in $e^+e^- \rightarrow W^+W^-$ events at LEP found a deviation from unity: $R_W(\tau/\mu) = 1.070 \pm 0.026$ [241]. ATLAS measured this ratio by analysing the full Run 2 dataset, identifying the τ -leptons through their decay into muons [242]. Hence the key step in the analysis is to distinguish these muons from those coming directly from W -boson decay (prompt muons).

This was achieved by using the distinct features of the τ -lepton: its significant lifetime, giving rise to a track with a large impact parameter, and its multibody decay into a muon and two neutrinos, leading to an average muon transverse momentum that is lower than in direct $W \rightarrow \mu\nu$ decays. The measurement was performed in both the $e\mu$ channel and the $\mu\mu$ channel, with one lepton used to probe the W -boson branching ratio and the other lepton to trigger the event and ensure a high-purity selection of top-pair events. The fraction of muons that are prompt ($W \rightarrow \mu\nu_\mu$) and the fraction that come from non-prompt τ -lepton decay ($W \rightarrow \tau\nu_\tau \rightarrow \mu\nu_\mu\nu_\tau$) were determined from a fit using templates that exploit shape differences between those fractions' distributions of both the muon's transverse impact parameter $|d_0|$ (i.e. the distance of closest approach of the muon track to the beam line in the x - y plane) and the muon's transverse momentum p_T . The $|d_0|$ shape for the prompt muons was calibrated using $Z \rightarrow \mu\mu$ events. The normalisations of the main backgrounds, i.e. prompt muons coming from $Z \rightarrow \mu\mu$ decays and non-prompt muons coming from b - or c -hadron decays, were extracted using control regions. The ratio $R_W(\tau/\mu)$ was measured from a two-dimensional profile-likelihood fit of the muon $|d_0|$ and p_T distributions, where the overall $t\bar{t}$ normalisation was allowed to vary freely, leading to $R_W(\tau/\mu) = 0.992 \pm 0.007(\text{stat.}) \pm 0.011(\text{syst.})$. The result agrees with the SM expectation of lepton-flavour universality and constitutes the most precise determination of this ratio. It demonstrates the ability of the LHC experiments to perform high-precision measurements.

Moreover, the large $t\bar{t}$ event sample collected during Run 2 was used to precisely measure the ratio of W -boson decay rates into electrons and muons [243]. The analysis selected $t\bar{t}$ events in the ee , $\mu\mu$ and $e\mu$ dilepton final states, relating the relative difference between channels to the ratio $R_W(\mu/e)$, and extracting the ratio by means of a maximum-likelihood fit. The measurements in the three channels were obtained with a technique similar to that used for the inclusive $t\bar{t}$ cross-section measurement in the $e\mu$ channel (see Section 3.1), with the dilepton invariant mass $m_{\ell\ell}$ being exploited in the ee and $\mu\mu$ channels to separate signal events from the dominant Z +jets background. In order to reduce the sensitivity to uncertainties in the electron and muon identification efficiencies, the result was normalised to the square root of the ratio of Z -boson decay rates to electron and muon pairs, $R_Z(\mu\mu/ee)$, which was measured simultaneously in data. The precise value of $R_Z(\mu\mu/ee)$ from the LEP and SLD experiments (with a $\sim 0.3\%$ uncertainty [193, 244]) was then used to extract the final result: $R_W(\mu/e) = 0.9995 \pm 0.0022(\text{stat.}) \pm 0.0036(\text{syst.}) \pm 0.0014(\text{ext.})$, where the last uncertainty refers to the external measurement of $R_Z(\mu\mu/ee)$. The SM assumption of lepton-flavour universality in W -boson decays into electron–neutrino and muon–neutrino pairs was thus confirmed at the 0.5% level.

8 Search for flavour-changing neutral currents in the top-quark sector

In the SM, flavour-changing neutral-current (FCNC) processes are forbidden at tree level and are strongly suppressed in loops by the GIM mechanism [245]. In the top-quark sector, the rare decay channels in which the top quark decays into a neutral boson (a Higgs or Z boson, a photon or a gluon) and a c - or u -quark belong to this family and are predicted to have branching ratios (BRs) ranging from 10^{-12} to 10^{-17} [246]. In addition, the same interaction vertices can give rise to single-top FCNC production processes, where a top quark (or antiquark) is produced in association with a neutral boson. These processes are predicted to have negligible cross-sections in the SM, but a number of BSM scenarios predict enhancements, increasing the FCNC top-quark decay BRs to 10^{-4} in some cases. These SM extensions include the quark-singlet model [247], the two-Higgs-doublet model [248], the Minimal Supersymmetric Standard Model (MSSM) [249], the MSSM with R-parity violation [250], models with warped extra dimensions [251], and extended mirror-fermion models [252].

During LHC Run 2, ATLAS investigated essentially all the accessible channels for such FCNC searches. Signal processes with a Higgs boson in the final state, i.e. involving the tHq vertex with $q = c$ or u , were the most intensely studied. This kind of process gives rise to a number of possible final-state topologies, depending on the Higgs boson’s decay mode, each requiring a dedicated analysis strategy and optimisation. On the other hand, these analyses could benefit from the experience gained through the studies of the Higgs boson production and decay modes, particularly in the context of $t\bar{t}H$ production. In addition, searches for processes involving neutral gauge bosons, i.e. with a tgq , $t\gamma q$ or tZq vertex, were performed. Both FCNC top-quark decays and single-top FCNC production processes were investigated, by eventually adopting a global approach as suggested in Ref. [253], relating FCNC decay branching ratios to FCNC production cross-sections via EFT operators.

8.1 Searches for top-quark FCNC processes involving a Higgs boson

The first published Run 2 searches for FCNC top-quark decays into a c - or u -quark and a Higgs boson, separately focusing on the $H \rightarrow \gamma\gamma$ [254], $H \rightarrow W^+W^-$ [255] and $H \rightarrow b\bar{b}/\tau^+\tau^-$ [256] decay channels, were all based on the dataset collected in 2015 and 2016, corresponding to an integrated luminosity of 36 fb^{-1} . All three analyses looked for $t\bar{t}$ events where one of the two top quarks decays into bW and the other via a FCNC into cH or uH . With the larger dataset available at the end of Run 2, updated results were released for most of these main Higgs boson decay channels. These new analyses considered FCNC processes not only in the top quark’s decay but also in its production, by searching for events with a single top quark plus a Higgs boson (tH) that were initiated by a u - or c -quark. The results were reported in dedicated papers for the $H \rightarrow \gamma\gamma$ [257], $H \rightarrow W^+W^-$ [258] and $H \rightarrow \tau^+\tau^-$ [259] channels, while for Higgs boson decay into a pair of bottom quarks, ATLAS took advantage of the full Run 2 dataset to perform a more general search for FCNC top-quark decays into a generic scalar boson and an up-type quark [260], in a new-scalar-boson mass range from 20 to 160 GeV, thus including the SM Higgs boson.

Searches using the Higgs boson’s diphoton decay channel [254, 257] looked for final states with a pair of energetic isolated photons with an invariant mass peaking at the Higgs boson mass, a top quark (decaying either leptonically or hadronically), and possibly a hadronic jet from a light quark or c -quark. In the partial-dataset analysis, events were separated into categories depending on the presence of a charged lepton and on the compatibility of the reconstructed final states with $t\bar{t}$ decays. With the full dataset, the analysis was further improved by using a dedicated charm-tagging algorithm to split the event categories more finely, and using a BDT-based selection for their definition. The result was then extracted by fitting the diphoton invariant-mass spectra with a resonant signal function centred around the Higgs boson mass and a background function, with constraints mainly from $m_{\gamma\gamma}$ bands on either side of each signal region.

The analyses reported in Ref. [255] and Ref. [258] focused on multilepton final states, targeting Higgs boson decays giving rise to at least one electron or muon, such as $H \rightarrow WW$ with at least one of the two W bosons decaying leptonically, but also $H \rightarrow ZZ$ or $H \rightarrow \tau\tau$.⁶ When the SM leg of the top-quark or top-antiquark decay gives rise to a charged lepton as well, these processes can produce events with two same-sign electrons or muons, or even three-lepton events, for which the background from SM processes is significantly smaller. This analysis is characterised by final states similar to those for the $t\bar{t}H$ measurement in the multilepton channel [261] and therefore shares with it a good fraction of the event selection, event

⁶ The analysis vetoes events with at least one reconstructed hadronic τ -lepton decay, so as to avoid statistical overlap with the dedicated search described before. Therefore, the analysis is sensitive to $H \rightarrow \tau\tau$ only when both τ -leptons decay to an electron or muon.

categorisation and background estimation. However, dedicated multivariate discriminants were employed in the signal regions to separate the SM processes from the FCNC signal.

The $H \rightarrow \tau^+ \tau^-$ analyses [256, 259] categorised events according to the numbers of reconstructed hadronic τ -lepton decays (τ_{had}) and light charged leptons from leptonic τ -lepton decays (τ_{lep}), to separately target $\tau_{\text{had}} \tau_{\text{had}}$ and $\tau_{\text{lep}} \tau_{\text{had}}$ events.⁷ While the partial-dataset analysis focused on hadronic decay in the SM leg of the $t\bar{t}$ process, the full-dataset analysis also included single-top topologies and dedicated event categories targeting $t\bar{t}$ events with leptonic top-quark decay. Events in the various categories were processed through dedicated kinematic reconstruction algorithms, aiming to deduce the four-momenta of the invisible decay products for each τ -lepton decay. Finally, dedicated BDT discriminants were built in each category, separately for the tcH and tuH couplings, using as input a number of topological and kinematic final-state variables, including ones with values coming from the kinematic reconstruction.

The $H \rightarrow b\bar{b}$ analyses [256, 260] were also heavily based on studies and analysis techniques developed in the context of the searches for the $t\bar{t}H$ process, in this case in the $b\bar{b}$ decay channel during Run 1 [262] and Run 2 [263]. They relied on the presence of a high-momentum electron or muon in the SM leg of the $t\bar{t}$ decay and categorised selected events according to jet and b -tagged-jet multiplicities (4–6 jets, and 2–4 b -tagged jets), with the goal of retaining events with b -quark jets that fail the b -tagging requirements, c -quark jets that are b -tagged, jets that are outside the acceptance or produced from hard QCD radiation, as well as including background-enriched data samples, useful for placing in situ constraints on some of the associated systematic uncertainties. In the first analysis, a dedicated likelihood discriminant was constructed in each of the categories to assess the compatibility of the observed final states with signal processes by considering invariant masses of jet and lepton combinations. The second analysis implemented a discriminating variable based on a NN in each signal region for each scalar mass hypothesis.

None of these searches for FCNC top-quark decays observed any significant excess over the SM expectations, with the largest deviation from the background-only hypothesis found in the case of the full-dataset analysis in the $\tau\tau$ channel, yielding a 2.3σ significance. Exclusion limits were then set on the branching ratios for the $t \rightarrow Hc$ and $t \rightarrow Hu$ processes, from each of the individual channels as well as from their combinations, and reported in Ref. [256] and Ref. [258] for the searches based on 36 fb^{-1} and 140 fb^{-1} respectively. For the partial-dataset analyses, the exclusion upper limits at 95% CL ranged from 1.5×10^{-3} to 5×10^{-3} depending on the channel, with combined limits of around 1×10^{-3} for both up-type-quark flavours. The corresponding 95% CL exclusion limits obtained by combining the full-dataset analyses instead yielded:

$$B(t \rightarrow uH) < 2.6 \times 10^{-4} \text{ and } B(t \rightarrow cH) < 3.4 \times 10^{-4}.$$

These results are shown in Figure 15, together with those of the individual input analyses.

8.2 Searches for top-quark FCNC processes involving neutral gauge bosons

With the full Run 2 dataset, ATLAS also performed searches for top-quark FCNC couplings to the gluon, the photon and the Z boson. In particular, limits on the top-quark FCNC interactions involving a gluon were set by searching for the single-top-quark production processes $ug \rightarrow t$ and $cg \rightarrow t$ [264]. This analysis relied on the selection of a sample of events compatible with the production of a single top quark, without the accompanying jet characterising the SM single-top-quark production channels (the t -, s - and tW -channels, see Section 4). The event selection was defined by requiring the presence of an electron or

⁷ Higgs boson decays with two τ_{lep} were targeted by the multilepton search.

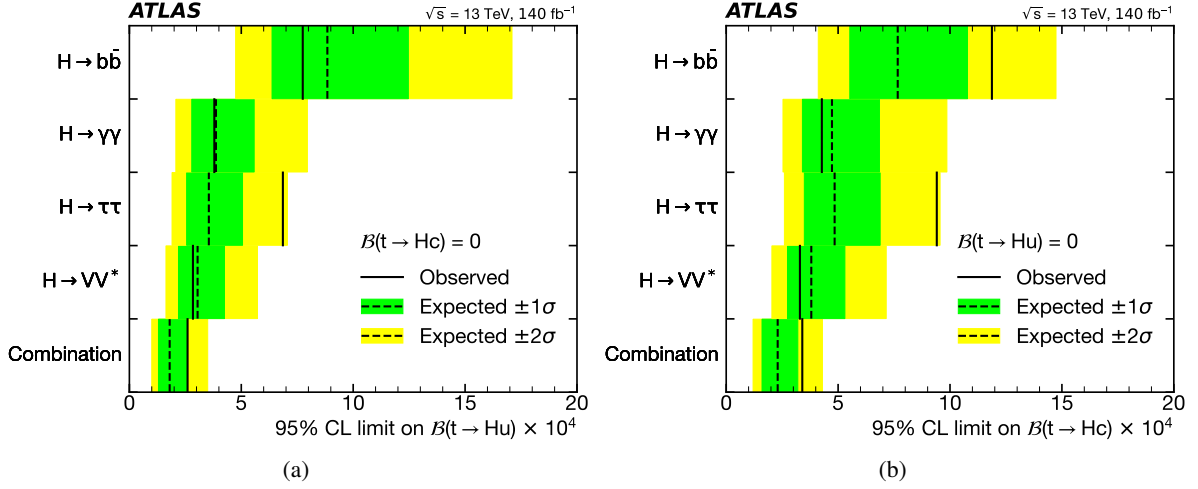


Figure 15: 95% CL upper limits on (a) $B(t \rightarrow Hu)$ and (b) $B(t \rightarrow Hc)$ for the individual ATLAS searches based on the full Run 2 dataset, as well as their combination (assuming (a) $B(t \rightarrow Hc) = 0$ and (b) $B(t \rightarrow Hu) = 0$). The observed limits (solid lines) are compared with the expected (median) limits under the background-only hypothesis (dotted lines). The surrounding shaded bands correspond to the 68% and 95% CL intervals around the expected limits, denoted by $\pm 1\sigma$ and $\pm 2\sigma$, respectively. Figures taken from Ref. [258].

muon, large missing transverse momentum, and exactly one central jet passing a particularly tight b -tagging requirement corresponding to a nominal 30% efficiency for b -quark-initiated jets and a rejection rate of around 900 (30 000) for c -quark-initiated (light-quark-initiated) jets. Two NN discriminants were built to discriminate between signal events and background events, including the irreducible background from t -channel single-top-quark production, based on a number of kinematic properties of final-state leptons, jets and the missing transverse momentum. One of these discriminants was trained specifically to isolate FCNC top-quark-production events initiated by a valence quark and a gluon, namely $ug \rightarrow t$, characterised by kinematic properties different from those of events from sea-quark-initiated processes such as $\bar{u}g \rightarrow \bar{t}$, $cg \rightarrow t$ and $\bar{c}g \rightarrow \bar{t}$. No significant excess of events compatible with FCNC-production kinematics was observed, and exclusion limits were set on the production cross-sections of the two signal processes. These were then turned into 95% CL limits on top-quark FCNC-decay branching ratios:

$$B(t \rightarrow ug) < 0.61 \times 10^{-4} \text{ and } B(t \rightarrow cg) < 3.7 \times 10^{-4}.$$

Limits on the c -quark-initiated process are significantly weaker than those on the u -quark-initiated process. This is mainly due to the predicted cross-section being lower for the $cg \rightarrow t$ process because it can only be initiated by sea quarks, which typically have a lower momentum fraction than the valence quarks contributing to the $ug \rightarrow t$ process. However, c -quark-initiated processes are still phenomenologically relevant, especially for two-Higgs-doublet models, which predict stronger FCNC couplings between top and charm quarks.

FCNC coupling between a top quark and a photon was also investigated deeply using Run 2 data. A search for FCNCs in the production of a top quark with a photon, $gu \rightarrow t\gamma$ or $gc \rightarrow t\gamma$, was performed using 80 fb^{-1} of data [265]. Events with an energetic isolated photon and the typical final-state signature of a leptonically decaying top quark (an isolated electron or muon, a b -tagged jet and missing transverse momentum), and possibly additional jets, were selected, and a NN based on kinematic variables was

used to discriminate between signal and SM background processes. The analysis was updated to use the full Run 2 dataset [266], and extended to cover both the production and decay processes, $gq \rightarrow t\gamma$ and $t \rightarrow \gamma q$ (in $t\bar{t}$ events) with q being an u - or c -quark, as target signal. As done in previous analyses, the search for a FCNC in top-quark decay was limited to $t\bar{t}$ -production events, so the two signal processes were characterized by similar event topologies. A multi-class DNN discriminant was built to classify events as coming from one of the two signal processes (FCNC in production or FCNC in decay) or as background events. Dedicated control samples were selected in order to control the normalisation of the main background processes, $t\bar{t}\gamma$ and $W\gamma$, while data-driven scale factors were obtained to correct the simulation of the background component induced by the misidentification of a hadron or an electron as a photon. The DNN was trained separately for $t\gamma u$ and $t\gamma c$ couplings, because of the different kinematics for the $gu \rightarrow t\gamma$ and $gc \rightarrow t\gamma$ processes, induced by the differences between the up- and charm-quark PDFs, and the different b -tagging probabilities for $t\bar{t}$ events with a $t \rightarrow \gamma u$ decay or $t \rightarrow \gamma c$ decay. The final results of the two searches, extracted with a binned profile-likelihood fit to the DNN discriminant in the signal region and to the photon p_T distributions in the background control regions, didn't show any significant excess over the SM expectations, allowing exclusion limits to be set on the signal production cross-sections and decay branching ratios, separately for right-handed (RH) and left-handed (LH) $t\gamma q$ couplings, as well as on the relative effective coupling constants [130, 253, 267, 268]. The exclusion limits on the branching ratios range from 2.8×10^{-5} to 22×10^{-5} for the former analysis, and from 0.85×10^{-5} to 4.5×10^{-5} for the latter analysis, depending on the light quark's flavour and on the coupling chirality, with the full-Run 2 results improving on the previous limits by factors of 3.3 to 5.4. For a LH $t\gamma q$ coupling, the 95% CL exclusion limits obtained are:

$$B(t \rightarrow uZ) < 0.85 \times 10^{-5} \text{ and } B(t \rightarrow cZ) < 4.2 \times 10^{-5}.$$

Finally, FCNC coupling between a top quark and a Z boson was studied in Ref. [269] and Ref. [270]. The former analysis, based on 36 fb^{-1} , relied only on the top-quark-pair events, with one top quark decaying through the $t \rightarrow Zq$ channel, while the latter analysis, based on the full Run 2 dataset, included single-top-quark production via $gq \rightarrow tZ$ (with $q = u, c$) as a signal process. Since the final-state topologies are similar to those investigated in SM $t\bar{t}Z$ and tZ associated-production processes (see Section 5), the analysis naturally relied on the selection of events with three charged leptons, two of them coming from the Z -boson decay and the other from the top-quark decay, plus a b -tagged jet and possibly additional jets. In the first analysis, the top quarks were kinematically reconstructed from the final-state leptons and jets, using χ^2 minimisation across all the possible jet and lepton permutations in each event. The result of the χ^2 minimisation was used as a discriminating variable in the three-lepton signal region, and a number of control regions were included in the analysis to specifically target the $t\bar{t}Z$, WZ , ZZ and non-prompt-lepton backgrounds. For the full-Run 2 search, multivariate discriminants were introduced to improve the signal sensitivity beyond the gain from the larger analysed dataset. In particular, after separating selected events into two orthogonal signal regions, individually optimised for single-top-quark and $t\bar{t}$ production signal processes, gradient boosted decision trees (GBDTs) were trained to discriminate between FCNC signals and SM backgrounds, using the outputs of the kinematic reconstruction as input variables. In the signal region dedicated to single-top-quark production, two separate GBDTs were built to separately target u - and c -quark-initiated processes. Finally, the presence of signal events from RH and LH FCNC couplings was tested separately. The full-Run 2 analysis improved the sensitivity to the branching ratios $B(t \rightarrow Zq)$ by a factor of two, and set the following 95% CL exclusion limits for the LH coupling scenario:

$$B(t \rightarrow u\gamma) < 6.2 \times 10^{-5} \text{ and } B(t \rightarrow c\gamma) < 1.3 \times 10^{-4}.$$

Similar limits were set for the RH coupling hypothesis (6.6×10^{-5} and 1.2×10^{-4} for the tZu and tZc couplings, respectively).

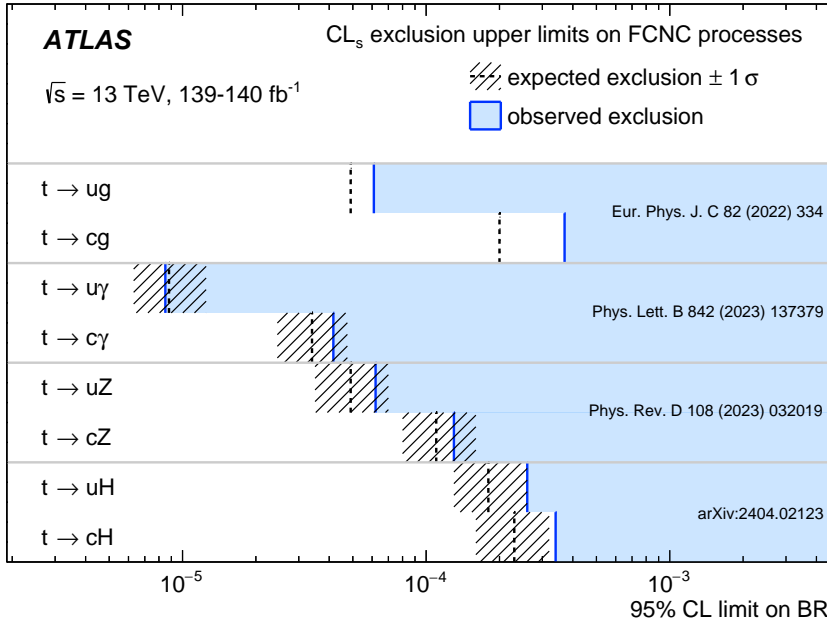


Figure 16: Summary of the 95% CL observed and expected limits on the branching ratios of the top-quark decays via flavour-changing neutral currents (FCNC) to a quark and a neutral boson $t \rightarrow qX$ ($X = g, Z, \gamma$ or H ; $q = u$ or c) set by the ATLAS Collaboration using its full Run 2 dataset. The hatched area represents the $\pm 1\sigma$ band around the expected exclusion limit. It is not shown in the case of the tgq coupling, as the numbers are not quoted in the publication. The quoted upper limits refer to the left-handed chirality hypothesis, and expected limits are computed assuming zero Standard Model contribution to the FCNC processes.

8.3 Summary of FCNC process constraints

A summary of the exclusion limits set by the ATLAS Run 2 searches for FCNCs in the top-quark sector is shown in Figure 16. As can be seen, exclusion limits on photon-mediated FCNC processes are the strongest, followed by those on transitions mediated by Z bosons and gluons, while weaker limits are set on processes involving Higgs bosons. In all cases, the sensitivity is stronger for $t \rightarrow u$ than for $t \rightarrow c$ transitions. All of these stringent limits on top-quark FCNC interactions were also interpreted as constraints on Wilson coefficients in an EFT framework, as detailed in Section 9.

9 Limits on Wilson coefficients within effective field theory

New physics effects from BSM theories characterised by a mass scale higher than the energy accessible at the LHC can be investigated in the framework of the Standard Model effective field theory (SMEFT), without specifying a particular BSM model. The SMEFT extension of the SM Lagrangian is:

$$\mathcal{L}_{\text{SMEFT}} = \mathcal{L}_{\text{SM}} + \sum_i \frac{C_i}{\Lambda^2} O_i + \dots$$

where \mathcal{L}_{SM} represents the SM Lagrangian, O_i are effective dimension-six operators and C_i the corresponding Wilson coefficients. Here, Λ corresponds to the cut-off scale of the effective theory and is usually set to

$\Lambda = 1$ TeV. Dimension-five operators induce baryon- and lepton-number-violating terms and are therefore usually ignored. Higher-dimension operators are Λ -suppressed and usually also ignored. The operators can be expressed in different bases. The Warsaw basis [267] is chosen for the results presented here.

Strong $t\bar{t}$ production is sensitive to the operator O_{tG} , which modifies the top–gluon vertex and primarily changes the overall production rate, and to the 14 operators characterising four-quark interactions: $O_{tu}^{(1)}$, $O_{tu}^{(8)}$, $O_{td}^{(1)}$, $O_{td}^{(8)}$, $O_{tq}^{(1)}$, $O_{tq}^{(8)}$, $O_{Qu}^{(1)}$, $O_{Qu}^{(8)}$, $O_{Qd}^{(1)}$, $O_{Qd}^{(8)}$, $O_{Qq}^{(1,1)}$, $O_{Qq}^{(3,1)}$, $O_{Qq}^{(1,8)}$, $O_{Qq}^{(3,8)}$. In particular, $O_{tq}^{(8)}$ can significantly alter differential $t\bar{t}$ cross-sections in the high-energy tails. The t -channel single-top-quark cross-section is particularly sensitive to the operator $O_{Qq}^{3,1}$. The Wtb vertex could also be altered by the operators $O_{\phi Q}^3$ and O_{tW} . The $t\bar{t}Z$ cross-section is sensitive to the 14 four-quark operators as well as to the operators modifying the top–boson vertices (O_{tW} , O_{tB} , O_{tG} , $O_{HQ}^{(1)}$, $O_{HQ}^{(3)}$, O_{Ht}). The $t\bar{t}t\bar{t}$ cross-section is specifically sensitive to the four heavy-flavour fermion operators (O_{QQ}^1 , O_{Qt}^1 , O_{tt}^1 , O_{Qt}^8). The $t\bar{t}$ charge asymmetry $A_C^{t\bar{t}}$ is also sensitive to the 14 four-quark operators but to different linear combinations of these, compared to $t\bar{t}$ production, which helps to disentangle the contributions when global fits are performed. It is also sensitive to the top–gluon operator O_{tG} . The differential $A_C^{t\bar{t}}$ measurements lead to tighter limits than obtained from the inclusive $A_C^{t\bar{t}}$ measurement, so the differential constraints are reported here. The energy asymmetry $A_E(\theta_j)$ is particularly sensitive to the chirality and the colour charges of the involved quark fields, and therefore to six specific four-quark operators ($O_{tu}^{(1)}$, $O_{tu}^{(8)}$, $O_{tq}^{(1)}$, $O_{tq}^{(8)}$, $O_{Qq}^{(1,1)}$, $O_{Qq}^{(1,8)}$).

Finally, limits on top-quark FCNC couplings can be interpreted as constraints on the Wilson coefficients of the EFT operators inducing tree-level FCNC transitions [253]. Exclusion limits on top–Higgs FCNC couplings can be translated into constraints on the coefficients $C_{u\phi}^{13}$ and $C_{u\phi}^{23}$, those on the top–gluon coupling into constraints on C_{uG}^{13} and C_{uG}^{23} , while limits on both photon- and Z -boson-induced FCNC interactions translate into constraints on linear combinations of the coefficients C_{uB}^{i3} and C_{uW}^{i3} , with $i = 1, 2$.

The 95% CL limits on Wilson coefficients extracted for $\Lambda = 1$ TeV from the measurements and searches described in this paper, assuming one coefficient at a time to be non-zero, are summarised in Tables 1, 2 and 3. These bounds are obtained using a parameterisation that includes the dimension-six-squared terms.

Table 1: Summary of the 95% CL intervals for top–boson Wilson coefficients within SMEFT set by the top-quark Run 2 measurements and searches. These limits are set for $\Lambda = 1$ TeV and when one coefficient at a time is assumed to be non-zero. $\Re C_{tW}$ and $\Im C_{tW}$ represent the real and imaginary parts of the complex C_{tW} coefficient.

| Top–boson coefficient | Limits | Input measurement | Reference |
|-----------------------|---------------|-----------------------------|-----------|
| $C_{\phi Q}^3$ | [−0.87, 1.42] | t -channel cross-section | [109] |
| $\Re C_{tW}$ | [−0.9, 1.4] | t -channel polarisation | [110] |
| | [−0.84, 1.0] | $t\bar{t}Z$ cross-section | [147] |
| $\Im C_{tW}$ | [−0.8, 0.2] | t -channel polarisation | [110] |
| | [−1.0, 1.0] | $t\bar{t}Z$ cross-section | [147] |
| $C_{HQ}^{(1)}$ | [−1.4, 0.84] | $t\bar{t}Z$ cross-section | [147] |
| $C_{HQ}^{(3)}$ | [−0.95, 2.0] | $t\bar{t}Z$ cross-section | [147] |
| C_{Ht} | [−2.2, 1.6] | $t\bar{t}Z$ cross-section | [147] |
| $\Re C_{tB}$ | [−1.7, 1.6] | $t\bar{t}Z$ cross-section | [147] |
| $\Im C_{tB}$ | [−1.9, 1.9] | $t\bar{t}Z$ cross-section | [147] |
| $\Re C_{tG}$ | [−0.23, 0.34] | $t\bar{t}Z$ cross-section | [147] |
| | [−0.75, 0.14] | $t\bar{t}$ charge asymmetry | [219] |
| | [−0.52, 0.15] | $t\bar{t}$ cross-section | [97] |
| $\Im C_{tG}$ | [−0.32, 0.33] | $t\bar{t}Z$ cross-section | [147] |

Table 2: Summary of the 95% CL intervals for four-quark Wilson coefficients within SMEFT set by the top-quark Run 2 measurements and searches. These limits are set for $\Lambda = 1$ TeV and when one coefficient at a time is assumed to be non-zero.

| Four-quark coefficient | Limits | Input measurement | Reference |
|------------------------|---------------|----------------------------------|-----------|
| $C_{Qq}^{3,1}$ | [−0.37, 0.06] | t -channel cross-section | [109] |
| | [−0.34, 0.23] | $t\bar{t}Z$ cross-section | [147] |
| | [−0.34, 0.43] | $t\bar{t}$ charge asymmetry | [219] |
| $C_{Qd}^{(1)}$ | [−0.47, 0.46] | $t\bar{t}Z$ cross-section | [147] |
| | [−0.39, 0.42] | $t\bar{t}$ charge asymmetry | [219] |
| $C_{Qd}^{(8)}$ | [−1.8, 0.62] | $t\bar{t}Z$ cross-section | [147] |
| | [−0.96, 1.37] | $t\bar{t}$ charge asymmetry | [219] |
| $C_{Qq}^{(1,1)}$ | [−0.29, 0.29] | $t\bar{t}Z$ cross-section | [147] |
| | [−0.52, 0.28] | $t\bar{t}$ charge asymmetry | [219] |
| | [−0.65, 0.67] | $t\bar{t}$ energy asymmetry | [223] |
| $C_{Qq}^{(1,8)}$ | [−1.2, 0.080] | $t\bar{t}Z$ cross-section | [147] |
| | [−0.25, 0.53] | $t\bar{t}$ charge asymmetry | [219] |
| | [−1.72, 2.10] | $t\bar{t}$ energy asymmetry | [223] |
| $C_{Qq}^{(3,8)}$ | [−0.68, 0.54] | $t\bar{t}Z$ cross-section | [147] |
| | [−1.23, 0.31] | $t\bar{t}$ charge asymmetry | [219] |
| $C_{Qu}^{(1)}$ | [−0.47, 0.43] | $t\bar{t}Z$ cross-section | [147] |
| | [−0.31, 0.23] | $t\bar{t}$ charge asymmetry | [219] |
| $C_{Qu}^{(8)}$ | [−1.6, 0.36] | $t\bar{t}Z$ cross-section | [147] |
| | [−1.78, 0.27] | $t\bar{t}$ charge asymmetry | [219] |
| $C_{tq}^{(1)}$ | [−0.42, 0.36] | $t\bar{t}Z$ cross-section | [147] |
| | [−0.20, 0.22] | $t\bar{t}$ charge asymmetry | [219] |
| | [−0.69, 0.75] | $t\bar{t}$ energy asymmetry | [223] |
| $C_{tq}^{(8)}$ | [−1.5, 0.22] | $t\bar{t}Z$ cross-section | [147] |
| | [−0.51, 0.58] | $t\bar{t}$ charge asymmetry | [219] |
| | [−2.01, 1.43] | $t\bar{t}$ energy asymmetry | [223] |
| | [−0.64, 0.12] | $t\bar{t}$ cross-section | [97] |
| $C_{td}^{(1)}$ | [−0.56, 0.56] | $t\bar{t}Z$ cross-section | [147] |
| | [−0.60, 0.84] | $t\bar{t}$ charge asymmetry | [219] |
| $C_{td}^{(8)}$ | [−2.5, 1.2] | $t\bar{t}Z$ cross-section | [147] |
| | [−1.62, 1.21] | $t\bar{t}$ charge asymmetry | [219] |
| $C_{tu}^{(1)}$ | [−0.66, 0.64] | $t\bar{t}Z$ cross-section | [147] |
| | [−0.70, 0.31] | $t\bar{t}$ charge asymmetry | [219] |
| | [−0.78, 0.81] | $t\bar{t}$ energy asymmetry | [223] |
| $C_{tu}^{(8)}$ | [−2.2, 0.38] | $t\bar{t}Z$ cross-section | [147] |
| | [−0.45, 0.82] | $t\bar{t}$ charge asymmetry | [219] |
| | [−1.71, 1.56] | $t\bar{t}$ energy asymmetry | [223] |
| C_{QQ}^1 | [−3.5, 4.1] | $t\bar{t}t\bar{t}$ cross-section | [176] |
| C_{Qt}^1 | [−3.5, 3.0] | $t\bar{t}t\bar{t}$ cross-section | [176] |
| C_{tt}^1 | [−1.7, 1.9] | $t\bar{t}t\bar{t}$ cross-section | [176] |
| C_{Qt}^8 | [−6.2, 6.9] | $t\bar{t}t\bar{t}$ cross-section | [176] |

Table 3: Summary of the 95% CL intervals for top-FCNC Wilson coefficients within SMEFT set by the top-quark Run 2 measurements and searches. These limits are set for $\Lambda = 1$ TeV and when one coefficient at a time is assumed to be non-zero.

| FCNC coefficient | Limits | Input search | Reference |
|---------------------------------|-----------|--------------------------|-----------|
| $ C_{u\phi}^{13,31} $ | < 0.68 | $t \rightarrow Hq$ | [258] |
| $ C_{u\phi}^{23,32} $ | < 0.78 | $t \rightarrow Hq$ | [258] |
| $ C_{uG}^{13} $ | < 0.057 | $t \rightarrow gq$ | [264] |
| $ C_{uG}^{23} $ | < 0.14 | $t \rightarrow gq$ | [264] |
| $ C_{uW}^{13*} + C_{uB}^{13*} $ | < 0.103 | $t \rightarrow \gamma q$ | [266] |
| $ C_{uW}^{31} + C_{uB}^{31} $ | < 0.123 | $t \rightarrow \gamma q$ | [266] |
| $ C_{uW}^{23*} + C_{uB}^{23*} $ | < 0.227 | $t \rightarrow \gamma q$ | [266] |
| $ C_{uW}^{32} + C_{uB}^{32} $ | < 0.235 | $t \rightarrow \gamma q$ | [266] |
| $ C_{uW}^{13*} + C_{uB}^{13*} $ | < 0.15 | $t \rightarrow Zq$ | [270] |
| $ C_{uW}^{31} + C_{uB}^{31} $ | < 0.16 | $t \rightarrow Zq$ | [270] |
| $ C_{uW}^{23*} + C_{uB}^{23*} $ | < 0.22 | $t \rightarrow Zq$ | [270] |
| $ C_{uW}^{32} + C_{uB}^{32} $ | < 0.21 | $t \rightarrow Zq$ | [270] |

10 Conclusion

With the unprecedented pp collision dataset collected during LHC Run 2 at a centre-of-mass energy of 13 TeV, the ATLAS Collaboration brought top-quark physics to the next level. Precise measurements challenge the most accurate theoretical predictions. The inclusive $t\bar{t}$ cross-section measurement has reached a precision of 1.8%, exceeding the precision of the NNLO+NNLL prediction. For the most abundant top-quark production processes, as well as for a number of top-quark associated-production processes, the focus is moving toward the measurement of differential distributions. Along with this shift of focus, rarer and rarer production processes can be observed and studied for the first time. Using Run 2 data, the tZq , $tq\gamma$ and $t\bar{t}t\bar{t}$ processes have now been observed. Measurements of the $t\bar{t}Z$, $t\bar{t}W$ and $t\bar{t}\gamma$ cross-sections achieving a precision of around 10% are turning into precision measurements, directly probing the top quark's couplings to gauge bosons. New methods for the precise determination of the top-quark mass have been adopted, alongside those already used in Run 1. Through the identification and reconstruction of top-quark decay products, several interesting measurements have been performed for the first time or with unprecedented accuracy, including the precise determination of the W -boson helicity fractions, the top quark's polarisation and $t\bar{t}$ spin correlations, as well as results showing strong evidence for charge asymmetry in top-quark pair production and the observation of quantum entanglement in $t\bar{t}$ events. Finally, exclusion limits for exotic or anomalous top-quark production and decay mechanisms have been improved significantly, challenging several new physics-model predictions.

In many cases, statistical uncertainties have become subdominant, putting more emphasis on systematic uncertainties. Systematic uncertainties have been reduced markedly with respect to Run 1. Due to precise understanding of detector-related systematic effects, especially those which usually dominate top-quark physics measurements (such as uncertainties in the jet energy scale and b -tagging efficiency), the dominant uncertainty in many of these measurements is related to the modelling of top-quark-pair production in MC simulation. This motivated several of the measurements discussed in this report that have been or will be used to tune such models, further reducing the impact of systematic uncertainties. Nevertheless, some of the measurements still suffer from significant statistical uncertainty, especially those involving rare processes, such as four- and three-top-quark production, some of those trying to precisely measure small SM effects, e.g. the $t\bar{t}$ charge asymmetry, and those sensitive to BSM effects, such as predicted in differential cross-section measurements in the tails of kinematic distributions.

While the Run 2 analyses of top-quark production and properties are not over yet, LHC Run 3 is bringing particle physics to a new energy with pp collisions at 13.6 TeV. Although the new energy increases the $t\bar{t}$ cross-section by only 11%, it can have larger effects, for instance increasing the $t\bar{t}t\bar{t}$ cross-section by 20%. There is no doubt that the higher energy will bring further advances in our understanding of the top quark, and perhaps new physics discoveries.

Acknowledgements

We thank CERN for the very successful operation of the LHC and its injectors, as well as the support staff at CERN and at our institutions worldwide without whom ATLAS could not be operated efficiently.

The crucial computing support from all WLCG partners is acknowledged gratefully, in particular from CERN, the ATLAS Tier-1 facilities at TRIUMF/SFU (Canada), NDGF (Denmark, Norway, Sweden), CC-IN2P3 (France), KIT/GridKA (Germany), INFN-CNAF (Italy), NL-T1 (Netherlands), PIC (Spain),

RAL (UK) and BNL (USA), the Tier-2 facilities worldwide and large non-WLCG resource providers. Major contributors of computing resources are listed in Ref. [271].

We gratefully acknowledge the support of ANPCyT, Argentina; YerPhI, Armenia; ARC, Australia; BMWFW and FWF, Austria; ANAS, Azerbaijan; CNPq and FAPESP, Brazil; NSERC, NRC and CFI, Canada; CERN; ANID, Chile; CAS, MOST and NSFC, China; Minciencias, Colombia; MEYS CR, Czech Republic; DNRF and DNSRC, Denmark; IN2P3-CNRS and CEA-DRF/IRFU, France; SRNSFG, Georgia; BMBF, HGF and MPG, Germany; GSRI, Greece; RGC and Hong Kong SAR, China; ISF and Benoziyo Center, Israel; INFN, Italy; MEXT and JSPS, Japan; CNRST, Morocco; NWO, Netherlands; RCN, Norway; MEiN, Poland; FCT, Portugal; MNE/IFA, Romania; MESTD, Serbia; MSSR, Slovakia; ARRS and MIZŠ, Slovenia; DSI/NRF, South Africa; MICINN, Spain; SRC and Wallenberg Foundation, Sweden; SERI, SNSF and Cantons of Bern and Geneva, Switzerland; MOST, Taipei; TENMAK, Türkiye; STFC, United Kingdom; DOE and NSF, United States of America.

Individual groups and members have received support from BCKDF, CANARIE, CRC and DRAC, Canada; PRIMUS 21/SCI/017, CERN-CZ and FORTE, Czech Republic; COST, ERC, ERDF, Horizon 2020, ICSC-NextGenerationEU and Marie Skłodowska-Curie Actions, European Union; Investissements d’Avenir Labex, Investissements d’Avenir Idex and ANR, France; DFG and AvH Foundation, Germany; Herakleitos, Thales and Aristeia programmes co-financed by EU-ESF and the Greek NSRF, Greece; BSF-NSF and MINERVA, Israel; Norwegian Financial Mechanism 2014-2021, Norway; NCN and NAWA, Poland; La Caixa Banking Foundation, CERCA Programme Generalitat de Catalunya and PROMETEO and GenT Programmes Generalitat Valenciana, Spain; Göran Gustafssons Stiftelse, Sweden; The Royal Society and Leverhulme Trust, United Kingdom.

In addition, individual members wish to acknowledge support from CERN: European Organization for Nuclear Research (CERN PJA5); Chile: Agencia Nacional de Investigación y Desarrollo (FONDECYT 1190886, FONDECYT 1210400, FONDECYT 1230987); China: National Natural Science Foundation of China (NSFC - 12175119, NSFC 12275265); Czech Republic: Czech Science Foundation (GACR - 24-11373S), Ministry of Education Youth and Sports (FORTE CZ.02.01.01/00/22_008/0004632); European Union: European Research Council (ERC - 948254, ERC 101089007), Horizon 2020 Framework Programme (MUCCA - CHIST-ERA-19-XAI-00), Italian Center for High Performance Computing, Big Data and Quantum Computing (ICSC, NextGenerationEU); France: Agence Nationale de la Recherche (ANR-20-CE31-0013, ANR-21-CE31-0013, ANR-21-CE31-0022), Investissements d’Avenir Labex (ANR-11-LABX-0012); Germany: Baden-Württemberg Stiftung (BW Stiftung-Postdoc Eliteprogramme), Deutsche Forschungsgemeinschaft (DFG - 469666862, DFG - CR 312/5-2); Italy: Istituto Nazionale di Fisica Nucleare (ICSC, NextGenerationEU); Japan: Japan Society for the Promotion of Science (JSPS KAKENHI 22H01227, JSPS KAKENHI 22KK0227, JSPS KAKENHI JP21H05085, JSPS KAKENHI JP22H04944); Netherlands: Netherlands Organisation for Scientific Research (NWO Veni 2020 - VI.Veni.202.179); Norway: Research Council of Norway (RCN-314472); Poland: Polish National Agency for Academic Exchange (PPN/PPO/2020/1/00002/U/00001), Polish National Science Centre (NCN 2021/42/E/ST2/00350, NCN OPUS nr 2022/47/B/ST2/03059, NCN UMO-2019/34/E/ST2/00393, UMO-2020/37/B/ST2/01043, UMO-2021/40/C/ST2/00187, UMO-2022/47/O/ST2/00148); Slovenia: Slovenian Research Agency (ARIS grant J1-3010); Spain: Generalitat Valenciana (Artemisa, FEDER, IDIFEDER/2018/048), Ministry of Science and Innovation (RYC2019-028510-I, RYC2020-030254-I), PROMETEO and GenT Programmes Generalitat Valenciana (CIDEGENT/2019/023, CIDEGENT/2019/027); Sweden: Swedish Research Council (VR 2022-03845, VR 2022-04683, VR 2023-03403), Knut and Alice Wallenberg Foundation (KAW 2018.0157, KAW 2019.0447, KAW 2022.0358); Switzerland: Swiss National Science Foundation

(SNSF - PCEFP2_194658); United Kingdom: Leverhulme Trust (Leverhulme Trust RPG-2020-004), Royal Society (NIF-R1-231091); United States of America: Neubauer Family Foundation.

References

- [1] D0 Collaboration, *Observation of the top quark*, *Phys. Rev. Lett.* **74** (1995) 2632, arXiv: [hep-ex/9503003](#).
- [2] CDF Collaboration, *Observation of Top Quark Production in $\bar{p}p$ Collisions with the Collider Detector at Fermilab*, *Phys. Rev. Lett.* **74** (1995) 2626, arXiv: [hep-ex/9503002](#).
- [3] ATLAS Collaboration, *The ATLAS Experiment at the CERN Large Hadron Collider*, *JINST* **3** (2008) S08003.
- [4] CMS Collaboration, *The CMS Experiment at the CERN LHC*, *JINST* **3** (2008) S08004.
- [5] S. Alekhin, A. Djouadi and S. Moch, *The top quark and Higgs boson masses and the stability of the electroweak vacuum*, *Phys. Lett. B* **716** (2012) 214, arXiv: [1207.0980 \[hep-ph\]](#).
- [6] J. R. Espinosa, *Implications of the top (and Higgs) mass for vacuum stability*, *PoS TOP2015* (2016) 043, ed. by L. Lista, F. Margaroli and F. Tramontano, arXiv: [1512.01222 \[hep-ph\]](#).
- [7] ATLAS Collaboration, *Exploration at the high-energy frontier: ATLAS Run 2 searches investigating the exotic jungle beyond the Standard Model*, (2024), arXiv: [2403.09292 \[hep-ex\]](#).
- [8] ATLAS Collaboration, *Performance of the ATLAS trigger system in 2015*, *Eur. Phys. J. C* **77** (2017) 317, arXiv: [1611.09661 \[hep-ex\]](#).
- [9] ATLAS Collaboration, *The performance of the jet trigger for the ATLAS detector during 2011 data taking*, *Eur. Phys. J. C* **76** (2016) 526, arXiv: [1606.07759 \[hep-ex\]](#).
- [10] ATLAS Collaboration, *Configuration and performance of the ATLAS b-jet triggers in Run 2*, *Eur. Phys. J. C* **81** (2021) 1087, arXiv: [2106.03584 \[hep-ex\]](#).
- [11] ATLAS Collaboration, *Performance of the ATLAS muon triggers in Run 2*, *JINST* **15** (2020) P09015, arXiv: [2004.13447 \[physics.ins-det\]](#).
- [12] ATLAS Collaboration, *Performance of electron and photon triggers in ATLAS during LHC Run 2*, *Eur. Phys. J. C* **80** (2020) 47, arXiv: [1909.00761 \[hep-ex\]](#).
- [13] ATLAS Collaboration, *ATLAS Insertable B-Layer: Technical Design Report*, ATLAS-TDR-19; CERN-LHCC-2010-013, 2010, URL: <https://cds.cern.ch/record/1291633>, Addendum: ATLAS-TDR-19-ADD-1; CERN-LHCC-2012-009, 2012, URL: <https://cds.cern.ch/record/1451888>.
- [14] B. Abbott et al., *Production and integration of the ATLAS Insertable B-Layer*, *JINST* **13** (2018) T05008, arXiv: [1803.00844 \[physics.ins-det\]](#).
- [15] ATLAS Collaboration, *ATLAS flavour-tagging algorithms for the LHC Run 2 pp collision dataset*, *Eur. Phys. J. C* **83** (2023) 681, arXiv: [2211.16345 \[physics.data-an\]](#).

- [16] ATLAS Collaboration, *ATLAS b-jet identification performance and efficiency measurement with $t\bar{t}$ events in pp collisions at $\sqrt{s} = 13$ TeV*, *Eur. Phys. J. C* **79** (2019) 970, arXiv: 1907.05120 [hep-ex].
- [17] ATLAS Collaboration, *Calibration of the light-flavour jet mistagging efficiency of the b-tagging algorithms with Z+jets events using 139 fb^{-1} of ATLAS proton–proton collision data at $\sqrt{s} = 13$ TeV*, *Eur. Phys. J. C* **83** (2023) 728, arXiv: 2301.06319 [hep-ex].
- [18] ATLAS Collaboration, *Measurement of the c-jet mistagging efficiency in $t\bar{t}$ events using pp collision data at $\sqrt{s} = 13$ TeV collected with the ATLAS detector*, *Eur. Phys. J. C* **82** (2022) 95, arXiv: 2109.10627 [hep-ex].
- [19] ATLAS Collaboration, *Dependence of the Jet Energy Scale on the Particle Content of Hadronic Jets in the ATLAS Detector Simulation*, ATL-PHYS-PUB-2022-021, 2022, URL: <https://cds.cern.ch/record/2808016>.
- [20] ATLAS Collaboration, *Jet energy scale and resolution measured in proton–proton collisions at $\sqrt{s} = 13$ TeV with the ATLAS detector*, *Eur. Phys. J. C* **81** (2021) 689, arXiv: 2007.02645 [hep-ex].
- [21] ATLAS Collaboration, *In situ calibration of large-radius jet energy and mass in 13 TeV proton–proton collisions with the ATLAS detector*, *Eur. Phys. J. C* **79** (2019) 135, arXiv: 1807.09477 [hep-ex].
- [22] ATLAS Collaboration, *Performance of pile-up mitigation techniques for jets in pp collisions at $\sqrt{s} = 8$ TeV using the ATLAS detector*, *Eur. Phys. J. C* **76** (2016) 581, arXiv: 1510.03823 [hep-ex].
- [23] ATLAS Collaboration, *Electron reconstruction and identification in the ATLAS experiment using the 2015 and 2016 LHC proton–proton collision data at $\sqrt{s} = 13$ TeV*, *Eur. Phys. J. C* **79** (2019) 639, arXiv: 1902.04655 [physics.ins-det].
- [24] ATLAS Collaboration, *Electron and photon efficiencies in LHC Run 2 with the ATLAS experiment*, (2023), arXiv: 2308.13362 [hep-ex].
- [25] ATLAS Collaboration, *Studies of the muon momentum calibration and performance of the ATLAS detector with pp collisions at $\sqrt{s} = 13$ TeV*, *Eur. Phys. J. C* **83** (2023) 686, arXiv: 2212.07338 [hep-ex].
- [26] ATLAS Collaboration, *Luminosity determination in pp collisions at $\sqrt{s} = 13$ TeV using the ATLAS detector at the LHC*, ATLAS-CONF-2019-021, 2019, URL: <https://cds.cern.ch/record/2677054>.
- [27] ATLAS Collaboration, *Luminosity determination in pp collisions at $\sqrt{s} = 13$ TeV using the ATLAS detector at the LHC*, *Eur. Phys. J. C* **83** (2023) 982, arXiv: 2212.09379 [hep-ex].
- [28] ATLAS Collaboration, *Muon reconstruction and identification efficiency in ATLAS using the full Run 2 pp collision data set at $\sqrt{s} = 13$ TeV*, *Eur. Phys. J. C* **81** (2021) 578, arXiv: 2012.00578 [hep-ex].
- [29] ATLAS Collaboration, *Evidence for the associated production of the Higgs boson and a top quark pair with the ATLAS detector*, *Phys. Rev. D* **97** (2018) 072003, arXiv: 1712.08891 [hep-ex].

- [30] ATLAS Collaboration, *Topological cell clustering in the ATLAS calorimeters and its performance in LHC Run 1*, *Eur. Phys. J. C* **77** (2017) 490, arXiv: [1603.02934 \[hep-ex\]](#).
- [31] ATLAS Collaboration, *Jet reconstruction and performance using particle flow with the ATLAS Detector*, *Eur. Phys. J. C* **77** (2017) 466, arXiv: [1703.10485 \[hep-ex\]](#).
- [32] M. Cacciari, G. P. Salam and G. Soyez, *The anti- k_r jet clustering algorithm*, *JHEP* **04** (2008) 063, arXiv: [0802.1189 \[hep-ph\]](#).
- [33] M. Cacciari, G. P. Salam and G. Soyez, *FastJet User Manual*, *Eur. Phys. J. C* **72** (2012) 1896, arXiv: [1111.6097 \[hep-ph\]](#).
- [34] B. Nachman, P. Nef, A. Schwartzman, M. Swiatlowski and C. Wanotayaroj, *Jets from Jets: Re-clustering as a tool for large radius jet reconstruction and grooming at the LHC*, *JHEP* **02** (2015) 075, arXiv: [1407.2922 \[hep-ph\]](#).
- [35] D. Krohn, J. Thaler and L.-T. Wang, *Jet Trimming*, *JHEP* **02** (2010) 084, arXiv: [0912.1342 \[hep-ph\]](#).
- [36] M. Dasgupta, A. Fregoso, S. Marzani and G. P. Salam, *Towards an understanding of jet substructure*, *JHEP* **09** (2013) 029, arXiv: [1307.0007 \[hep-ph\]](#).
- [37] A. J. Larkoski, S. Marzani, G. Soyez and J. Thaler, *Soft Drop*, *JHEP* **05** (2014) 146, arXiv: [1402.2657 \[hep-ph\]](#).
- [38] ATLAS Collaboration, *Optimisation of large-radius jet reconstruction for the ATLAS detector in 13 TeV proton–proton collisions*, *Eur. Phys. J. C* **81** (2021) 334, arXiv: [2009.04986 \[hep-ex\]](#).
- [39] ATLAS Collaboration, *The performance of missing transverse momentum reconstruction and its significance with the ATLAS detector using 140 fb^{-1} of $\sqrt{s} = 13 \text{ TeV}$ pp collisions*, (2024), arXiv: [2402.05858 \[hep-ex\]](#).
- [40] G. D’Agostini, *A Multidimensional unfolding method based on Bayes’ theorem*, *Nucl. Instrum. Meth. A* **362** (1995) 487.
- [41] G. D’Agostini, ‘Improved iterative Bayesian unfolding’, *Alliance Workshop on Unfolding and Data Correction*, 2010, arXiv: [1010.0632 \[physics.data-an\]](#).
- [42] G. Choudalakis, *Fully Bayesian Unfolding*, (2012), arXiv: [1201.4612 \[physics.data-an\]](#).
- [43] V. Blobel, ‘An Unfolding method for high-energy physics experiments’, *Conference on Advanced Statistical Techniques in Particle Physics*, 2002 258, arXiv: [hep-ex/0208022](#).
- [44] G. Cowan, *Statistical data analysis*, Oxford University Press, 1998.
- [45] A. L. Read, *Presentation of search results: The CL_s technique*, *J. Phys. G* **28** (2002) 2693, ed. by M. R. Whalley and L. Lyons.
- [46] G. Cowan, K. Cranmer, E. Gross and O. Vitells, *Asymptotic formulae for likelihood-based tests of new physics*, *Eur. Phys. J. C* **71** (2011) 1554, arXiv: [1007.1727 \[physics.data-an\]](#), Erratum: *Eur. Phys. J. C* **73** (2013) 2501.
- [47] ATLAS Collaboration, *Measurements of b -jet tagging efficiency with the ATLAS detector using $t\bar{t}$ events at $\sqrt{s} = 13 \text{ TeV}$* , *JHEP* **08** (2018) 089, arXiv: [1805.01845 \[hep-ex\]](#).

- [48] ATLAS Collaboration, *Improvements in $t\bar{t}$ modelling using NLO+PS Monte Carlo generators for Run 2*, ATL-PHYS-PUB-2018-009, 2018, URL: <https://cds.cern.ch/record/2630327>.
- [49] S. Alioli, P. Nason, C. Oleari and E. Re, *A general framework for implementing NLO calculations in shower Monte Carlo programs: the POWHEG BOX*, *JHEP* **06** (2010) 043, arXiv: [1002.2581](https://arxiv.org/abs/1002.2581) [[hep-ph](#)].
- [50] T. Sjöstrand, S. Mrenna and P. Z. Skands, *PYTHIA 6.4 physics and manual*, *JHEP* **05** (2006) 026, arXiv: [hep-ph/0603175](https://arxiv.org/abs/hep-ph/0603175).
- [51] D. J. Lange, *The EvtGen particle decay simulation package*, *Nucl. Instrum. Meth. A* **462** (2001) 152, ed. by S. Erhan, P. Schlein and Y. Rozen.
- [52] T. Sjöstrand et al., *An introduction to PYTHIA 8.2*, *Comput. Phys. Commun.* **191** (2015) 159, arXiv: [1410.3012](https://arxiv.org/abs/1410.3012) [[hep-ph](#)].
- [53] P. Z. Skands, *Tuning Monte Carlo Generators: The Perugia Tunes*, *Phys. Rev. D* **82** (2010) 074018, arXiv: [1005.3457](https://arxiv.org/abs/1005.3457) [[hep-ph](#)].
- [54] ATLAS Collaboration, *ATLAS Pythia 8 tunes to 7 TeV data*, ATL-PHYS-PUB-2014-021, 2014, URL: <https://cds.cern.ch/record/1966419>.
- [55] J. Bellm et al., *Herwig 7.0/Herwig++ 3.0 release note*, *Eur. Phys. J. C* **76** (2016) 196, arXiv: [1512.01178](https://arxiv.org/abs/1512.01178) [[hep-ph](#)].
- [56] J. Alwall et al., *The automated computation of tree-level and next-to-leading order differential cross sections, and their matching to parton shower simulations*, *JHEP* **07** (2014) 079, arXiv: [1405.0301](https://arxiv.org/abs/1405.0301) [[hep-ph](#)].
- [57] E. Bothmann et al., *Event Generation with Sherpa 2.2*, *SciPost Phys.* **7** (2019) 034, arXiv: [1905.09127](https://arxiv.org/abs/1905.09127) [[hep-ph](#)].
- [58] ATLAS Collaboration, *Studies on the improvement of the matching uncertainty definition in top-quark processes simulated with POWHEG+PYTHIA8*, ATL-PHYS-PUB-2023-029, 2013, URL: <https://cds.cern.ch/record/2872787>.
- [59] P. Artoisenet, R. Frederix, O. Mattelaer and R. Rietkerk, *Automatic spin-entangled decays of heavy resonances in Monte Carlo simulations*, *JHEP* **03** (2013) 015, arXiv: [1212.3460](https://arxiv.org/abs/1212.3460) [[hep-ph](#)].
- [60] M. Czakon et al., *Top-pair production at the LHC through NNLO QCD and NLO EW*, *JHEP* **10** (2017) 186, arXiv: [1705.04105](https://arxiv.org/abs/1705.04105) [[hep-ph](#)].
- [61] NNPDF Collaboration, R. D. Ball et al., *Parton distributions for the LHC run II*, *JHEP* **04** (2015) 040, arXiv: [1410.8849](https://arxiv.org/abs/1410.8849) [[hep-ph](#)].
- [62] J. Butterworth et al., *PDF4LHC recommendations for LHC Run II*, *J. Phys. G* **43** (2016) 023001, arXiv: [1510.03865](https://arxiv.org/abs/1510.03865) [[hep-ph](#)].
- [63] ATLAS Collaboration, *A study of different colour reconnection settings for Pythia8 generator using underlying event observables*, ATL-PHYS-PUB-2017-008, 2017, URL: <https://cds.cern.ch/record/2262253>.
- [64] T. Sjöstrand, *Colour reconnection and its effects on precise measurements at the LHC*, (2013), arXiv: [1310.8073](https://arxiv.org/abs/1310.8073) [[hep-ph](#)].
- [65] S. Argyropoulos and T. Sjöstrand, *Effects of color reconnection on $t\bar{t}$ final states at the LHC*, *JHEP* **11** (2014) 043, arXiv: [1407.6653](https://arxiv.org/abs/1407.6653) [[hep-ph](#)].

- [66] S. Frixione, E. Laenen, P. Motylinski, C. D. White and B. R. Webber, *Single-top hadroproduction in association with a W boson*, *JHEP* **07** (2008) 029, arXiv: [0805.3067](https://arxiv.org/abs/0805.3067) [[hep-ph](#)].
- [67] ATLAS Collaboration, *Modelling of rare top quark processes at $\sqrt{s} = 13$ TeV in ATLAS*, ATL-PHYS-PUB-2020-024, 2020, URL: <https://cds.cern.ch/record/2730584>.
- [68] ATLAS Collaboration, *Study of $t\bar{t}b\bar{b}$ and $t\bar{t}W$ background modelling for $t\bar{t}H$ analyses*, ATL-PHYS-PUB-2022-026, 2022, URL: <https://cds.cern.ch/record/2810864>.
- [69] ATLAS Collaboration, *Studies of $t\bar{t}$ / tW interference effects in $b\bar{b}\ell^+\ell'^-\nu\bar{\nu}'$ final states with Powheg and MG5_aMC@NLO setups*, ATL-PHYS-PUB-2021-042, 2021, URL: <https://cds.cern.ch/record/2792254>.
- [70] J. Mazzitelli et al., *Top-pair production at the LHC with MINNLO_{PS}*, *JHEP* **04** (2022) 079, arXiv: [2112.12135](https://arxiv.org/abs/2112.12135) [[hep-ph](#)].
- [71] ATLAS Collaboration, *Measurement of differential cross sections in $t\bar{t}$ and $t\bar{t}$ +jets production in the lepton+jets decay mode in pp collisions at $\sqrt{s} = 13$ TeV using 140 fb^{-1} of ATLAS data*, ATLAS-CONF-2023-068, 2023, URL: <https://cds.cern.ch/record/2873524>.
- [72] M. Czakon, P. Fiedler and A. Mitov, *Total Top-Quark Pair-Production Cross Section at Hadron Colliders Through $O(\alpha_S^4)$* , *Phys. Rev. Lett.* **110** (2013) 252004, arXiv: [1303.6254](https://arxiv.org/abs/1303.6254) [[hep-ph](#)].
- [73] W. Bernreuther, M. Fückler and Z.-G. Si, *Weak interaction corrections to hadronic top quark pair production*, *Phys. Rev. D* **74** (2006) 113005, arXiv: [hep-ph/0610334](https://arxiv.org/abs/hep-ph/0610334).
- [74] J. H. Kühn, A. Scharf and P. Uwer, *Weak interaction effects in top-quark pair production at hadron colliders*, *Eur. Phys. J. C* **51** (2007) 37, arXiv: [hep-ph/0610335](https://arxiv.org/abs/hep-ph/0610335).
- [75] W. Hollik and M. Kollár, *NLO QED contributions to top-pair production at hadron colliders*, *Phys. Rev. D* **77** (2008) 014008, arXiv: [0708.1697](https://arxiv.org/abs/0708.1697) [[hep-ph](#)].
- [76] M. Cacciari, M. Czakon, M. Mangano, A. Mitov and P. Nason, *Top-pair production at hadron colliders with next-to-next-to-leading logarithmic soft-gluon resummation*, *Phys. Lett. B* **710** (2012) 612, arXiv: [1111.5869](https://arxiv.org/abs/1111.5869) [[hep-ph](#)].
- [77] N. Kidonakis, M. Guzzi and A. Tonero, *Top-quark cross sections and distributions at approximate N^3 LO*, *Phys. Rev. D* **108** (2023) 054012, arXiv: [2306.06166](https://arxiv.org/abs/2306.06166) [[hep-ph](#)].
- [78] R. D. Ball et al., *The PDF4LHC21 combination of global PDF fits for the LHC Run III*, *J. Phys. G* **49** (2022) 080501, arXiv: [2203.05506](https://arxiv.org/abs/2203.05506) [[hep-ph](#)].
- [79] M. Czakon and A. Mitov, *Top++: A Program for the Calculation of the Top-Pair Cross-Section at Hadron Colliders*, *Comput. Phys. Commun.* **185** (2014) 2930, arXiv: [1112.5675](https://arxiv.org/abs/1112.5675) [[hep-ph](#)].
- [80] ATLAS Collaboration, *Measurement of the $t\bar{t}$ production cross-section using $e\mu$ events with b -tagged jets in pp collisions at $\sqrt{s} = 13$ TeV with the ATLAS detector*, *Phys. Lett. B* **761** (2016) 136, arXiv: [1606.02699](https://arxiv.org/abs/1606.02699) [[hep-ex](#)], Erratum: *Phys. Lett. B* **772** (2017) 879.

- [81] ATLAS Collaboration, *Measurement of the $t\bar{t}$ production cross-section using $e\mu$ events with b -tagged jets in pp collisions at $\sqrt{s} = 7$ and 8 TeV with the ATLAS detector*, [Eur. Phys. J. C **74** \(2014\) 3109](#), arXiv: [1406.5375 \[hep-ex\]](#), Addendum: [Eur. Phys. J. C **76** \(2016\) 642](#).
- [82] ATLAS Collaboration, *Measurement of the $t\bar{t}$ production cross-section and lepton differential distributions in $e\mu$ dilepton events from pp collisions at $\sqrt{s} = 13$ TeV with the ATLAS detector*, [Eur. Phys. J. C **80** \(2020\) 528](#), arXiv: [1910.08819 \[hep-ex\]](#).
- [83] ATLAS Collaboration, *Inclusive and differential cross-sections for dilepton $t\bar{t}$ production measured in $\sqrt{s} = 13$ TeV pp collisions with the ATLAS detector*, [JHEP **07** \(2023\) 141](#), arXiv: [2303.15340 \[hep-ex\]](#).
- [84] E. Todesco and J. Wenninger, *Large Hadron Collider momentum calibration and accuracy*, [Phys. Rev. Accel. Beams **20** \(2017\) 081003](#).
- [85] ATLAS Collaboration, *Measurements of top-quark pair to Z-boson cross-section ratios at $\sqrt{s} = 13, 8, 7$ TeV with the ATLAS detector*, [JHEP **02** \(2017\) 117](#), arXiv: [1612.03636 \[hep-ex\]](#).
- [86] ATLAS Collaboration, *Measurement of the $t\bar{t}$ production cross-section in the lepton+jets channel at $\sqrt{s} = 13$ TeV with the ATLAS experiment*, [Phys. Lett. B **810** \(2020\) 135797](#), arXiv: [2006.13076 \[hep-ex\]](#).
- [87] ATLAS Collaboration, *Measurements of top-quark pair single- and double-differential cross-sections in the all-hadronic channel in pp collisions at $\sqrt{s} = 13$ TeV using the ATLAS detector*, [JHEP **01** \(2021\) 033](#), arXiv: [2006.09274 \[hep-ex\]](#).
- [88] ATLAS Collaboration, *Measurement of the inclusive $t\bar{t}$ production cross section in the lepton + jets channel in pp collisions at $\sqrt{s} = 7$ TeV with the ATLAS detector using support vector machines*, [Phys. Rev. D **108** \(2023\) 032014](#), arXiv: [2212.00571 \[hep-ex\]](#).
- [89] ATLAS Collaboration, *Measurement of the $t\bar{t}$ production cross-section in pp collisions at $\sqrt{s} = 5.02$ TeV with the ATLAS detector*, [JHEP **06** \(2023\) 138](#), arXiv: [2207.01354 \[hep-ex\]](#).
- [90] ATLAS Collaboration, *Measurement of the $t\bar{t}$ cross section and its ratio to the Z production cross section using pp collisions at $\sqrt{s} = 13.6$ TeV with the ATLAS detector*, [Phys. Lett. B **848** \(2024\) 138376](#), arXiv: [2308.09529 \[hep-ex\]](#).
- [91] ATLAS Collaboration, *Measurement of jet activity produced in top-quark events with an electron, a muon and two b -tagged jets in the final state in pp collisions at $\sqrt{s} = 13$ TeV with the ATLAS detector*, [Eur. Phys. J. C **77** \(2017\) 220](#), arXiv: [1610.09978 \[hep-ex\]](#).
- [92] ATLAS Collaboration, *Measurements of top-quark pair differential cross-sections in the $e\mu$ channel in pp collisions at $\sqrt{s} = 13$ TeV using the ATLAS detector*, [Eur. Phys. J. C **77** \(2017\) 292](#), arXiv: [1612.05220 \[hep-ex\]](#).
- [93] ATLAS Collaboration, *Measurements of top-quark pair differential cross-sections in the lepton+jets channel in pp collisions at $\sqrt{s} = 13$ TeV using the ATLAS detector*, [JHEP **11** \(2017\) 191](#), arXiv: [1708.00727 \[hep-ex\]](#).
- [94] ATLAS Collaboration, *Measurements of differential cross sections of top quark pair production in association with jets in pp collisions at $\sqrt{s} = 13$ TeV using the ATLAS detector*, [JHEP **10** \(2018\) 159](#), arXiv: [1802.06572 \[hep-ex\]](#).

- [95] ATLAS Collaboration, *Measurements of top-quark pair differential and double-differential cross-sections in the ℓ +jets channel with pp collisions at $\sqrt{s} = 13$ TeV using the ATLAS detector*, *Eur. Phys. J. C* **79** (2019) 1028, arXiv: [1908.07305 \[hep-ex\]](#),
Erratum: *Eur. Phys. J. C* **80** (2020) 1092.
- [96] ATLAS Collaboration, *Measurements of $t\bar{t}$ differential cross-sections of highly boosted top quarks decaying to all-hadronic final states in pp collisions at $\sqrt{s} = 13$ TeV using the ATLAS detector*, *Phys. Rev. D* **98** (2018) 012003, arXiv: [1801.02052 \[hep-ex\]](#).
- [97] ATLAS Collaboration, *Measurements of differential cross-sections in top-quark pair events with a high transverse momentum top quark and limits on beyond the Standard Model contributions to top-quark pair production with the ATLAS detector at $\sqrt{s} = 13$ TeV*, *JHEP* **06** (2022) 063, arXiv: [2202.12134 \[hep-ex\]](#).
- [98] ATLAS Collaboration, *Differential $t\bar{t}$ cross-section measurements using boosted top quarks in the all-hadronic final state with 139 fb^{-1} of ATLAS data*, *JHEP* **04** (2023) 080, arXiv: [2205.02817 \[hep-ex\]](#).
- [99] D0 Collaboration, *Measurement of the top quark mass using dilepton events*, *Phys. Rev. Lett.* **80** (1998) 2063, arXiv: [hep-ex/9706014](#).
- [100] ATLAS Collaboration, *Measurement of lepton differential distributions and the top quark mass in $t\bar{t}$ production in pp collisions at $\sqrt{s} = 8$ TeV with the ATLAS detector*, *Eur. Phys. J. C* **77** (2017) 804, arXiv: [1709.09407 \[hep-ex\]](#).
- [101] ATLAS Collaboration, *Differential top-antitop cross-section measurements as a function of observables constructed from final-state particles using pp collisions at $\sqrt{s} = 7$ TeV in the ATLAS detector*, *JHEP* **06** (2015) 100, arXiv: [1502.05923 \[hep-ex\]](#).
- [102] J. Erdmann et al., *A likelihood-based reconstruction algorithm for top-quark pairs and the KLFitter framework*, *Nucl. Instrum. Meth. A* **748** (2014) 18, arXiv: [1312.5595 \[hep-ex\]](#).
- [103] ATLAS Collaboration, *Measurements of inclusive and differential fiducial cross-sections of $t\bar{t}$ production with additional heavy-flavour jets in proton–proton collisions at $\sqrt{s} = 13$ TeV with the ATLAS detector*, *JHEP* **04** (2019) 046, arXiv: [1811.12113 \[hep-ex\]](#).
- [104] ATLAS Collaboration, *Measurements of jet observables sensitive to b -quark fragmentation in $t\bar{t}$ events at the LHC with the ATLAS detector*, *Phys. Rev. D* **106** (2022) 032008, arXiv: [2202.13901 \[hep-ex\]](#).
- [105] T. M. P. Tait and C.-P. Yuan, *Single top quark production as a window to physics beyond the standard model*, *Phys. Rev. D* **63** (2000) 014018, arXiv: [hep-ph/0007298](#).
- [106] Q.-H. Cao, J. Wudka and C.-P. Yuan, *Search for new physics via single-top production at the LHC*, *Phys. Lett. B* **658** (2007) 50, arXiv: [0704.2809 \[hep-ph\]](#).
- [107] J. Campbell, T. Neumann and Z. Sullivan, *Single-top-quark production in the t -channel at NNLO*, *JHEP* **02** (2021) 040, arXiv: [2012.01574 \[hep-ph\]](#).
- [108] ATLAS Collaboration, *Measurement of the inclusive cross-sections of single top-quark and top-antiquark t -channel production in pp collisions at $\sqrt{s} = 13$ TeV with the ATLAS detector*, *JHEP* **04** (2017) 086, arXiv: [1609.03920 \[hep-ex\]](#).

- [109] ATLAS Collaboration, *Measurement of t -channel production of single top quarks and antiquarks in pp collisions at 13 TeV using the full ATLAS Run 2 data sample*, (2024), arXiv: [2403.02126 \[hep-ex\]](#).
- [110] ATLAS Collaboration, *Measurement of the polarisation of single top quarks and antiquarks produced in the t -channel at $\sqrt{s} = 13$ TeV and bounds on the tWb dipole operator from the ATLAS experiment*, *JHEP* **11** (2022) 040, arXiv: [2202.11382 \[hep-ex\]](#).
- [111] J. A. Aguilar-Saavedra and S. Amor Dos Santos, *New directions for top quark polarization in the t -channel process*, *Phys. Rev. D* **89** (2014) 114009, arXiv: [1404.1585 \[hep-ph\]](#).
- [112] ATLAS Collaboration, *Probing the quantum interference between singly and doubly resonant top-quark production in pp collisions at $\sqrt{s} = 13$ TeV with the ATLAS detector*, *Phys. Rev. Lett.* **121** (2018) 152002, arXiv: [1806.04667 \[hep-ex\]](#).
- [113] CMS Collaboration, *Observation of the associated production of a single top quark and a W boson in pp collisions at $\sqrt{s} = 8$ TeV*, *Phys. Rev. Lett.* **112** (2014) 231802, arXiv: [1401.2942 \[hep-ex\]](#).
- [114] ATLAS Collaboration, *Measurement of the production cross-section of a single top quark in association with a W boson at 8 TeV with the ATLAS experiment*, *JHEP* **01** (2016) 064, arXiv: [1510.03752 \[hep-ex\]](#).
- [115] N. Kidonakis and N. Yamanaka, *Higher-order corrections for tW production at high-energy hadron colliders*, *JHEP* **05** (2021) 278, arXiv: [2102.11300 \[hep-ph\]](#).
- [116] ATLAS Collaboration, *Measurement of the cross-section for producing a W boson in association with a single top quark in pp collisions at $\sqrt{s} = 13$ TeV with ATLAS*, *JHEP* **01** (2018) 063, arXiv: [1612.07231 \[hep-ex\]](#).
- [117] ATLAS Collaboration, *Measurement of differential cross-sections of a single top quark produced in association with a W boson at $\sqrt{s} = 13$ TeV with ATLAS*, *Eur. Phys. J. C* **78** (2018) 186, arXiv: [1712.01602 \[hep-ex\]](#).
- [118] C. G. Lester and D. J. Summers, *Measuring masses of semi-invisibly decaying particles pair produced at hadron colliders*, *Phys. Lett. B* **463** (1999) 99, arXiv: [hep-ph/9906349](#).
- [119] A. Barr, C. Lester and P. Stephens, *A variable for measuring masses at hadron colliders when missing energy is expected; m_{T2} : the truth behind the glamour*, *J. Phys. G* **29** (2003) 2343, arXiv: [hep-ph/0304226](#).
- [120] T. Ježo, J. M. Lindert, P. Nason, C. Oleari and S. Pozzorini, *An NLO+PS generator for $t\bar{t}$ and Wt production and decay including non-resonant and interference effects*, *Eur. Phys. J. C* **76** (2016) 691, arXiv: [1607.04538 \[hep-ph\]](#).
- [121] T. Ježo and P. Nason, *On the Treatment of Resonances in Next-to-Leading Order Calculations Matched to a Parton Shower*, *JHEP* **12** (2015) 1, arXiv: [1509.09071 \[hep-ph\]](#).
- [122] CDF and D0 Collaborations, *Observation of s -channel production of single top quarks at the Tevatron*, *Phys. Rev. Lett.* **112** (2014) 231803, arXiv: [1402.5126 \[hep-ex\]](#).

- [123] ATLAS Collaboration, *Evidence for single top-quark production in the s-channel in proton-proton collisions at $\sqrt{s}=8$ TeV with the ATLAS detector using the Matrix Element Method*, [Phys. Lett. B **756** \(2016\) 228](#), arXiv: [1511.05980 \[hep-ex\]](#).
- [124] P. Kant et al., *HatHor for single top-quark production: Updated predictions and uncertainty estimates for single top-quark production in hadronic collisions*, [Comput. Phys. Commun. **191** \(2015\) 74](#), arXiv: [1406.4403 \[hep-ph\]](#).
- [125] ATLAS Collaboration, *Measurement of single top-quark production in the s-channel in proton-proton collisions at $\sqrt{s}=13$ TeV with the ATLAS detector*, [JHEP **06** \(2023\) 191](#), arXiv: [2209.08990 \[hep-ex\]](#).
- [126] K. Kondo, *Dynamical Likelihood Method for Reconstruction of Events With Missing Momentum. 1: Method and Toy Models*, [J. Phys. Soc. Jap. **57** \(1988\) 4126](#).
- [127] K. Kondo, *Dynamical likelihood method for reconstruction of events with missing momentum. 2: Mass spectra for $2 \rightarrow 2$ processes*, [J. Phys. Soc. Jap. **60** \(1991\) 836](#).
- [128] N. Cabibbo, *Unitary Symmetry and Leptonic Decays*, [Phys. Rev. Lett. **10** \(1963\) 531](#).
- [129] M. Kobayashi and T. Maskawa, *CP-Violation in the Renormalizable Theory of Weak Interaction*, [Prog. Theor. Phys. **49** \(1973\) 652](#).
- [130] J. A. Aguilar-Saavedra, *A Minimal set of top anomalous couplings*, [Nucl. Phys. B **812** \(2009\) 181](#), arXiv: [0811.3842 \[hep-ph\]](#).
- [131] N. Kidonakis, *Theoretical results for electroweak boson and single-top production*, [PoS **DIS2015** \(2015\) 170](#), arXiv: [1506.04072 \[hep-ph\]](#).
- [132] ATLAS Collaboration, *Characterising the Higgs boson with ATLAS data from Run 2 of the LHC*, (2024), arXiv: [2404.05498 \[hep-ex\]](#).
- [133] J. A. Aguilar-Saavedra, *Identifying top partners at LHC*, [JHEP **11** \(2009\) 030](#), arXiv: [0907.3155 \[hep-ph\]](#).
- [134] J. A. Aguilar-Saavedra, R. Benbrik, S. Heinemeyer and M. Pérez-Victoria, *Handbook of vectorlike quarks: Mixing and single production*, [Phys. Rev. D **88** \(2013\) 094010](#), arXiv: [1306.0572 \[hep-ph\]](#).
- [135] M. Perelstein, *Little Higgs models and their phenomenology*, [Prog. Part. Nucl. Phys. **58** \(2007\) 247](#), arXiv: [hep-ph/0512128](#).
- [136] D. Dicus, A. Stange and S. Willenbrock, *Higgs decay to top quarks at hadron colliders*, [Phys. Lett. B **333** \(1994\) 126](#), arXiv: [hep-ph/9404359](#).
- [137] N. Craig, F. D’Eramo, P. Draper, S. Thomas and H. Zhang, *The Hunt for the Rest of the Higgs Bosons*, [JHEP **06** \(2015\) 137](#), arXiv: [1504.04630 \[hep-ph\]](#).
- [138] N. Craig, J. Hajer, Y.-Y. Li, T. Liu and H. Zhang, *Heavy Higgs bosons at low $\tan\beta$: from the LHC to 100 TeV*, [JHEP **01** \(2017\) 018](#), arXiv: [1605.08744 \[hep-ph\]](#).
- [139] C. Degrande, J.-M. Gérard, C. Grojean, F. Maltoni and G. Servant, *Non-resonant New Physics in Top Pair Production at Hadron Colliders*, [JHEP **03** \(2011\) 125](#), arXiv: [1010.6304 \[hep-ph\]](#).
- [140] C. Zhang, *Constraining $q\bar{q}t\bar{t}$ operators from four-top production: a case for enhanced EFT sensitivity*, [Chin. Phys. C **42** \(2018\) 023104](#), arXiv: [1708.05928 \[hep-ph\]](#).

- [141] ATLAS Collaboration, *Tools for estimating fake/non-prompt lepton backgrounds with the ATLAS detector at the LHC*, [JINST **18** \(2023\) T11004](#), arXiv: [2211.16178 \[hep-ex\]](#).
- [142] ATLAS Collaboration, *Electron and photon performance measurements with the ATLAS detector using the 2015–2017 LHC proton–proton collision data*, [JINST **14** \(2019\) P12006](#), arXiv: [1908.00005 \[hep-ex\]](#).
- [143] ATLAS Collaboration, *Measurement of the $t\bar{t}W$ and $t\bar{t}Z$ production cross sections in pp collisions at $\sqrt{s} = 8$ TeV with the ATLAS detector*, [JHEP **11** \(2015\) 172](#), arXiv: [1509.05276 \[hep-ex\]](#).
- [144] ATLAS Collaboration, *Measurement of the $t\bar{t}Z$ and $t\bar{t}W$ production cross sections in multilepton final states using 3.2 fb^{-1} of pp collisions at $\sqrt{s} = 13$ TeV with the ATLAS detector*, [Eur. Phys. J. C **77** \(2017\) 40](#), arXiv: [1609.01599 \[hep-ex\]](#).
- [145] ATLAS Collaboration, *Measurement of the $t\bar{t}Z$ and $t\bar{t}W$ cross sections in proton–proton collisions at $\sqrt{s} = 13$ TeV with the ATLAS detector*, [Phys. Rev. D **99** \(2019\) 072009](#), arXiv: [1901.03584 \[hep-ex\]](#).
- [146] ATLAS Collaboration, *Measurement of the total and differential cross-sections of $t\bar{t}W$ production in pp collisions at $\sqrt{s} = 13$ TeV with the ATLAS detector*, (2024), arXiv: [2401.05299 \[hep-ex\]](#).
- [147] ATLAS Collaboration, *Inclusive and differential cross-section measurements of $t\bar{t}Z$ production in pp collisions at $\sqrt{s} = 13$ TeV with the ATLAS detector, including EFT and spin-correlation interpretations*, (2023), arXiv: [2312.04450 \[hep-ex\]](#).
- [148] A. Kulesza, L. Motyka, D. Schwartzländer, T. Stebel and V. Theeuwes, *Associated production of a top quark pair with a heavy electroweak gauge boson at NLO+NNLL accuracy*, [Eur. Phys. J. C **79** \(2019\) 249](#), arXiv: [1812.08622 \[hep-ph\]](#).
- [149] L. Buonocore et al., *Precise Predictions for the Associated Production of a W Boson with a Top-Antitop Quark Pair at the LHC*, [Phys. Rev. Lett. **131** \(2023\) 231901](#), arXiv: [2306.16311 \[hep-ph\]](#).
- [150] ATLAS Collaboration, *Measurements of the inclusive and differential production cross sections of a top-quark–antiquark pair in association with a Z boson at $\sqrt{s} = 13$ TeV with the ATLAS detector*, [Eur. Phys. J. C **81** \(2021\) 737](#), arXiv: [2103.12603 \[hep-ex\]](#).
- [151] ATLAS Collaboration, *Measurement of the production cross-section of a single top quark in association with a Z boson in proton–proton collisions at 13 TeV with the ATLAS detector*, [Phys. Lett. B **780** \(2018\) 557](#), arXiv: [1710.03659 \[hep-ex\]](#).
- [152] ATLAS Collaboration, *Observation of the associated production of a top quark and a Z boson in pp collisions at $\sqrt{s} = 13$ TeV with the ATLAS detector*, [JHEP **07** \(2020\) 124](#), arXiv: [2002.07546 \[hep-ex\]](#).
- [153] J. Campbell, R. K. Ellis and R. Röntsch, *Single top production in association with a Z boson at the LHC*, [Phys. Rev. D **87** \(2013\) 114006](#), arXiv: [1302.3856 \[hep-ph\]](#).
- [154] U. Baur, A. Juste, L. H. Orr and D. Rainwater, *Probing electroweak top quark couplings at hadron colliders*, [Phys. Rev. D **71** \(2005\) 054013](#), arXiv: [hep-ph/0412021](#).
- [155] A. O. Bouzas and F. Larios, *Electromagnetic dipole moments of the Top quark*, [Phys. Rev. D **87** \(2013\) 074015](#), arXiv: [1212.6575 \[hep-ph\]](#).

- [156] M. Schulze and Y. Soreq, *Pinning down electroweak dipole operators of the top quark*, *Eur. Phys. J. C* **76** (2016) 466, arXiv: [1603.08911 \[hep-ph\]](#).
- [157] ATLAS Collaboration, *Observation of top-quark pair production in association with a photon and measurement of the $t\bar{t}\gamma$ production cross section in pp collisions at $\sqrt{s} = 7$ TeV using the ATLAS detector*, *Phys. Rev. D* **91** (2015) 072007, arXiv: [1502.00586 \[hep-ex\]](#).
- [158] ATLAS Collaboration, *Measurement of the $t\bar{t}\gamma$ production cross section in proton-proton collisions at $\sqrt{s} = 8$ TeV with the ATLAS detector*, *JHEP* **11** (2017) 086, arXiv: [1706.03046 \[hep-ex\]](#).
- [159] ATLAS Collaboration, *Measurements of inclusive and differential fiducial cross-sections of $t\bar{t}\gamma$ production in leptonic final states at $\sqrt{s} = 13$ TeV in ATLAS*, *Eur. Phys. J. C* **79** (2019) 382, arXiv: [1812.01697 \[hep-ex\]](#).
- [160] ATLAS Collaboration, *Measurements of inclusive and differential cross-sections of combined $t\bar{t}\gamma$ and $tW\gamma$ production in the $e\mu$ channel at 13 TeV with the ATLAS detector*, *JHEP* **09** (2020) 049, arXiv: [2007.06946 \[hep-ex\]](#).
- [161] K. Melnikov, M. Schulze and A. Scharf, *QCD corrections to top quark pair production in association with a photon at hadron colliders*, *Phys. Rev. D* **83** (2011) 074013, arXiv: [1102.1967 \[hep-ph\]](#).
- [162] G. Bevilacqua, H. B. Hartanto, M. Kraus, T. Weber and M. Worek, *Hard Photons in Hadroproduction of Top Quarks with Realistic Final States*, *JHEP* **10** (2018) 158, arXiv: [1803.09916 \[hep-ph\]](#).
- [163] G. Bevilacqua, H. B. Hartanto, M. Kraus, T. Weber and M. Worek, *Precise predictions for $t\bar{t}\gamma/t\bar{t}$ cross section ratios at the LHC*, *JHEP* **01** (2019) 188, arXiv: [1809.08562 \[hep-ph\]](#).
- [164] ATLAS Collaboration, *Observation of Single-Top-Quark Production in Association with a Photon Using the ATLAS Detector*, *Phys. Rev. Lett.* **131** (2023) 181901, arXiv: [2302.01283 \[hep-ex\]](#).
- [165] A. Pomarol and J. Serra, *Top Quark Compositeness: Feasibility and Implications*, *Phys. Rev. D* **78** (2008) 074026, arXiv: [0806.3247 \[hep-ph\]](#).
- [166] H. P. Nilles, *Supersymmetry, Supergravity and Particle Physics*, *Phys. Rept.* **110** (1984) 1.
- [167] G. R. Farrar and P. Fayet, *Phenomenology of the Production, Decay, and Detection of New Hadronic States Associated with Supersymmetry*, *Phys. Lett. B* **76** (1978) 575.
- [168] Q.-H. Cao, S.-L. Chen and Y. Liu, *Probing Higgs Width and Top Quark Yukawa Coupling from $t\bar{t}H$ and $t\bar{t}\bar{t}$ Productions*, *Phys. Rev. D* **95** (2017) 053004, arXiv: [1602.01934 \[hep-ph\]](#).
- [169] Q.-H. Cao, S.-L. Chen, Y. Liu, R. Zhang and Y. Zhang, *Limiting top quark-Higgs boson interaction and Higgs-boson width from multitop productions*, *Phys. Rev. D* **99** (2019) 113003, arXiv: [1901.04567 \[hep-ph\]](#).
- [170] R. Frederix, D. Pagani and M. Zaro, *Large NLO corrections in $t\bar{t}W^\pm$ and $t\bar{t}\bar{t}$ hadroproduction from supposedly subleading EW contributions*, *JHEP* **02** (2018) 031, arXiv: [1711.02116 \[hep-ph\]](#).
- [171] G. Bevilacqua and M. Worek, *Constraining BSM Physics at the LHC: Four top final states with NLO accuracy in perturbative QCD*, *JHEP* **07** (2012) 111, arXiv: [1206.3064 \[hep-ph\]](#).

- [172] T. Ježo and M. Kraus, *Hadroproduction of four top quarks in the powheg box*, *Phys. Rev. D* **105** (2022) 114024, arXiv: 2110.15159 [hep-ph].
- [173] M. van Beekveld, A. Kulesza and L. M. Valero, *Threshold resummation for the production of four top quarks at the LHC*, (2022), arXiv: 2212.03259 [hep-ph].
- [174] ATLAS Collaboration, *Search for new phenomena in events with same-charge leptons and b-jets in pp collisions at $\sqrt{s} = 13$ TeV with the ATLAS detector*, *JHEP* **12** (2018) 039, arXiv: 1807.11883 [hep-ex].
- [175] ATLAS Collaboration, *Evidence for $t\bar{t}\bar{t}$ production in the multilepton final state in proton–proton collisions at $\sqrt{s} = 13$ TeV with the ATLAS detector*, *Eur. Phys. J. C* **80** (2020) 1085, arXiv: 2007.14858 [hep-ex].
- [176] ATLAS Collaboration, *Observation of four-top-quark production in the multilepton final state with the ATLAS detector*, *Eur. Phys. J. C* **83** (2023) 496, arXiv: 2303.15061 [hep-ex].
- [177] ATLAS Collaboration, *Measurement of the properties of Higgs boson production at $\sqrt{s} = 13$ TeV in the $H \rightarrow \gamma\gamma$ channel using 139 fb^{-1} of pp collision data with the ATLAS experiment*, *JHEP* **07** (2023) 088, arXiv: 2207.00348 [hep-ex].
- [178] ATLAS Collaboration, *Probing the CP nature of the top-Higgs Yukawa coupling in $t\bar{t}H$ and tH events with $H \rightarrow b\bar{b}$ decays using the ATLAS detector at the LHC*, (2023), arXiv: 2303.05974 [hep-ex].
- [179] ATLAS Collaboration, *Search for four-top-quark production in the single-lepton and opposite-sign dilepton final states in pp collisions at $\sqrt{s} = 13$ TeV with the ATLAS detector*, *Phys. Rev. D* **99** (2019) 052009, arXiv: 1811.02305 [hep-ex].
- [180] ATLAS Collaboration, *Measurement of the $t\bar{t}\bar{t}$ production cross section in pp collisions at $\sqrt{s} = 13$ TeV with the ATLAS detector*, *JHEP* **11** (2021) 118, arXiv: 2106.11683 [hep-ex].
- [181] ATLAS Collaboration, *Roadmap towards future combinations and Effective Field Theory interpretations of top+X processes*, ATL-PHYS-PUB-2023-030, 2023, URL: <https://cds.cern.ch/record/2872789>.
- [182] Particle Data Group, M. Tanabashi et al., *Review of Particle Physics*, *Phys. Rev. D* **98** (3 2018) 030001.
- [183] A. H. Hoang, *What is the Top Quark Mass?*, *Ann. Rev. Nucl. Part. Sci.* **70** (2020) 225, arXiv: 2004.12915 [hep-ph].
- [184] ATLAS Collaboration, *A precise interpretation for the top quark mass parameter in ATLAS Monte Carlo simulation*, ATL-PHYS-PUB-2021-034, 2021, URL: <https://cds.cern.ch/record/2777332>.
- [185] ATLAS Collaboration, *Measurement of the top quark mass in the $t\bar{t} \rightarrow \text{lepton} + \text{jets}$ channel from $\sqrt{s} = 8$ TeV ATLAS data and combination with previous results*, *Eur. Phys. J. C* **79** (2019) 290, arXiv: 1810.01772 [hep-ex].
- [186] CMS Collaboration, *Measurement of the top quark mass using proton–proton data at $\sqrt{s} = 7$ and 8 TeV*, *Phys. Rev. D* **93** (2016) 072004, arXiv: 1509.04044 [hep-ex].

- [187] Tevatron Electroweak Working Group, *Combination of CDF and D0 results on the mass of the top quark using up 9.7 fb^{-1} at the Tevatron*, (2016), arXiv: [1608.01881 \[hep-ex\]](#).
- [188] ATLAS Collaboration, *Measurement of the top quark mass in the $t\bar{t} \rightarrow$ dilepton channel from $\sqrt{s} = 8 \text{ TeV}$ ATLAS data*, *Phys. Lett. B* **761** (2016) 350, arXiv: [1606.02179 \[hep-ex\]](#).
- [189] ATLAS and CMS Collaborations, *Combination of measurements of the top quark mass from data collected by the ATLAS and CMS experiments at $\sqrt{s} = 7$ and 8 TeV* , (2024), arXiv: [2402.08713 \[hep-ex\]](#).
- [190] ATLAS Collaboration, *Measurement of the top-quark mass using a leptonic invariant mass in pp collisions at $\sqrt{s} = 13 \text{ TeV}$ with the ATLAS detector*, *JHEP* **06** (2023) 019, arXiv: [2209.00583 \[hep-ex\]](#).
- [191] ATLAS Collaboration, *Measurement of the top-quark mass in $t\bar{t} \rightarrow$ dilepton events with the ATLAS experiment using the template method in 13 TeV pp collision data*, ATLAS-CONF-2022-058, 2022, URL: <https://cds.cern.ch/record/2826701>.
- [192] ATLAS Collaboration, *Measurement of the top-quark mass in $t\bar{t} + 1$ -jet events collected with the ATLAS detector in pp collisions at $\sqrt{s} = 8 \text{ TeV}$* , *JHEP* **11** (2019) 150, arXiv: [1905.02302 \[hep-ex\]](#).
- [193] Particle Data Group, R. L. Workman et al., *Review of Particle Physics*, *PTEP* **2022** (2022) 083C01.
- [194] A. Czarnecki, J. G. Körner and J. H. Piclum, *Helicity fractions of W bosons from top quark decays at next-to-next-to-leading order in QCD*, *Phys. Rev. D* **81** (2010) 111503, arXiv: [1005.2625 \[hep-ph\]](#).
- [195] ATLAS Collaboration, *Measurement of the polarisation of W bosons produced in top-quark decays using dilepton events at $\sqrt{s} = 13 \text{ TeV}$ with the ATLAS experiment*, *Phys. Lett. B* **843** (2023) 137829, arXiv: [2209.14903 \[hep-ex\]](#).
- [196] A. Brandenburg, Z. G. Si and P. Uwer, *QCD-corrected spin analyzing power of jets in decays of polarized top quarks*, *Phys. Lett. B* **539** (2002) 235, arXiv: [hep-ph/0205023](#).
- [197] ATLAS Collaboration, *Observation of spin correlation in $t\bar{t}$ events from pp collisions at $\sqrt{s} = 7 \text{ TeV}$ using the ATLAS detector*, *Phys. Rev. Lett.* **108** (2012) 212001, arXiv: [1203.4081 \[hep-ex\]](#).
- [198] ATLAS Collaboration, *Measurements of spin correlation in top-antitop quark events from proton-proton collisions at $\sqrt{s} = 7 \text{ TeV}$ using the ATLAS detector*, *Phys. Rev. D* **90** (2014) 112016, arXiv: [1407.4314 \[hep-ex\]](#).
- [199] ATLAS Collaboration, *Measurement of Spin Correlation in Top-Antitop Quark Events and Search for Top Squark Pair Production in pp Collisions at $\sqrt{s} = 8 \text{ TeV}$ Using the ATLAS Detector*, *Phys. Rev. Lett.* **114** (2015) 142001, arXiv: [1412.4742 \[hep-ex\]](#).
- [200] ATLAS Collaboration, *Measurements of top quark spin observables in $t\bar{t}$ events using dilepton final states in $\sqrt{s} = 8 \text{ TeV}$ pp collisions with the ATLAS detector*, *JHEP* **03** (2017) 113, arXiv: [1612.07004 \[hep-ex\]](#).
- [201] ATLAS Collaboration, *Measurements of top-quark pair spin correlations in the $e\mu$ channel at $\sqrt{s} = 13 \text{ TeV}$ using pp collisions in the ATLAS detector*, *Eur. Phys. J. C* **80** (2020) 754, arXiv: [1903.07570 \[hep-ex\]](#).

- [202] W. Bernreuther, D. Heisler and Z.-G. Si, *A set of top quark spin correlation and polarization observables for the LHC: Standard Model predictions and new physics contributions*, [JHEP **12** \(2015\) 1](#), arXiv: [1508.05271 \[hep-ph\]](#).
- [203] Y. Afik and J. R. M. de Nova, *Entanglement and quantum tomography with top quarks at the LHC*, [Eur. Phys. J. Plus **136** \(2021\) 907](#), arXiv: [2003.02280 \[quant-ph\]](#).
- [204] M. Fabbrichesi, R. Floreanini and G. Panizzo, *Testing Bell Inequalities at the LHC with Top-Quark Pairs*, [Phys. Rev. Lett. **127** \(2021\) 161801](#), arXiv: [2102.11883 \[hep-ph\]](#).
- [205] C. Severi, C. D. E. Boschi, F. Maltoni and M. Sioli, *Quantum tops at the LHC: from entanglement to Bell inequalities*, [Eur. Phys. J. C **82** \(2022\) 285](#), arXiv: [2110.10112 \[hep-ph\]](#).
- [206] J. A. Aguilar-Saavedra and J. A. Casas, *Improved tests of entanglement and Bell inequalities with LHC tops*, [Eur. Phys. J. C **82** \(2022\) 666](#), arXiv: [2205.00542 \[hep-ph\]](#).
- [207] R. Ashby-Pickering, A. J. Barr and A. Wierzychucka, *Quantum state tomography, entanglement detection and Bell violation prospects in weak decays of massive particles*, [JHEP **05** \(2023\) 020](#), arXiv: [2209.13990 \[quant-ph\]](#).
- [208] ATLAS Collaboration, *Observation of quantum entanglement in top-quark pairs using the ATLAS detector*, (2023), arXiv: [2311.07288 \[hep-ex\]](#).
- [209] B. A. Betchart, R. Demina and A. Harel, *Analytic solutions for neutrino momenta in decay of top quarks*, [Nucl. Instrum. Meth. A **736** \(2014\) 169](#), arXiv: [1305.1878 \[hep-ph\]](#).
- [210] Y. Afik and J. R. M. de Nova, *Quantum Discord and Steering in Top Quarks at the LHC*, [Phys. Rev. Lett. **130** \(2023\) 221801](#), arXiv: [2209.03969 \[quant-ph\]](#).
- [211] Y. Afik and J. R. M. de Nova, *Quantum information with top quarks in QCD*, [Quantum **6** \(2022\) 820](#), arXiv: [2203.05582 \[quant-ph\]](#).
- [212] O. Antuñano, J. H. Kühn and G. Rodrigo, *Top quarks, axiguons, and charge asymmetries at hadron colliders*, [Phys. Rev. D **77** \(2008\) 014003](#), arXiv: [0709.1652 \[hep-ph\]](#).
- [213] P. H. Frampton, J. Shu and K. Wang, *Axiguon as possible explanation for $p\bar{p} \rightarrow t\bar{t}$ forward-backward asymmetry*, [Phys. Lett. B **683** \(2010\) 294](#), arXiv: [0911.2955 \[hep-ph\]](#).
- [214] J. L. Rosner, *Prominent decay modes of a leptophobic Z'* , [Phys. Lett. B **387** \(1996\) 113](#), arXiv: [hep-ph/9607207](#).
- [215] J. A. Aguilar-Saavedra and M. Pérez-Victoria, *Asymmetries in $t\bar{t}$ production: LHC versus Tevatron*, [Phys. Rev. D **84** \(2011\) 115013](#), arXiv: [1105.4606 \[hep-ph\]](#).
- [216] M. P. Roselló and M. Vos, *Constraints on four-fermion interactions from the $t\bar{t}$ charge asymmetry at hadron colliders*, [Eur. Phys. J. C **76** \(2016\) 200](#), arXiv: [1512.07542 \[hep-ex\]](#).
- [217] J. A. Aguilar-Saavedra, A. Juste and F. Rubbo, *Boosting the $t\bar{t}$ charge asymmetry*, [Phys. Lett. B **707** \(2012\) 92](#), arXiv: [1109.3710 \[hep-ph\]](#).

- [218] ATLAS and CMS Collaborations, *Combination of inclusive and differential $t\bar{t}$ charge asymmetry measurements using ATLAS and CMS data at $\sqrt{s} = 7$ and 8 TeV*, *JHEP* **04** (2018) 033, arXiv: 1709.05327 [hep-ex].
- [219] ATLAS Collaboration, *Evidence for the charge asymmetry in $pp \rightarrow t\bar{t}$ production at $\sqrt{s} = 13$ TeV with the ATLAS detector*, *JHEP* **08** (2023) 077, arXiv: 2208.12095 [hep-ex].
- [220] M. Czakon et al., *Top-quark charge asymmetry at the LHC and Tevatron through NNLO QCD and NLO EW*, *Phys. Rev. D* **98** (2018) 014003, arXiv: 1711.03945 [hep-ph].
- [221] W. Bernreuther and Z.-G. Si, *Top quark and leptonic charge asymmetries for the Tevatron and LHC*, *Phys. Rev. D* **86** (2012) 034026, arXiv: 1205.6580 [hep-ph].
- [222] S. Berge and S. Westhoff, *Top-Quark Charge Asymmetry Goes Forward: Two New Observables for Hadron Colliders*, *JHEP* **07** (2013) 179, arXiv: 1305.3272 [hep-ph].
- [223] ATLAS Collaboration, *Measurement of the energy asymmetry in $t\bar{t}j$ production at 13 TeV with the ATLAS experiment and interpretation in the SMEFT framework*, *Eur. Phys. J. C* **82** (2022) 374, arXiv: 2110.05453 [hep-ex].
- [224] F. Maltoni, M. L. Mangano, I. Tsinikos and M. Zaro, *Top-quark charge asymmetry and polarization in $t\bar{t}W^\pm$ production at the LHC*, *Phys. Lett. B* **736** (2014) 252, arXiv: 1406.3262 [hep-ph].
- [225] G. Bevilacqua et al., *NLO QCD corrections to off-shell $t\bar{t}W^\pm$ production at the LHC: correlations and asymmetries*, *Eur. Phys. J. C* **81** (2021) 675, arXiv: 2012.01363 [hep-ph].
- [226] ATLAS Collaboration, *Search for leptonic charge asymmetry in $t\bar{t}W$ production in final states with three leptons at $\sqrt{s} = 13$ TeV*, *JHEP* **07** (2023) 033, arXiv: 2301.04245 [hep-ex].
- [227] J. A. Aguilar-Saavedra, E. Álvarez, A. Juste and F. Rubbo, *Shedding light on the $t\bar{t}$ asymmetry: the photon handle*, *JHEP* **04** (2014) 188, arXiv: 1402.3598 [hep-ph].
- [228] D. Pagani, H.-S. Shao, I. Tsinikos and M. Zaro, *Automated EW corrections with isolated photons: $t\bar{t}\gamma$, $t\bar{t}\gamma\gamma$ and $t\gamma j$ as case studies*, *JHEP* **09** (2021) 155, arXiv: 2106.02059 [hep-ph].
- [229] J. Bergner and M. Schulze, *The top quark charge asymmetry in $t\bar{t}\gamma$ production at the LHC*, *Eur. Phys. J. C* **79** (2019) 189, arXiv: 1812.10535 [hep-ph].
- [230] ATLAS Collaboration, *Measurement of the charge asymmetry in top-quark pair production in association with a photon with the ATLAS experiment*, *Phys. Lett. B* **843** (2023) 137848, arXiv: 2212.10552 [hep-ex].
- [231] ATLAS Collaboration, *Measurement of colour flow with the jet pull angle in $t\bar{t}$ events using the ATLAS detector at $\sqrt{s} = 8$ TeV*, *Phys. Lett. B* **750** (2015) 475, arXiv: 1506.05629 [hep-ex].
- [232] ATLAS Collaboration, *Measurement of colour flow using jet-pull observables in $t\bar{t}$ events with the ATLAS experiment at $\sqrt{s} = 13$ TeV*, *Eur. Phys. J. C* **78** (2018) 847, arXiv: 1805.02935 [hep-ex].

- [233] J. Gallicchio and M. D. Schwartz, *Seeing in Color: Jet Superstructure*, *Phys. Rev. Lett.* **105** (2010) 022001, arXiv: [1001.5027 \[hep-ph\]](#).
- [234] Z. Nagy and D. E. Soper, *Parton showers with quantum interference: Leading color, spin averaged*, *JHEP* **03** (2008) 030, arXiv: [0801.1917 \[hep-ph\]](#).
- [235] A. Buckley et al., *General-purpose event generators for LHC physics*, *Phys. Rept.* **504** (2011) 145, arXiv: [1101.2599 \[hep-ph\]](#).
- [236] ATLAS Collaboration, *Measurements of observables sensitive to colour reconnection in $t\bar{t}$ events with the ATLAS detector at $\sqrt{s} = 13$ TeV*, *Eur. Phys. J. C* **83** (2023) 518, arXiv: [2209.07874 \[hep-ex\]](#).
- [237] ATLAS Collaboration, *Performance of top-quark and W-boson tagging with ATLAS in Run 2 of the LHC*, *Eur. Phys. J. C* **79** (2019) 375, arXiv: [1808.07858 \[hep-ex\]](#).
- [238] CMS Collaboration, *Identification of heavy, energetic, hadronically decaying particles using machine-learning techniques*, *JINST* **15** (2020) P06005, arXiv: [2004.08262 \[hep-ex\]](#).
- [239] A. Butter et al., *The Machine Learning landscape of top taggers*, *SciPost Phys.* **7** (2019) 014, ed. by G. Kasieczka and T. Plehn, arXiv: [1902.09914 \[hep-ph\]](#).
- [240] ATLAS Collaboration, *Measurement of jet substructure in boosted $t\bar{t}$ events with the ATLAS detector using 140 fb^{-1} of 13 TeV pp collisions*, (2023), arXiv: [2312.03797 \[hep-ex\]](#).
- [241] S. Schael et al., *Electroweak Measurements in Electron-Positron Collisions at W-Boson-Pair Energies at LEP*, *Phys. Rept.* **532** (2013) 119, arXiv: [1302.3415 \[hep-ex\]](#).
- [242] ATLAS Collaboration, *Test of the universality of τ and μ lepton couplings in W-boson decays with the ATLAS detector*, *Nature Phys.* **17** (2021) 813, arXiv: [2007.14040 \[hep-ex\]](#).
- [243] ATLAS Collaboration, *Precise test of lepton flavour universality in W-boson decays into muons and electrons in pp collisions at $\sqrt{s} = 13$ TeV with the ATLAS detector*, (2024), arXiv: [2403.02133 \[hep-ex\]](#).
- [244] ALEPH, DELPHI, L3, OPAL and SLD Collaborations, LEP Electroweak Working Group, SLD Electroweak Group, SLD Heavy Flavour Group, *Precision electroweak measurements on the Z resonance*, *Phys. Rept.* **427** (2006) 257, arXiv: [hep-ex/0509008](#).
- [245] S. L. Glashow, J. Iliopoulos and L. Maiani, *Weak Interactions with Lepton-Hadron Symmetry*, *Phys. Rev. D* **2** (1970) 1285.
- [246] J. A. Aguilar-Saavedra, *Top flavor-changing neutral interactions: Theoretical expectations and experimental detection*, *Acta Phys. Polon. B* **35** (2004) 2695, ed. by F. del Aguila, R. Pittau, A. Djouadi and C. G. Papadopoulos, arXiv: [hep-ph/0409342](#).
- [247] J. A. Aguilar-Saavedra, *Effects of mixing with quark singlets*, *Phys. Rev. D* **67** (2003) 035003, arXiv: [hep-ph/0210112](#), Erratum: *Phys. Rev. D* **69** (2004) 099901.
- [248] D. Atwood, L. Reina and A. Soni, *Phenomenology of two Higgs doublet models with flavor-changing neutral currents*, *Phys. Rev. D* **55** (1997) 3156, arXiv: [hep-ph/9609279](#).

- [249] J. J. Cao et al., *Supersymmetry-induced flavor-changing neutral-current top-quark processes at the CERN Large Hadron Collider*, *Phys. Rev. D* **75** (2007) 075021, arXiv: [hep-ph/0702264](#).
- [250] J. M. Yang, B.-L. Young and X. Zhang, *Flavor-changing top quark decays in R-parity-violating supersymmetric models*, *Phys. Rev. D* **58** (1998) 055001, arXiv: [hep-ph/9705341](#).
- [251] K. Agashe, G. Perez and A. Soni, *Collider Signals of Top Quark Flavor Violation from a Warped Extra Dimension*, *Phys. Rev. D* **75** (2007) 015002, arXiv: [hep-ph/0606293](#).
- [252] P. Q. Hung, Y.-X. Lin, C. S. Nugroho and T.-C. Yuan, *Top Quark Rare Decays via Loop-Induced FCNC Interactions in Extended Mirror Fermion Model*, *Nucl. Phys. B* **927** (2018) 166, arXiv: [1709.01690](#) [[hep-ph](#)].
- [253] G. Durieux, F. Maltoni and C. Zhang, *Global approach to top-quark flavor-changing interactions*, *Phys. Rev. D* **91** (2015) 074017, arXiv: [1412.7166](#) [[hep-ph](#)].
- [254] ATLAS Collaboration, *Search for top quark decays $t \rightarrow qH$, with $H \rightarrow \gamma\gamma$, in $\sqrt{s} = 13$ TeV pp collisions using the ATLAS detector*, *JHEP* **10** (2017) 129, arXiv: [1707.01404](#) [[hep-ex](#)].
- [255] ATLAS Collaboration, *Search for flavor-changing neutral currents in top quark decays $t \rightarrow Hc$ and $t \rightarrow Hu$ in multilepton final states in proton–proton collisions at $\sqrt{s} = 13$ TeV with the ATLAS detector*, *Phys. Rev. D* **98** (2018) 032002, arXiv: [1805.03483](#) [[hep-ex](#)].
- [256] ATLAS Collaboration, *Search for top-quark decays $t \rightarrow Hq$ with 36fb^{-1} of pp collision data at $\sqrt{s} = 13$ TeV with the ATLAS detector*, *JHEP* **05** (2019) 123, arXiv: [1812.11568](#) [[hep-ex](#)].
- [257] ATLAS Collaboration, *Search for flavor-changing neutral tqH interactions with $H \rightarrow \gamma\gamma$ in pp collisions at $\sqrt{s} = 13$ TeV using the ATLAS detector*, *JHEP* **12** (2023) 195, arXiv: [2309.12817](#) [[hep-ex](#)].
- [258] ATLAS Collaboration, *Search for flavour-changing neutral-current couplings between the top quark and the Higgs boson in multi-lepton final states in 13 TeV pp collisions with the ATLAS detector*, (2024), arXiv: [2404.02123](#) [[hep-ex](#)].
- [259] ATLAS Collaboration, *Search for flavour-changing neutral current interactions of the top quark and the Higgs boson in events with a pair of τ -leptons in pp collisions at $\sqrt{s} = 13$ TeV with the ATLAS detector*, *JHEP* **06** (2023) 155, arXiv: [2208.11415](#) [[hep-ex](#)].
- [260] ATLAS Collaboration, *Search for a new scalar resonance in flavour-changing neutral-current top-quark decays $t \rightarrow qX$ ($q = u, c$), with $X \rightarrow b\bar{b}$, in proton–proton collisions at $\sqrt{s} = 13$ TeV with the ATLAS detector*, *JHEP* **07** (2023) 199, arXiv: [2301.03902](#) [[hep-ex](#)].
- [261] ATLAS Collaboration, *Evidence for the associated production of the Higgs boson and a top quark pair with the ATLAS detector*, *Phys. Rev. D* **97** (2018) 072003, arXiv: [1712.08891](#) [[hep-ex](#)].
- [262] ATLAS Collaboration, *Search for the Standard Model Higgs boson produced in association with top quarks and decaying into $b\bar{b}$ in pp collisions at $\sqrt{s} = 8$ TeV with the ATLAS detector*, *Eur. Phys. J. C* **75** (2015) 349, arXiv: [1503.05066](#) [[hep-ex](#)].
- [263] ATLAS Collaboration, *Search for the standard model Higgs boson produced in association with top quarks and decaying into a $b\bar{b}$ pair in pp collisions at $\sqrt{s} = 13$ TeV with the ATLAS detector*, *Phys. Rev. D* **97** (2018) 072016, arXiv: [1712.08895](#) [[hep-ex](#)].

- [264] ATLAS Collaboration, *Search for flavour-changing neutral-current interactions of a top quark and a gluon in pp collisions at $\sqrt{s} = 13$ TeV with the ATLAS detector*, *Eur. Phys. J. C* **82** (2022) 334, arXiv: [2112.01302 \[hep-ex\]](#).
- [265] ATLAS Collaboration, *Search for flavour-changing neutral currents in processes with one top quark and a photon using 81fb^{-1} of pp collisions at $\sqrt{s} = 13$ TeV with the ATLAS experiment*, *Phys. Lett. B* **800** (2020) 135082, arXiv: [1908.08461 \[hep-ex\]](#).
- [266] ATLAS Collaboration, *Search for flavour-changing neutral-current couplings between the top quark and the photon with the ATLAS detector at $\sqrt{s} = 13$ TeV*, *Phys. Lett. B* **842** (2023) 137379, arXiv: [2205.02537 \[hep-ex\]](#).
- [267] B. Grzadkowski, M. Iskrzyński, M. Misiak and J. Rosiek, *Dimension-Six Terms in the Standard Model Lagrangian*, *JHEP* **10** (2010) 085, arXiv: [1008.4884 \[hep-ph\]](#).
- [268] D. Barducci et al., *Interpreting top-quark LHC measurements in the standard-model effective field theory*, (2018), ed. by J. A. Aguilar-Saavedra et al., arXiv: [1802.07237 \[hep-ph\]](#).
- [269] ATLAS Collaboration, *Search for flavour-changing neutral current top-quark decays $t \rightarrow qZ$ in proton–proton collisions at $\sqrt{s} = 13$ TeV with the ATLAS detector*, *JHEP* **07** (2018) 176, arXiv: [1803.09923 \[hep-ex\]](#).
- [270] ATLAS Collaboration, *Search for flavor-changing neutral-current couplings between the top quark and the Z boson with proton–proton collisions at $\sqrt{s} = 13$ TeV with the ATLAS detector*, *Phys. Rev. D* **108** (2023) 032019, arXiv: [2301.11605 \[hep-ex\]](#).
- [271] ATLAS Collaboration, *ATLAS Computing Acknowledgements*, ATL-SOFT-PUB-2023-001, 2023, URL: <https://cds.cern.ch/record/2869272>.

The ATLAS Collaboration

G. Aad ¹⁰³, E. Aakvaag ¹⁶, B. Abbott ¹²¹, S. Abdelhameed ^{117a}, K. Abeling ⁵⁵, N.J. Abicht ⁴⁹, S.H. Abidi ²⁹, M. Aboeela ⁴⁴, A. Aboulhorma ^{35e}, H. Abramowicz ¹⁵², H. Abreu ¹⁵¹, Y. Abulaiti ¹¹⁸, B.S. Acharya ^{69a,69b,k}, A. Ackermann ^{63a}, C. Adam Bourdarios ⁴, L. Adamczyk ^{86a}, S.V. Addepalli ²⁶, M.J. Addison ¹⁰², J. Adelman ¹¹⁶, A. Adiguzel ^{21c}, T. Adye ¹³⁵, A.A. Affolder ¹³⁷, Y. Afik ³⁹, M.N. Agaras ¹³, J. Agarwala ^{73a,73b}, A. Aggarwal ¹⁰¹, C. Agheorghiesei ^{27c}, A. Ahmad ³⁶, F. Ahmadov ^{38,x}, W.S. Ahmed ¹⁰⁵, S. Ahuja ⁹⁶, X. Ai ^{62e}, G. Aielli ^{76a,76b}, A. Aikot ¹⁶⁴, M. Ait Tamliah ^{35e}, B. Aitbenkhik ^{35a}, M. Akbiyik ¹⁰¹, T.P.A. Åkesson ⁹⁹, A.V. Akimov ³⁷, D. Akiyama ¹⁶⁹, N.N. Akolkar ²⁴, S. Aktas ^{21a}, K. Al Houry ⁴¹, G.L. Alberghi ^{23b}, J. Albert ¹⁶⁶, P. Albicocco ⁵³, G.L. Albouy ⁶⁰, S. Alderweireldt ⁵², Z.L. Alegria ¹²², M. Aleksa ³⁶, I.N. Aleksandrov ³⁸, C. Alexa ^{27b}, T. Alexopoulos ¹⁰, F. Alfonsi ^{23b}, M. Algren ⁵⁶, M. Alhroob ¹⁴², B. Ali ¹³³, H.M.J. Ali ⁹², S. Ali ³¹, S.W. Alibocus ⁹³, M. Aliev ^{33c}, G. Alimonti ^{71a}, W. Alkahi ⁵⁵, C. Allaire ⁶⁶, B.M.M. Allbrooke ¹⁴⁷, J.F. Allen ⁵², C.A. Allendes Flores ^{138f}, P.P. Allport ²⁰, A. Aloisio ^{72a,72b}, F. Alonso ⁹¹, C. Alpigiani ¹³⁹, Z.M.K. Alsolami ⁹², M. Alvarez Estevez ¹⁰⁰, A. Alvarez Fernandez ¹⁰¹, M. Alves Cardoso ⁵⁶, M.G. Alvigi ^{72a,72b}, M. Aly ¹⁰², Y. Amaral Coutinho ^{83b}, A. Ambler ¹⁰⁵, C. Amelung ³⁶, M. Amerl ¹⁰², C.G. Ames ¹¹⁰, D. Amidei ¹⁰⁷, K.J. Amirie ¹⁵⁶, S.P. Amor Dos Santos ^{131a}, K.R. Amos ¹⁶⁴, S. An ⁸⁴, V. Ananiev ¹²⁶, C. Anastopoulos ¹⁴⁰, T. Andeen ¹¹, J.K. Anders ³⁶, S.Y. Andreato ^{47a,47b}, A. Andreazza ^{71a,71b}, S. Angelidakis ⁹, A. Angerami ^{41,z}, A.V. Anisenkov ³⁷, A. Annovi ^{74a}, C. Antel ⁵⁶, E. Antipov ¹⁴⁶, M. Antonelli ⁵³, F. Anulli ^{75a}, M. Aoki ⁸⁴, T. Aoki ¹⁵⁴, M.A. Aparo ¹⁴⁷, L. Aperio Bella ⁴⁸, C. Appelt ¹⁸, A. Apyan ²⁶, S.J. Arbiol Val ⁸⁷, C. Arcangeletti ⁵³, A.T.H. Arce ⁵¹, E. Arena ⁹³, J-F. Arguin ¹⁰⁹, S. Argyropoulos ⁵⁴, J.-H. Arling ⁴⁸, O. Arnaez ⁴, H. Arnold ¹¹⁵, G. Artoni ^{75a,75b}, H. Asada ¹¹², K. Asai ¹¹⁹, S. Asai ¹⁵⁴, N.A. Asbah ³⁶, K. Assamagan ²⁹, R. Astalos ^{28a}, K.S.V. Astrand ⁹⁹, S. Atashi ¹⁶⁰, R.J. Atkin ^{33a}, M. Atkinson ¹⁶³, H. Atmani ^{35f}, P.A. Atlasiddha ¹²⁹, K. Augsten ¹³³, S. Auricchio ^{72a,72b}, A.D. Auriol ²⁰, V.A. Austrup ¹⁰², G. Avolio ³⁶, K. Axiotis ⁵⁶, G. Azuelos ^{109,ad}, D. Babal ^{28b}, H. Bachacou ¹³⁶, K. Bachas ^{153,o}, A. Bachi ³⁴, F. Backman ^{47a,47b}, A. Badea ³⁹, T.M. Baer ¹⁰⁷, P. Bagnaia ^{75a,75b}, M. Bahmani ¹⁸, D. Bahner ⁵⁴, K. Bai ¹²⁴, J.T. Baines ¹³⁵, L. Baines ⁹⁵, O.K. Baker ¹⁷³, E. Bakos ¹⁵, D. Bakshi Gupta ⁸, V. Balakrishnan ¹²¹, R. Balasubramanian ¹¹⁵, E.M. Baldin ³⁷, P. Balek ^{86a}, E. Ballabene ^{23b,23a}, F. Balli ¹³⁶, L.M. Baltos ^{63a}, W.K. Balunas ³², J. Balz ¹⁰¹, I. Bamwidhi ^{117b}, E. Banas ⁸⁷, M. Bandieramonte ¹³⁰, A. Bandyopadhyay ²⁴, S. Bansal ²⁴, L. Barak ¹⁵², M. Barakat ⁴⁸, E.L. Barberio ¹⁰⁶, D. Barberis ^{57b,57a}, M. Barbero ¹⁰³, M.Z. Barel ¹¹⁵, K.N. Barends ^{33a}, T. Barillari ¹¹¹, M-S. Barisits ³⁶, T. Barklow ¹⁴⁴, P. Baron ¹²³, D.A. Baron Moreno ¹⁰², A. Baroncelli ^{62a}, G. Barone ²⁹, A.J. Barr ¹²⁷, J.D. Barr ⁹⁷, F. Barreiro ¹⁰⁰, J. Barreiro Guimarães da Costa ^{14a}, U. Barron ¹⁵², M.G. Barros Teixeira ^{131a}, S. Barsov ³⁷, F. Bartels ^{63a}, R. Bartoldus ¹⁴⁴, A.E. Barton ⁹², P. Bartos ^{28a}, A. Basan ¹⁰¹, M. Baselga ⁴⁹, A. Bassalat ^{66,b}, M.J. Basso ^{157a}, R. Bate ¹⁶⁵, R.L. Bates ⁵⁹, S. Batlamous ¹⁰⁰, B. Batool ¹⁴², M. Battaglia ¹³⁷, D. Battulga ¹⁸, M. Baucé ^{75a,75b}, M. Bauer ³⁶, P. Bauer ²⁴, L.T. Bazzano Hurrell ³⁰, J.B. Beacham ⁵¹, T. Beau ¹²⁸, J.Y. Beaucamp ⁹¹, P.H. Beauchemin ¹⁵⁹, P. Bechtel ²⁴, H.P. Beck ^{19,n}, K. Becker ¹⁶⁸, A.J. Beddall ⁸², V.A. Bednyakov ³⁸, C.P. Bee ¹⁴⁶, L.J. Beemster ¹⁵, T.A. Beermann ³⁶, M. Begalli ^{83d}, M. Begel ²⁹, A. Behera ¹⁴⁶, J.K. Behr ⁴⁸, J.F. Beirer ³⁶, F. Beisiegel ²⁴, M. Belfkir ^{117b}, G. Bella ¹⁵², L. Bellagamba ^{23b}, A. Bellerive ³⁴, P. Bellos ²⁰, K. Beloborodov ³⁷, D. Bencheikroun ^{35a}, F. Bendebba ^{35a}, Y. Benhammou ¹⁵²,

K.C. Benkendorfer ⁶¹, L. Beresford ⁴⁸, M. Beretta ⁵³, E. Bergeaas Kuutmann ¹⁶², N. Berger ⁴,
 B. Bergmann ¹³³, J. Beringer ^{17a}, G. Bernardi ⁵, C. Bernius ¹⁴⁴, F.U. Bernlochner ²⁴,
 F. Bernon ^{36,103}, A. Berrocal Guardia ¹³, T. Berry ⁹⁶, P. Berta ¹³⁴, A. Berthold ⁵⁰, S. Bethke ¹¹¹,
 A. Betti ^{75a,75b}, A.J. Bevan ⁹⁵, N.K. Bhalla ⁵⁴, M. Bhamjee ^{33c}, S. Bhatta ¹⁴⁶,
 D.S. Bhattacharya ¹⁶⁷, P. Bhattarai ¹⁴⁴, K.D. Bhide ⁵⁴, V.S. Bhopatkar ¹²², R.M. Bianchi ¹³⁰,
 G. Bianco ^{23b,23a}, O. Biebel ¹¹⁰, R. Bielski ¹²⁴, M. Biglietti ^{77a}, C.S. Billingsley ⁴⁴, M. Bindi ⁵⁵,
 A. Bingul ^{21b}, C. Bini ^{75a,75b}, A. Biondini ⁹³, C.J. Birch-sykes ¹⁰², G.A. Bird ³², M. Birman ¹⁷⁰,
 M. Biros ¹³⁴, S. Biryukov ¹⁴⁷, T. Bisanz ⁴⁹, E. Bisceglie ^{43b,43a}, J.P. Biswal ¹³⁵, D. Biswas ¹⁴²,
 I. Bloch ⁴⁸, A. Blue ⁵⁹, U. Blumenschein ⁹⁵, J. Blumenthal ¹⁰¹, V.S. Bobrovnikov ³⁷,
 M. Boehler ⁵⁴, B. Boehm ¹⁶⁷, D. Bogavac ³⁶, A.G. Bogdanchikov ³⁷, C. Bohm ^{47a},
 V. Boisvert ⁹⁶, P. Bokan ³⁶, T. Bold ^{86a}, M. Bomben ⁵, M. Bona ⁹⁵, M. Boonekamp ¹³⁶,
 C.D. Booth ⁹⁶, A.G. Borbély ⁵⁹, I.S. Bordulev ³⁷, H.M. Borecka-Bielska ¹⁰⁹, G. Borissov ⁹²,
 D. Bortoletto ¹²⁷, D. Boscherini ^{23b}, M. Bosman ¹³, J.D. Bossio Sola ³⁶, K. Bouaouda ^{35a},
 N. Bouchhar ¹⁶⁴, L. Boudet ⁴, J. Boudreau ¹³⁰, E.V. Bouhova-Thacker ⁹², D. Boumediene ⁴⁰,
 R. Bouquet ^{57b,57a}, A. Boveia ¹²⁰, J. Boyd ³⁶, D. Boye ²⁹, I.R. Boyko ³⁸, L. Bozianu ⁵⁶,
 J. Bracinik ²⁰, N. Brahimi ⁴, G. Brandt ¹⁷², O. Brandt ³², F. Braren ⁴⁸, B. Brau ¹⁰⁴,
 J.E. Brau ¹²⁴, R. Brenner ¹⁷⁰, L. Brenner ¹¹⁵, R. Brenner ¹⁶², S. Bressler ¹⁷⁰, D. Britton ⁵⁹,
 D. Britzger ¹¹¹, I. Brock ²⁴, G. Brooijmans ⁴¹, E. Brost ²⁹, L.M. Brown ¹⁶⁶, L.E. Bruce ⁶¹,
 T.L. Bruckler ¹²⁷, P.A. Bruckman de Renstrom ⁸⁷, B. Brüers ⁴⁸, A. Bruni ^{23b}, G. Bruni ^{23b},
 M. Bruschi ^{23b}, N. Bruscinò ^{75a,75b}, T. Buanes ¹⁶, Q. Buat ¹³⁹, D. Buchin ¹¹¹, A.G. Buckley ⁵⁹,
 O. Bulekov ³⁷, B.A. Bullard ¹⁴⁴, S. Burdin ⁹³, C.D. Burgard ⁴⁹, A.M. Burger ³⁶,
 B. Burghgrave ⁸, O. Burlayenko ⁵⁴, J.T.P. Burr ³², J.C. Burzynski ¹⁴³, E.L. Busch ⁴¹,
 V. Büscher ¹⁰¹, P.J. Bussey ⁵⁹, J.M. Butler ²⁵, C.M. Buttar ⁵⁹, J.M. Butterworth ⁹⁷,
 W. Buttinger ¹³⁵, C.J. Buxo Vazquez ¹⁰⁸, A.R. Buzykaev ³⁷, S. Cabrera Urbán ¹⁶⁴,
 L. Cadamuro ⁶⁶, D. Caforio ⁵⁸, H. Cai ¹³⁰, Y. Cai ^{14a,14e}, Y. Cai ^{14c}, V.M.M. Cairo ³⁶,
 O. Cakir ^{3a}, N. Calace ³⁶, P. Calafiura ^{17a}, G. Calderini ¹²⁸, P. Calfayan ⁶⁸, G. Callea ⁵⁹,
 L.P. Caloba ^{83b}, D. Calvet ⁴⁰, S. Calvet ⁴⁰, M. Calvetti ^{74a,74b}, R. Camacho Toro ¹²⁸,
 S. Camarda ³⁶, D. Camarero Munoz ²⁶, P. Camarri ^{76a,76b}, M.T. Camerlingo ^{72a,72b},
 D. Cameron ³⁶, C. Camincher ¹⁶⁶, M. Campanelli ⁹⁷, A. Camplani ⁴², V. Canale ^{72a,72b},
 A.C. Canbay ^{3a}, E. Canonero ⁹⁶, J. Cantero ¹⁶⁴, Y. Cao ¹⁶³, F. Capocasa ²⁶, M. Capua ^{43b,43a},
 A. Carbone ^{71a,71b}, R. Cardarelli ^{76a}, J.C.J. Cardenas ⁸, G. Carducci ^{43b,43a}, T. Carli ³⁶,
 G. Carlino ^{72a}, J.I. Carlotto ¹³, B.T. Carlson ^{130,p}, E.M. Carlson ^{166,157a}, J. Carmignani ⁹³,
 L. Carminati ^{71a,71b}, A. Carnelli ¹³⁶, M. Carnesale ^{75a,75b}, S. Caron ¹¹⁴, E. Carquin ^{138f},
 S. Carrá ^{71a}, G. Carratta ^{23b,23a}, A.M. Carroll ¹²⁴, T.M. Carter ⁵², M.P. Casado ^{13,h},
 M. Caspar ⁴⁸, F.L. Castillo ⁴, L. Castillo Garcia ¹³, V. Castillo Gimenez ¹⁶⁴, N.F. Castro ^{131a,131e},
 A. Catinaccio ³⁶, J.R. Catmore ¹²⁶, T. Cavaliere ⁴, V. Cavaliere ²⁹, N. Cavalli ^{23b,23a},
 Y.C. Cekmecelioglu ⁴⁸, E. Celebi ^{21a}, S. Cella ³⁶, F. Celli ¹²⁷, M.S. Centonze ^{70a,70b},
 V. Cepaitis ⁵⁶, K. Cerny ¹²³, A.S. Cerqueira ^{83a}, A. Cerri ¹⁴⁷, L. Cerrito ^{76a,76b}, F. Cerutti ^{17a},
 B. Cervato ¹⁴², A. Cervelli ^{23b}, G. Cesarini ⁵³, S.A. Cetin ⁸², D. Chakraborty ¹¹⁶, J. Chan ^{17a},
 W.Y. Chan ¹⁵⁴, J.D. Chapman ³², E. Chapon ¹³⁶, B. Chargeishvili ^{150b}, D.G. Charlton ²⁰,
 M. Chatterjee ¹⁹, C. Chauhan ¹³⁴, Y. Che ^{14c}, S. Chekanov ⁶, S.V. Chekulaev ^{157a},
 G.A. Chelkov ^{38,a}, A. Chen ¹⁰⁷, B. Chen ¹⁵², B. Chen ¹⁶⁶, H. Chen ^{14c}, H. Chen ²⁹,
 J. Chen ^{62c}, J. Chen ¹⁴³, M. Chen ¹²⁷, S. Chen ¹⁵⁴, S.J. Chen ^{14c}, X. Chen ^{62c,136},
 X. Chen ^{14b,ac}, Y. Chen ^{62a}, C.L. Cheng ¹⁷¹, H.C. Cheng ^{64a}, S. Cheong ¹⁴⁴, A. Cheplakov ³⁸,
 E. Cheremushkina ⁴⁸, E. Cherepanova ¹¹⁵, R. Cherkaoui El Moursli ^{35e}, E. Cheu ⁷, K. Cheung ⁶⁵,
 L. Chevalier ¹³⁶, V. Chiarella ⁵³, G. Chiarelli ^{74a}, N. Chiedde ¹⁰³, G. Chiodini ^{70a},
 A.S. Chisholm ²⁰, A. Chitan ^{27b}, M. Chitishvili ¹⁶⁴, M.V. Chizhov ³⁸, K. Choi ¹¹, Y. Chou ¹³⁹,

E.Y.S. Chow ¹¹⁴, K.L. Chu ¹⁷⁰, M.C. Chu ^{64a}, X. Chu ^{14a,14e}, J. Chudoba ¹³²,
 J.J. Chwastowski ⁸⁷, D. Cieri ¹¹¹, K.M. Ciesla ^{86a}, V. Cindro ⁹⁴, A. Ciocio ^{17a}, F. Ciroto ^{72a,72b},
 Z.H. Citron ¹⁷⁰, M. Citterio ^{71a}, D.A. Ciubotaru ^{27b}, A. Clark ⁵⁶, P.J. Clark ⁵², C. Clarry ¹⁵⁶,
 J.M. Clavijo Columbie ⁴⁸, S.E. Clawson ⁴⁸, C. Clement ^{47a,47b}, J. Clercx ⁴⁸, Y. Coadou ¹⁰³,
 M. Cobal ^{69a,69c}, A. Coccaro ^{57b}, R.F. Coelho Barrue ^{131a}, R. Coelho Lopes De Sa ¹⁰⁴,
 S. Coelli ^{71a}, B. Cole ⁴¹, J. Collot ⁶⁰, P. Conde Muiño ^{131a,131g}, M.P. Connell ^{33c},
 S.H. Connell ^{33c}, E.I. Conroy ¹²⁷, F. Conventi ^{72a,ae}, H.G. Cooke ²⁰, A.M. Cooper-Sarkar ¹²⁷,
 F.A. Corchia ^{23b,23a}, A. Cordeiro Oudot Choi ¹²⁸, L.D. Corpe ⁴⁰, M. Corradi ^{75a,75b},
 F. Corriveau ^{105,v}, A. Cortes-Gonzalez ¹⁸, M.J. Costa ¹⁶⁴, F. Costanza ⁴, D. Costanzo ¹⁴⁰,
 B.M. Cote ¹²⁰, J. Couthures ⁴, G. Cowan ⁹⁶, K. Cranmer ¹⁷¹, D. Cremonini ^{23b,23a},
 S. Crépe-Renaudin ⁶⁰, F. Crescioli ¹²⁸, M. Cristinziani ¹⁴², M. Cristoforetti ^{78a,78b}, V. Croft ¹¹⁵,
 J.E. Crosby ¹²², G. Crosetti ^{43b,43a}, A. Cueto ¹⁰⁰, Z. Cui ⁷, W.R. Cunningham ⁵⁹, F. Curcio ¹⁶⁴,
 J.R. Curran ⁵², P. Czodrowski ³⁶, M.M. Czurylo ³⁶, M.J. Da Cunha Sargedas De Sousa ^{57b,57a},
 J.V. Da Fonseca Pinto ^{83b}, C. Da Via ¹⁰², W. Dabrowski ^{86a}, T. Dado ⁴⁹, S. Dahbi ¹⁴⁹,
 T. Dai ¹⁰⁷, D. Dal Santo ¹⁹, C. Dallapiccola ¹⁰⁴, M. Dam ⁴², G. D'amen ²⁹, V. D'Amico ¹¹⁰,
 J. Damp ¹⁰¹, J.R. Dandoy ³⁴, D. Dannheim ³⁶, M. Danninger ¹⁴³, V. Dao ³⁶, G. Darbo ^{57b},
 S.J. Das ^{29,af}, F. Dattola ⁴⁸, S. D'Auria ^{71a,71b}, A. D'avanzo ^{72a,72b}, C. David ^{33a}, T. Davidek ¹³⁴,
 I. Dawson ⁹⁵, H.A. Day-hall ¹³³, K. De ⁸, R. De Asmundis ^{72a}, N. De Biase ⁴⁸,
 S. De Castro ^{23b,23a}, N. De Groot ¹¹⁴, P. de Jong ¹¹⁵, H. De la Torre ¹¹⁶, A. De Maria ^{14c},
 A. De Salvo ^{75a}, U. De Sanctis ^{76a,76b}, F. De Santis ^{70a,70b}, A. De Santo ¹⁴⁷,
 J.B. De Vivie De Regie ⁶⁰, D.V. Dedovich ³⁸, J. Degen ⁹³, A.M. Deiana ⁴⁴, F. Del Corso ^{23b,23a},
 J. Del Peso ¹⁰⁰, F. Del Rio ^{63a}, L. Delagrangue ¹²⁸, F. Deliot ¹³⁶, C.M. Delitzsch ⁴⁹,
 M. Della Pietra ^{72a,72b}, D. Della Volpe ⁵⁶, A. Dell'Acqua ³⁶, L. Dell'Asta ^{71a,71b}, M. Delmastro ⁴,
 P.A. Delsart ⁶⁰, S. Demers ¹⁷³, M. Demichev ³⁸, S.P. Denisov ³⁷, L. D'Eramo ⁴⁰,
 D. Derendarz ⁸⁷, F. Derue ¹²⁸, P. Dervan ⁹³, K. Desch ²⁴, C. Deutsch ²⁴, F.A. Di Bello ^{57b,57a},
 A. Di Ciaccio ^{76a,76b}, L. Di Ciaccio ⁴, A. Di Domenico ^{75a,75b}, C. Di Donato ^{72a,72b},
 A. Di Girolamo ³⁶, G. Di Gregorio ³⁶, A. Di Luca ^{78a,78b}, B. Di Micco ^{77a,77b}, R. Di Nardo ^{77a,77b},
 M. Diamantopoulou ³⁴, F.A. Dias ¹¹⁵, T. Dias Do Vale ¹⁴³, M.A. Diaz ^{138a,138b},
 F.G. Diaz Capriles ²⁴, M. Didenko ¹⁶⁴, E.B. Diehl ¹⁰⁷, S. Díez Cornell ⁴⁸, C. Diez Pardos ¹⁴²,
 C. Dimitriadi ^{162,24}, A. Dimitrievska ²⁰, J. Dingfelder ²⁴, I-M. Dinu ^{27b}, S.J. Dittmeier ^{63b},
 F. Dittus ³⁶, M. Divisek ¹³⁴, F. Djama ¹⁰³, T. Djobava ^{150b}, C. Doglioni ^{102,99},
 A. Dohnalova ^{28a}, J. Dolejsi ¹³⁴, Z. Dolezal ¹³⁴, K. Domijan ^{86a}, K.M. Dona ³⁹,
 M. Donadelli ^{83c}, B. Dong ¹⁰⁸, J. Donini ⁴⁰, A. D'Onofrio ^{72a,72b}, M. D'Onofrio ⁹³,
 J. Dopke ¹³⁵, A. Doria ^{72a}, N. Dos Santos Fernandes ^{131a}, P. Dougan ¹⁰², M.T. Dova ⁹¹,
 A.T. Doyle ⁵⁹, M.A. Dragnet ¹²⁷, E. Dreyer ¹⁷⁰, I. Drivas-koulouris ¹⁰, M. Drnevich ¹¹⁸,
 M. Drozdova ⁵⁶, D. Du ^{62a}, T.A. du Pree ¹¹⁵, F. Dubinin ³⁷, M. Dubovsky ^{28a}, E. Duchovni ¹⁷⁰,
 G. Duckeck ¹¹⁰, O.A. Ducu ^{27b}, D. Duda ⁵², A. Dudarev ³⁶, E.R. Duden ²⁶, M. D'uffizi ¹⁰²,
 L. Dufлот ⁶⁶, M. Dührssen ³⁶, I. Duminica ^{27g}, A.E. Dumitriu ^{27b}, M. Dunford ^{63a}, S. Dungs ⁴⁹,
 K. Dunne ^{47a,47b}, A. Duperrin ¹⁰³, H. Duran Yildiz ^{3a}, M. Düren ⁵⁸, A. Durglishvili ^{150b},
 B.L. Dwyer ¹¹⁶, G.I. Dyckes ^{17a}, M. Dyndal ^{86a}, B.S. Dziedzic ³⁶, Z.O. Earnshaw ¹⁴⁷,
 G.H. Eberwein ¹²⁷, B. Eckerova ^{28a}, S. Eggebrecht ⁵⁵, E. Egidio Purcino De Souza ¹²⁸,
 L.F. Ehrke ⁵⁶, G. Eigen ¹⁶, K. Einsweiler ^{17a}, T. Ekelof ¹⁶², P.A. Ekman ⁹⁹, S. El Farkh ^{35b},
 Y. El Ghazali ^{35b}, H. El Jarrari ³⁶, A. El Moussaouy ¹⁰⁹, V. Ellajosyula ¹⁶², M. Ellert ¹⁶²,
 F. Ellinghaus ¹⁷², N. Ellis ³⁶, J. Elmsheuser ²⁹, M. Elsayy ^{117a}, M. Elsing ³⁶,
 D. Emelianov ¹³⁵, Y. Enari ¹⁵⁴, I. Ene ^{17a}, S. Epari ¹³, P.A. Erland ⁸⁷, M. Errenst ¹⁷²,
 M. Escalier ⁶⁶, C. Escobar ¹⁶⁴, E. Etzion ¹⁵², G. Evans ^{131a}, H. Evans ⁶⁸, L.S. Evans ⁹⁶,
 A. Ezhilov ³⁷, S. Ezzarqtouni ^{35a}, F. Fabbri ^{23b,23a}, L. Fabbri ^{23b,23a}, G. Facini ⁹⁷,

V. Fadeyev ¹³⁷, R.M. Fakhruddinov ³⁷, D. Fakoudis ¹⁰¹, S. Falciano ^{75a},
L.F. Falda Ulhoa Coelho ³⁶, F. Fallavollita ¹¹¹, J. Faltova ¹³⁴, C. Fan ¹⁶³, Y. Fan ^{14a},
Y. Fang ^{14a,14e}, M. Fanti ^{71a,71b}, M. Faraj ^{69a,69b}, Z. Farazpay ⁹⁸, A. Farbin ⁸, A. Farilla ^{77a},
T. Farooque ¹⁰⁸, S.M. Farrington ⁵², F. Fassi ^{35e}, D. Fassouliotis ⁹, M. Fauci Giannelli ^{76a,76b},
W.J. Fawcett ³², L. Fayard ⁶⁶, P. Federic ¹³⁴, P. Federicova ¹³², O.L. Fedin ^{37,a}, M. Feickert ¹⁷¹,
L. Feligioni ¹⁰³, D.E. Fellers ¹²⁴, C. Feng ^{62b}, M. Feng ^{14b}, Z. Feng ¹¹⁵, M.J. Fenton ¹⁶⁰,
L. Ferencz ⁴⁸, R.A.M. Ferguson ⁹², S.I. Fernandez Luengo ^{138f}, P. Fernandez Martinez ¹³,
M.J.V. Fernoux ¹⁰³, J. Ferrando ⁹², A. Ferrari ¹⁶², P. Ferrari ^{115,114}, R. Ferrari ^{73a}, D. Ferrere ⁵⁶,
C. Ferretti ¹⁰⁷, F. Fiedler ¹⁰¹, P. Fiedler ¹³³, A. Filipčič ⁹⁴, E.K. Filmer ¹, F. Filthaut ¹¹⁴,
M.C.N. Fiolhais ^{131a,131c,c}, L. Fiorini ¹⁶⁴, W.C. Fisher ¹⁰⁸, T. Fitschen ¹⁰², P.M. Fitzhugh ¹³⁶,
I. Fleck ¹⁴², P. Fleischmann ¹⁰⁷, T. Flick ¹⁷², M. Flores ^{33d,aa}, L.R. Flores Castillo ^{64a},
L. Flores Sanz De Acedo ³⁶, F.M. Follega ^{78a,78b}, N. Fomin ¹⁶, J.H. Foo ¹⁵⁶, A. Formica ¹³⁶,
A.C. Forti ¹⁰², E. Fortin ³⁶, A.W. Fortman ^{17a}, M.G. Foti ^{17a}, L. Fountas ^{9,i}, D. Fournier ⁶⁶,
H. Fox ⁹², P. Francavilla ^{74a,74b}, S. Francescato ⁶¹, S. Franchellucci ⁵⁶, M. Franchini ^{23b,23a},
S. Franchino ^{63a}, D. Francis ³⁶, L. Franco ¹¹⁴, V. Franco Lima ³⁶, L. Franconi ⁴⁸, M. Franklin ⁶¹,
G. Frattari ²⁶, Y.Y. Frid ¹⁵², J. Friend ⁵⁹, N. Fritzsche ⁵⁰, A. Froch ⁵⁴, D. Froidevaux ³⁶,
J.A. Frost ¹²⁷, Y. Fu ^{62a}, S. Fuenzalida Garrido ^{138f}, M. Fujimoto ¹⁰³, K.Y. Fung ^{64a},
E. Furtado De Simas Filho ^{83e}, M. Furukawa ¹⁵⁴, J. Fuster ¹⁶⁴, A. Gabrielli ^{23b,23a},
A. Gabrielli ¹⁵⁶, P. Gadow ³⁶, G. Gagliardi ^{57b,57a}, L.G. Gagnon ^{17a}, S. Gaid ¹⁶¹,
S. Galantzan ¹⁵², E.J. Gallas ¹²⁷, B.J. Gallop ¹³⁵, K.K. Gan ¹²⁰, S. Ganguly ¹⁵⁴, Y. Gao ⁵²,
F.M. Garay Walls ^{138a,138b}, B. Garcia ²⁹, C. García ¹⁶⁴, A. Garcia Alonso ¹¹⁵,
A.G. Garcia Caffaro ¹⁷³, J.E. García Navarro ¹⁶⁴, M. Garcia-Sciveres ^{17a}, G.L. Gardner ¹²⁹,
R.W. Gardner ³⁹, N. Garelli ¹⁵⁹, D. Garg ⁸⁰, R.B. Garg ¹⁴⁴, J.M. Gargan ⁵², C.A. Garner ¹⁵⁶,
C.M. Garvey ^{33a}, V.K. Gassmann ¹⁵⁹, G. Gaudio ^{73a}, V. Gautam ¹³, P. Gauzzi ^{75a,75b},
I.L. Gavrilenko ³⁷, A. Gavrilyuk ³⁷, C. Gay ¹⁶⁵, G. Gaycken ⁴⁸, E.N. Gazis ¹⁰, A.A. Geanta ^{27b},
C.M. Gee ¹³⁷, A. Gekow ¹²⁰, C. Gemme ^{57b}, M.H. Genest ⁶⁰, A.D. Gentry ¹¹³, S. George ⁹⁶,
W.F. George ²⁰, T. Gerialis ⁴⁶, P. Gessinger-Befurt ³⁶, M.E. Geyik ¹⁷², M. Ghani ¹⁶⁸,
K. Ghorbanian ⁹⁵, A. Ghosal ¹⁴², A. Ghosh ¹⁶⁰, A. Ghosh ⁷, B. Giacobbe ^{23b}, S. Giagu ^{75a,75b},
T. Giani ¹¹⁵, P. Giannetti ^{74a}, A. Giannini ^{62a}, S.M. Gibson ⁹⁶, M. Gignac ¹³⁷, D.T. Gil ^{86b},
A.K. Gilbert ^{86a}, B.J. Gilbert ⁴¹, D. Gillberg ³⁴, G. Gilles ¹¹⁵, L. Ginabat ¹²⁸,
D.M. Gingrich ^{2,ad}, M.P. Giordani ^{69a,69c}, P.F. Giraud ¹³⁶, G. Giugliarelli ^{69a,69c}, D. Giugni ^{71a},
F. Giuli ³⁶, I. Gkialas ^{9,i}, L.K. Gladilin ³⁷, C. Glasman ¹⁰⁰, G.R. Gledhill ¹²⁴, G. Glemža ⁴⁸,
M. Glisic ¹²⁴, I. Gnesi ^{43b,e}, Y. Go ²⁹, M. Goblirsch-Kolb ³⁶, B. Gocke ⁴⁹, D. Godin ¹⁰⁹,
B. Gokturk ^{21a}, S. Goldfarb ¹⁰⁶, T. Golling ⁵⁶, M.G.D. Gololo ^{33g}, D. Golubkov ³⁷,
J.P. Gombas ¹⁰⁸, A. Gomes ^{131a,131b}, G. Gomes Da Silva ¹⁴², A.J. Gomez Delegido ¹⁶⁴,
R. Gonçalves ^{131a}, L. Gonella ²⁰, A. Gongadze ^{150c}, F. Gonnella ²⁰, J.L. Gonski ¹⁴⁴,
R.Y. González Andana ⁵², S. González de la Hoz ¹⁶⁴, R. Gonzalez Lopez ⁹³,
C. Gonzalez Renteria ^{17a}, M.V. Gonzalez Rodrigues ⁴⁸, R. Gonzalez Suarez ¹⁶²,
S. Gonzalez-Sevilla ⁵⁶, L. Goossens ³⁶, B. Gorini ³⁶, E. Gorini ^{70a,70b}, A. Gorišek ⁹⁴,
T.C. Gosart ¹²⁹, A.T. Goshaw ⁵¹, M.I. Gostkin ³⁸, S. Goswami ¹²², C.A. Gottardo ³⁶,
S.A. Gotz ¹¹⁰, M. Gouighri ^{35b}, V. Goumarre ⁴⁸, A.G. Goussiou ¹³⁹, N. Govender ^{33c},
I. Grabowska-Bold ^{86a}, K. Graham ³⁴, E. Gramstad ¹²⁶, S. Grancagnolo ^{70a,70b}, C.M. Grant ^{1,136},
P.M. Gravila ^{27f}, F.G. Gravili ^{70a,70b}, H.M. Gray ^{17a}, M. Greco ^{70a,70b}, C. Grefe ²⁴,
I.M. Gregor ⁴⁸, K.T. Greif ¹⁶⁰, P. Grenier ¹⁴⁴, S.G. Grewe ¹¹¹, A.A. Grillo ¹³⁷, K. Grimm ³¹,
S. Grinstein ^{13,r}, J.-F. Grivaz ⁶⁶, E. Gross ¹⁷⁰, J. Grosse-Knetter ⁵⁵, J.C. Grundy ¹²⁷,
L. Guan ¹⁰⁷, J.G.R. Guerrero Rojas ¹⁶⁴, G. Guerrieri ^{69a,69c}, F. Guescini ¹¹¹, R. Gugel ¹⁰¹,
J.A.M. Guhit ¹⁰⁷, A. Guida ¹⁸, E. Guilloton ¹⁶⁸, S. Guindon ³⁶, F. Guo ^{14a,14e}, J. Guo ^{62c},

L. Guo ⁴⁸, Y. Guo ¹⁰⁷, R. Gupta ¹³⁰, S. Gurbuz ²⁴, S.S. Gurdasani ⁵⁴, G. Gustavino ³⁶,
 M. Guth ⁵⁶, P. Gutierrez ¹²¹, L.F. Gutierrez Zagazeta ¹²⁹, M. Gutsche ⁵⁰, C. Gutschow ⁹⁷,
 C. Gwenlan ¹²⁷, C.B. Gwilliam ⁹³, E.S. Haaland ¹²⁶, A. Haas ¹¹⁸, M. Habedank ⁴⁸,
 C. Haber ^{17a}, H.K. Hadavand ⁸, A. Hadeef ⁵⁰, S. Hadzic ¹¹¹, A.I. Hagan ⁹², J.J. Hahn ¹⁴²,
 E.H. Haines ⁹⁷, M. Haleem ¹⁶⁷, J. Haley ¹²², J.J. Hall ¹⁴⁰, G.D. Hallewell ¹⁰³, L. Halser ¹⁹,
 K. Hamano ¹⁶⁶, M. Hamer ²⁴, G.N. Hamity ⁵², E.J. Hampshire ⁹⁶, J. Han ^{62b}, K. Han ^{62a},
 L. Han ^{14c}, L. Han ^{62a}, S. Han ^{17a}, Y.F. Han ¹⁵⁶, K. Hanagaki ⁸⁴, M. Hance ¹³⁷,
 D.A. Hangal ⁴¹, H. Hanif ¹⁴³, M.D. Hank ¹²⁹, J.B. Hansen ⁴², P.H. Hansen ⁴², K. Hara ¹⁵⁸,
 D. Harada ⁵⁶, T. Harenberg ¹⁷², S. Harkusha ³⁷, M.L. Harris ¹⁰⁴, Y.T. Harris ¹²⁷, J. Harrison ¹³,
 N.M. Harrison ¹²⁰, P.F. Harrison ¹⁶⁸, N.M. Hartman ¹¹¹, N.M. Hartmann ¹¹⁰, R.Z. Hasan ^{96,135},
 Y. Hasegawa ¹⁴¹, S. Hassan ¹⁶, R. Hauser ¹⁰⁸, C.M. Hawkes ²⁰, R.J. Hawkings ³⁶,
 Y. Hayashi ¹⁵⁴, S. Hayashida ¹¹², D. Hayden ¹⁰⁸, C. Hayes ¹⁰⁷, R.L. Hayes ¹¹⁵, C.P. Hays ¹²⁷,
 J.M. Hays ⁹⁵, H.S. Hayward ⁹³, F. He ^{62a}, M. He ^{14a,14e}, Y. He ¹⁵⁵, Y. He ⁴⁸, Y. He ⁹⁷,
 N.B. Heatley ⁹⁵, V. Hedberg ⁹⁹, A.L. Heggelund ¹²⁶, N.D. Hehir ^{95,*}, C. Heidegger ⁵⁴,
 K.K. Heidegger ⁵⁴, W.D. Heidorn ⁸¹, J. Heilman ³⁴, S. Heim ⁴⁸, T. Heim ^{17a}, J.G. Heinlein ¹²⁹,
 J.J. Heinrich ¹²⁴, L. Heinrich ^{111,ab}, J. Hejbal ¹³², A. Held ¹⁷¹, S. Hellesund ¹⁶,
 C.M. Helling ¹⁶⁵, S. Hellman ^{47a,47b}, R.C.W. Henderson ⁹², L. Henkelmann ³²,
 A.M. Henriques Correia ³⁶, H. Herde ⁹⁹, Y. Hernández Jiménez ¹⁴⁶, L.M. Herrmann ²⁴,
 T. Herrmann ⁵⁰, G. Herten ⁵⁴, R. Hertenberger ¹¹⁰, L. Hervas ³⁶, M.E. Hesping ¹⁰¹,
 N.P. Hesse ^{157a}, M. Hidaoui ^{35b}, E. Hill ¹⁵⁶, S.J. Hillier ²⁰, J.R. Hinds ¹⁰⁸, F. Hinterkeuser ²⁴,
 M. Hirose ¹²⁵, S. Hirose ¹⁵⁸, D. Hirschbuehl ¹⁷², T.G. Hitchings ¹⁰², B. Hiti ⁹⁴, J. Hobbs ¹⁴⁶,
 R. Hobincu ^{27e}, N. Hod ¹⁷⁰, M.C. Hodgkinson ¹⁴⁰, B.H. Hodgkinson ¹²⁷, A. Hoecker ³⁶,
 D.D. Hofer ¹⁰⁷, J. Hofer ⁴⁸, T. Holm ²⁴, M. Holzbock ¹¹¹, L.B.A.H. Hommels ³²,
 B.P. Honan ¹⁰², J.J. Hong ⁶⁸, J. Hong ^{62c}, T.M. Hong ¹³⁰, B.H. Hooberman ¹⁶³,
 W.H. Hopkins ⁶, M.C. Hoppesch ¹⁶³, Y. Horii ¹¹², S. Hou ¹⁴⁹, A.S. Howard ⁹⁴, J. Howarth ⁵⁹,
 J. Hoya ⁶, M. Hrabovsky ¹²³, A. Hrynevich ⁴⁸, T. Hryn'ova ⁴, P.J. Hsu ⁶⁵, S.-C. Hsu ¹³⁹,
 T. Hsu ⁶⁶, M. Hu ^{17a}, Q. Hu ^{62a}, S. Huang ^{64b}, X. Huang ^{14a,14e}, Y. Huang ¹⁴⁰, Y. Huang ¹⁰¹,
 Y. Huang ^{14a}, Z. Huang ¹⁰², Z. Hubacek ¹³³, M. Huebner ²⁴, F. Huegging ²⁴, T.B. Huffman ¹²⁷,
 C.A. Hugli ⁴⁸, M. Huhtinen ³⁶, S.K. Huiberts ¹⁶, R. Hulsken ¹⁰⁵, N. Huseynov ¹², J. Huston ¹⁰⁸,
 J. Huth ⁶¹, R. Hyneman ¹⁴⁴, G. Iacobucci ⁵⁶, G. Iakovidis ²⁹, L. Iconomidou-Fayard ⁶⁶,
 J.P. Iddon ³⁶, P. Iengo ^{72a,72b}, R. Iguchi ¹⁵⁴, T. Iizawa ¹²⁷, Y. Ikegami ⁸⁴, N. Ilic ¹⁵⁶,
 H. Imam ^{35a}, M. Ince Lezki ⁵⁶, T. Ingebretsen Carlson ^{47a,47b}, G. Introzzi ^{73a,73b}, M. Iodice ^{77a},
 V. Ippolito ^{75a,75b}, R.K. Irwin ⁹³, M. Ishino ¹⁵⁴, W. Islam ¹⁷¹, C. Issever ^{18,48}, S. Istin ^{21a,ah},
 H. Ito ¹⁶⁹, R. Iuppa ^{78a,78b}, A. Ivina ¹⁷⁰, J.M. Izen ⁴⁵, V. Izzo ^{72a}, P. Jacka ¹³², P. Jackson ¹,
 C.S. Jagfeld ¹¹⁰, G. Jain ^{157a}, P. Jain ⁴⁸, K. Jakobs ⁵⁴, T. Jakoubek ¹⁷⁰, J. Jamieson ⁵⁹,
 M. Javurkova ¹⁰⁴, L. Jeanty ¹²⁴, J. Jejelava ^{150a,y}, P. Jenni ^{54,f}, C.E. Jessiman ³⁴, C. Jia ^{62b},
 J. Jia ¹⁴⁶, X. Jia ⁶¹, X. Jia ^{14a,14e}, Z. Jia ^{14c}, C. Jiang ⁵², S. Jiggins ⁴⁸, J. Jimenez Pena ¹³,
 S. Jin ^{14c}, A. Jinaru ^{27b}, O. Jinnouchi ¹⁵⁵, P. Johansson ¹⁴⁰, K.A. Johns ⁷, J.W. Johnson ¹³⁷,
 D.M. Jones ¹⁴⁷, E. Jones ⁴⁸, P. Jones ³², R.W.L. Jones ⁹², T.J. Jones ⁹³, H.L. Joos ^{55,36},
 R. Joshi ¹²⁰, J. Jovicevic ¹⁵, X. Ju ^{17a}, J.J. Junggeburth ¹⁰⁴, T. Junkermann ^{63a},
 A. Juste Rozas ^{13,r}, M.K. Juzek ⁸⁷, S. Kabana ^{138e}, A. Kaczmarzka ⁸⁷, M. Kado ¹¹¹,
 H. Kagan ¹²⁰, M. Kagan ¹⁴⁴, A. Kahn ¹²⁹, C. Kahra ¹⁰¹, T. Kaji ¹⁵⁴, E. Kajomovitz ¹⁵¹,
 N. Kakati ¹⁷⁰, I. Kalaitzidou ⁵⁴, C.W. Kalderon ²⁹, N.J. Kang ¹³⁷, D. Kar ^{33g}, K. Karava ¹²⁷,
 M.J. Kareem ^{157b}, E. Karentzos ⁵⁴, O. Karkout ¹¹⁵, S.N. Karpov ³⁸, Z.M. Karpova ³⁸,
 V. Kartvelishvili ⁹², A.N. Karyukhin ³⁷, E. Kasimi ¹⁵³, J. Katzy ⁴⁸, S. Kaur ³⁴, K. Kawade ¹⁴¹,
 M.P. Kawale ¹²¹, C. Kawamoto ⁸⁸, T. Kawamoto ^{62a}, E.F. Kay ³⁶, F.I. Kaya ¹⁵⁹, S. Kazakos ¹⁰⁸,
 V.F. Kazanin ³⁷, Y. Ke ¹⁴⁶, J.M. Keaveney ^{33a}, R. Keeler ¹⁶⁶, G.V. Kehris ⁶¹, J.S. Keller ³⁴,

A.S. Kelly⁹⁷, J.J. Kempster¹⁴⁷, P.D. Kennedy¹⁰¹, O. Kepka¹³², B.P. Kerridge¹³⁵, S. Kersten¹⁷²,
 B.P. Kerševan⁹⁴, L. Keszezhova^{28a}, S. Ketabchi Haghighat¹⁵⁶, R.A. Khan¹³⁰, A. Khanov¹²²,
 A.G. Kharlamov³⁷, T. Kharlamova³⁷, E.E. Khoda¹³⁹, M. Kholodenko³⁷, T.J. Khoo¹⁸,
 G. Khoriauli¹⁶⁷, J. Khubua^{150b}, Y.A.R. Khwaira¹²⁸, B. Kibirige^{33g}, D.W. Kim^{47a,47b},
 Y.K. Kim³⁹, N. Kimura⁹⁷, M.K. Kingston⁵⁵, A. Kirchoff⁵⁵, C. Kirfel²⁴, F. Kirfel²⁴,
 J. Kirk¹³⁵, A.E. Kiryunin¹¹¹, C. Kitsaki¹⁰, O. Kivernyk²⁴, M. Klassen¹⁵⁹, C. Klein³⁴,
 L. Klein¹⁶⁷, M.H. Klein⁴⁴, S.B. Klein⁵⁶, U. Klein⁹³, P. Klimek³⁶, A. Klimentov²⁹,
 T. Klioutchnikova³⁶, P. Kluit¹¹⁵, S. Kluth¹¹¹, E. Kneringer⁷⁹, T.M. Knight¹⁵⁶, A. Knue⁴⁹,
 R. Kobayashi⁸⁸, D. Kobylanski¹⁷⁰, S.F. Koch¹²⁷, M. Kocian¹⁴⁴, P. Kodyš¹³⁴,
 D.M. Koeck¹²⁴, P.T. Koenig²⁴, T. Koffas³⁴, O. Kolay⁵⁰, I. Koletsou⁴, T. Komarek¹²³,
 K. Köneke⁵⁴, A.X.Y. Kong¹, T. Kono¹¹⁹, N. Konstantinidis⁹⁷, P. Kontaxakis⁵⁶, B. Konya⁹⁹,
 R. Kopeliansky⁴¹, S. Koperny^{86a}, K. Korcyl⁸⁷, K. Kordas^{153,d}, A. Korn⁹⁷, S. Korn⁵⁵,
 I. Korolkov¹³, N. Korotkova³⁷, B. Kortman¹¹⁵, O. Kortner¹¹¹, S. Kortner¹¹¹,
 W.H. Kostecka¹¹⁶, V.V. Kostyukhin¹⁴², A. Kotsokechagia¹³⁶, A. Kotwal⁵¹, A. Koulouris³⁶,
 A. Kourkoumeli-Charalampidi^{73a,73b}, C. Kourkoumelis⁹, E. Kourlitis^{111,ab}, O. Kovanda¹²⁴,
 R. Kowalewski¹⁶⁶, W. Kozanecki¹³⁶, A.S. Kozhin³⁷, V.A. Kramarenko³⁷, G. Kramberger⁹⁴,
 P. Kramer¹⁰¹, M.W. Krasny¹²⁸, A. Krasznahorkay³⁶, J.W. Kraus¹⁷², J.A. Kremer⁴⁸,
 T. Kresse⁵⁰, J. Kretschmar⁹³, K. Kreul¹⁸, P. Krieger¹⁵⁶, S. Krishnamurthy¹⁰⁴,
 M. Krivos¹³⁴, K. Krizka²⁰, K. Kroeninger⁴⁹, H. Kroha¹¹¹, J. Kroll¹³², J. Kroll¹²⁹,
 K.S. Krowpman¹⁰⁸, U. Kruchonak³⁸, H. Krüger²⁴, N. Krumnack⁸¹, M.C. Kruse⁵¹,
 O. Kuchinskaia³⁷, S. Kuday^{3a}, S. Kuehn³⁶, R. Kuesters⁵⁴, T. Kuhl⁴⁸, V. Kukhtin³⁸,
 Y. Kulchitsky^{37,a}, S. Kuleshov^{138d,138b}, M. Kumar^{33g}, N. Kumari⁴⁸, P. Kumari^{157b},
 A. Kupco¹³², T. Kupfer⁴⁹, A. Kupich³⁷, O. Kuprash⁵⁴, H. Kurashige⁸⁵, L.L. Kurchaninov^{157a},
 O. Kurdysh⁶⁶, Y.A. Kurochkin³⁷, A. Kurova³⁷, M. Kuze¹⁵⁵, A.K. Kvam¹⁰⁴, J. Kvita¹²³,
 T. Kwan¹⁰⁵, N.G. Kyriacou¹⁰⁷, L.A.O. Laatu¹⁰³, C. Lacasta¹⁶⁴, F. Lacava^{75a,75b},
 H. Lacker¹⁸, D. Lacour¹²⁸, N.N. Lad⁹⁷, E. Ladygin³⁸, A. Lafarge⁴⁰, B. Laforge¹²⁸,
 T. Lagouri¹⁷³, F.Z. Lahbabi^{35a}, S. Lai⁵⁵, J.E. Lambert¹⁶⁶, S. Lammers⁶⁸, W. Lampl⁷,
 C. Lampoudis^{153,d}, G. Lamprinoudis¹⁰¹, A.N. Lancaster¹¹⁶, E. Lançon²⁹, U. Landgraf⁵⁴,
 M.P.J. Landon⁹⁵, V.S. Lang⁵⁴, O.K.B. Langrekken¹²⁶, A.J. Lankford¹⁶⁰, F. Lanni³⁶,
 K. Lantzsck²⁴, A. Lanza^{73a}, J.F. Laporte¹³⁶, T. Lari^{71a}, F. Lasagni Manghi^{23b}, M. Lassnig³⁶,
 V. Latonova¹³², A. Laudrain¹⁰¹, A. Laurier¹⁵¹, S.D. Lawlor¹⁴⁰, Z. Lawrence¹⁰²,
 R. Lazaridou¹⁶⁸, M. Lazzaroni^{71a,71b}, B. Le¹⁰², E.M. Le Boulicaut⁵¹, L.T. Le Pottier^{17a},
 B. Leban^{23b,23a}, A. Lebedev⁸¹, M. LeBlanc¹⁰², F. Ledroit-Guillon⁶⁰, S.C. Lee¹⁴⁹,
 S. Lee^{47a,47b}, T.F. Lee⁹³, L.L. Leeuw^{33c}, H.P. Lefebvre⁹⁶, M. Lefebvre¹⁶⁶, C. Leggett^{17a},
 G. Lehmann Miotto³⁶, M. Leigh⁵⁶, W.A. Leight¹⁰⁴, W. Leinonen¹¹⁴, A. Leisos^{153,q},
 M.A.L. Leite^{83c}, C.E. Leitgeb¹⁸, R. Leitner¹³⁴, K.J.C. Leney⁴⁴, T. Lenz²⁴, S. Leone^{74a},
 C. Leonidopoulos⁵², A. Leopold¹⁴⁵, C. Leroy¹⁰⁹, R. Les¹⁰⁸, C.G. Lester³², M. Levchenko³⁷,
 J. Levêque⁴, L.J. Levinson¹⁷⁰, G. Levrini^{23b,23a}, M.P. Lewicki⁸⁷, C. Lewis¹³⁹, D.J. Lewis⁴,
 A. Li⁵, B. Li^{62b}, C. Li^{62a}, C-Q. Li¹¹¹, H. Li^{62a}, H. Li^{62b}, H. Li^{14c}, H. Li^{14b}, H. Li^{62b},
 J. Li^{62c}, K. Li¹³⁹, L. Li^{62c}, M. Li^{14a,14e}, S. Li^{14a,14e}, S. Li^{62d,62c}, T. Li⁵, X. Li¹⁰⁵,
 Z. Li¹²⁷, Z. Li¹⁵⁴, Z. Li^{14a,14e}, S. Liang^{14a,14e}, Z. Liang^{14a}, M. Liberatore¹³⁶, B. Liberti^{76a},
 K. Lie^{64c}, J. Lieber Marin^{83e}, H. Lien⁶⁸, K. Lin¹⁰⁸, R.E. Lindley⁷, J.H. Lindon²,
 E. Lipeles¹²⁹, A. Lipniacka¹⁶, A. Lister¹⁶⁵, J.D. Little⁴, B. Liu^{14a}, B.X. Liu^{14d},
 D. Liu^{62d,62c}, E.H.L. Liu²⁰, J.B. Liu^{62a}, J.K.K. Liu³², K. Liu^{62d}, K. Liu^{62d,62c}, M. Liu^{62a},
 M.Y. Liu^{62a}, P. Liu^{14a}, Q. Liu^{62d,139,62c}, X. Liu^{62a}, X. Liu^{62b}, Y. Liu^{14d,14e}, Y.L. Liu^{62b},
 Y.W. Liu^{62a}, J. Llorente Merino¹⁴³, S.L. Lloyd⁹⁵, E.M. Lobodzinska⁴⁸, P. Loch⁷,
 T. Lohse¹⁸, K. Lohwasser¹⁴⁰, E. Loiacono⁴⁸, M. Lokajicek^{132,*}, J.D. Lomas²⁰,

J.D. Long ¹⁶³, I. Longarini ¹⁶⁰, R. Longo ¹⁶³, I. Lopez Paz ⁶⁷, A. Lopez Solis ⁴⁸,
 N. Lorenzo Martinez ⁴, A.M. Lory ¹¹⁰, M. Losada ^{117a}, G. Löschcke Centeno ¹⁴⁷, O. Loseva ³⁷,
 X. Lou ^{47a,47b}, X. Lou ^{14a,14e}, A. Lounis ⁶⁶, P.A. Love ⁹², G. Lu ^{14a,14e}, M. Lu ⁶⁶, S. Lu ¹²⁹,
 Y.J. Lu ⁶⁵, H.J. Lubatti ¹³⁹, C. Luci ^{75a,75b}, F.L. Lucio Alves ^{14c}, F. Luehring ⁶⁸, I. Luise ¹⁴⁶,
 O. Lukianchuk ⁶⁶, O. Lundberg ¹⁴⁵, B. Lund-Jensen ¹⁴⁵, N.A. Luongo ⁶, M.S. Lutz ³⁶,
 A.B. Lux ²⁵, D. Lynn ²⁹, R. Lysak ¹³², E. Lytken ⁹⁹, V. Lyubushkin ³⁸, T. Lyubushkina ³⁸,
 M.M. Lyukova ¹⁴⁶, M.Firdaus M. Soberi ⁵², H. Ma ²⁹, K. Ma ^{62a}, L.L. Ma ^{62b}, W. Ma ^{62a},
 Y. Ma ¹²², G. Maccarrone ⁵³, J.C. MacDonald ¹⁰¹, P.C. Machado De Abreu Farias ^{83e},
 R. Madar ⁴⁰, T. Madula ⁹⁷, J. Maeda ⁸⁵, T. Maeno ²⁹, H. Maguire ¹⁴⁰, V. Maiboroda ¹³⁶,
 A. Maio ^{131a,131b,131d}, K. Maj ^{86a}, O. Majersky ⁴⁸, S. Majewski ¹²⁴, N. Makovec ⁶⁶,
 V. Maksimovic ¹⁵, B. Malaescu ¹²⁸, Pa. Malecki ⁸⁷, V.P. Maleev ³⁷, F. Malek ^{60,m}, M. Mali ⁹⁴,
 D. Malito ⁹⁶, U. Mallik ⁸⁰, S. Maltezos ¹⁰, S. Malyukov ³⁸, J. Mamuzic ¹³, G. Mancini ⁵³,
 M.N. Mancini ²⁶, G. Manco ^{73a,73b}, J.P. Mandalia ⁹⁵, I. Mandić ⁹⁴,
 L. Manhaes de Andrade Filho ^{83a}, I.M. Maniatis ¹⁷⁰, J. Manjarres Ramos ⁹⁰, D.C. Mankad ¹⁷⁰,
 A. Mann ¹¹⁰, S. Manzoni ³⁶, L. Mao ^{62c}, X. Mapekula ^{33c}, A. Marantis ^{153,q}, G. Marchiori ⁵,
 M. Marcisovsky ¹³², C. Marcon ^{71a}, M. Marinescu ²⁰, S. Marium ⁴⁸, M. Marjanovic ¹²¹,
 A. Markhoos ⁵⁴, M. Markovitch ⁶⁶, E.J. Marshall ⁹², Z. Marshall ^{17a}, S. Marti-Garcia ¹⁶⁴,
 T.A. Martin ¹³⁵, V.J. Martin ⁵², B. Martin dit Latour ¹⁶, L. Martinelli ^{75a,75b}, M. Martinez ^{13,r},
 P. Martinez Agullo ¹⁶⁴, V.I. Martinez Outschoorn ¹⁰⁴, P. Martinez Suarez ¹³, S. Martin-Haugh ¹³⁵,
 G. Martinovicova ¹³⁴, V.S. Martoiu ^{27b}, A.C. Martyniuk ⁹⁷, A. Marzin ³⁶, D. Mascione ^{78a,78b},
 L. Masetti ¹⁰¹, T. Mashimo ¹⁵⁴, J. Masik ¹⁰², A.L. Maslennikov ³⁷, P. Massarotti ^{72a,72b},
 P. Mastrandrea ^{74a,74b}, A. Mastroberardino ^{43b,43a}, T. Masubuchi ¹⁵⁴, T. Mathisen ¹⁶²,
 J. Matousek ¹³⁴, N. Matsuzawa ¹⁵⁴, J. Maurer ^{27b}, A.J. Maury ⁶⁶, B. Maček ⁹⁴, D.A. Maximov ³⁷,
 A.E. May ¹⁰², R. Mazini ¹⁴⁹, I. Maznas ¹¹⁶, M. Mazza ¹⁰⁸, S.M. Mazza ¹³⁷, E. Mazzeo ^{71a,71b},
 C. Mc Ginn ²⁹, J.P. Mc Gowan ¹⁶⁶, S.P. Mc Kee ¹⁰⁷, C.C. McCracken ¹⁶⁵, E.F. McDonald ¹⁰⁶,
 A.E. McDougall ¹¹⁵, J.A. Mcfayden ¹⁴⁷, R.P. McGovern ¹²⁹, G. Mchedlidze ^{150b},
 R.P. Mckenzie ^{33g}, T.C. Mclachlan ⁴⁸, D.J. Mclaughlin ⁹⁷, S.J. McMahon ¹³⁵,
 C.M. Mcpartland ⁹³, R.A. McPherson ^{166,v}, S. Mehlhase ¹¹⁰, A. Mehta ⁹³, D. Melini ¹⁶⁴,
 B.R. Mellado Garcia ^{33g}, A.H. Melo ⁵⁵, F. Meloni ⁴⁸, A.M. Mendes Jacques Da Costa ¹⁰²,
 H.Y. Meng ¹⁵⁶, L. Meng ⁹², S. Menke ¹¹¹, M. Mentink ³⁶, E. Meoni ^{43b,43a}, G. Mercado ¹¹⁶,
 S. Merianos ¹⁵³, C. Merlassino ^{69a,69c}, L. Merola ^{72a,72b}, C. Meroni ^{71a,71b}, J. Metcalfe ⁶,
 A.S. Mete ⁶, E. Meuser ¹⁰¹, C. Meyer ⁶⁸, J-P. Meyer ¹³⁶, R.P. Middleton ¹³⁵, L. Mijović ⁵²,
 G. Mikenberg ¹⁷⁰, M. Mikestikova ¹³², M. Mikuž ⁹⁴, H. Mildner ¹⁰¹, A. Milic ³⁶,
 D.W. Miller ³⁹, E.H. Miller ¹⁴⁴, L.S. Miller ³⁴, A. Milov ¹⁷⁰, D.A. Milstead ^{47a,47b}, T. Min ^{14c},
 A.A. Minaenko ³⁷, I.A. Minashvili ^{150b}, L. Mince ⁵⁹, A.I. Mincer ¹¹⁸, B. Mindur ^{86a},
 M. Mineev ³⁸, Y. Mino ⁸⁸, L.M. Mir ¹³, M. Miralles Lopez ⁵⁹, M. Mironova ^{17a}, A. Mishima ¹⁵⁴,
 M.C. Missio ¹¹⁴, A. Mitra ¹⁶⁸, V.A. Mitsou ¹⁶⁴, Y. Mitsumori ¹¹², O. Miu ¹⁵⁶,
 P.S. Miyagawa ⁹⁵, T. Mkrtchyan ^{63a}, M. Mlinarevic ⁹⁷, T. Mlinarevic ⁹⁷, M. Mlynarikova ³⁶,
 S. Mobius ¹⁹, P. Mogg ¹¹⁰, M.H. Mohamed Farook ¹¹³, A.F. Mohammed ^{14a,14e}, S. Mohapatra ⁴¹,
 G. Mokgatitwane ^{33g}, L. Moleri ¹⁷⁰, B. Mondal ¹⁴², S. Mondal ¹³³, K. Mönig ⁴⁸,
 E. Monnier ¹⁰³, L. Monsonis Romero ¹⁶⁴, J. Montejo Berlingen ¹³, M. Montella ¹²⁰,
 F. Montekali ^{77a,77b}, F. Monticelli ⁹¹, S. Monzani ^{69a,69c}, N. Morange ⁶⁶,
 A.L. Moreira De Carvalho ⁴⁸, M. Moreno Llácer ¹⁶⁴, C. Moreno Martinez ⁵⁶, P. Morettini ^{57b},
 S. Morgenstern ³⁶, M. Morii ⁶¹, M. Morinaga ¹⁵⁴, F. Morodei ^{75a,75b}, L. Morvaj ³⁶,
 P. Moschovakos ³⁶, B. Moser ³⁶, M. Mosidze ^{150b}, T. Moskalets ⁵⁴, P. Moskvitina ¹¹⁴,
 J. Moss ^{31,j}, P. Moszkowicz ^{86a}, A. Moussa ^{35d}, E.J.W. Moyse ¹⁰⁴, O. Mtintsilana ^{33g},
 S. Muanza ¹⁰³, J. Mueller ¹³⁰, D. Muenstermann ⁹², R. Müller ¹⁹, G.A. Mullier ¹⁶²,

A.J. Mullin³², J.J. Mullin¹²⁹, D.P. Mungo¹⁵⁶, D. Munoz Perez¹⁶⁴, F.J. Munoz Sanchez¹⁰²,
 M. Murin¹⁰², W.J. Murray^{168,135}, M. Muškinja⁹⁴, C. Mwewa²⁹, A.G. Myagkov^{37,a},
 A.J. Myers⁸, G. Myers¹⁰⁷, M. Myska¹³³, B.P. Nachman^{17a}, O. Nackenhorst⁴⁹, K. Nagai¹²⁷,
 K. Nagano⁸⁴, J.L. Nagle^{29,af}, E. Nagy¹⁰³, A.M. Nairz³⁶, Y. Nakahama⁸⁴, K. Nakamura⁸⁴,
 K. Nakkalil⁵, H. Nanjo¹²⁵, E.A. Narayanan¹¹³, I. Naryshkin³⁷, L. Nasella^{71a,71b},
 M. Naseri³⁴, S. Nasri^{117b}, C. Nass²⁴, G. Navarro^{22a}, J. Navarro-Gonzalez¹⁶⁴, R. Nayak¹⁵²,
 A. Nayaz¹⁸, P.Y. Nechaeva³⁷, S. Nechaeva^{23b,23a}, F. Nechansky⁴⁸, L. Nedic¹²⁷, T.J. Neep²⁰,
 A. Negri^{73a,73b}, M. Negrini^{23b}, C. Nellist¹¹⁵, C. Nelson¹⁰⁵, K. Nelson¹⁰⁷, S. Nemecek¹³²,
 M. Nessi^{36,g}, M.S. Neubauer¹⁶³, F. Neuhaus¹⁰¹, J. Neundorf⁴⁸, P.R. Newman²⁰,
 C.W. Ng¹³⁰, Y.W.Y. Ng⁴⁸, B. Ngair^{117a}, H.D.N. Nguyen¹⁰⁹, R.B. Nickerson¹²⁷,
 R. Nicolaidou¹³⁶, J. Nielsen¹³⁷, M. Niemeyer⁵⁵, J. Niermann⁵⁵, N. Nikiforou³⁶,
 V. Nikolaenko^{37,a}, I. Nikolic-Audit¹²⁸, K. Nikolopoulos²⁰, P. Nilsson²⁹, I. Ninca⁴⁸,
 G. Ninio¹⁵², A. Nisati^{75a}, N. Nishu², R. Nisius¹¹¹, J-E. Nitschke⁵⁰, E.K. Nkadimeng^{33g},
 T. Nobe¹⁵⁴, T. Nommensen¹⁴⁸, M.B. Norfolk¹⁴⁰, R.R.B. Norisam⁹⁷, B.J. Norman³⁴,
 M. Noury^{35a}, J. Novak⁹⁴, T. Novak⁹⁴, L. Novotny¹³³, R. Novotny¹¹³, L. Nozka¹²³,
 K. Ntekas¹⁶⁰, N.M.J. Nunes De Moura Junior^{83b}, J. Ocariz¹²⁸, A. Ochi⁸⁵, I. Ochoa^{131a},
 S. Oerdek^{48,s}, J.T. Offermann³⁹, A. Ogrodnik¹³⁴, A. Oh¹⁰², C.C. Ohm¹⁴⁵, H. Oide⁸⁴,
 R. Oishi¹⁵⁴, M.L. Ojeda⁴⁸, Y. Okumura¹⁵⁴, L.F. Oleiro Seabra^{131a}, S.A. Olivares Pino^{138d},
 G. Oliveira Correa¹³, D. Oliveira Damazio²⁹, D. Oliveira Goncalves^{83a}, J.L. Oliver¹⁶⁰,
 Ö.O. Öncel⁵⁴, A.P. O'Neill¹⁹, A. Onofre^{131a,131e}, P.U.E. Onyisi¹¹, M.J. Oreglia³⁹,
 G.E. Orellana⁹¹, D. Orestano^{77a,77b}, N. Orlando¹³, R.S. Orr¹⁵⁶, V. O'Shea⁵⁹,
 L.M. Osojnak¹²⁹, R. Ospanov^{62a}, G. Otero y Garzon³⁰, H. Otono⁸⁹, P.S. Ott^{63a},
 G.J. Ottino^{17a}, M. Ouchrif^{35d}, F. Ould-Saada¹²⁶, T. Ovsiannikova¹³⁹, M. Owen⁵⁹,
 R.E. Owen¹³⁵, V.E. Ozcan^{21a}, F. Ozturk⁸⁷, N. Ozturk⁸, S. Ozturk⁸², H.A. Pacey¹²⁷,
 A. Pacheco Pages¹³, C. Padilla Aranda¹³, G. Padovano^{75a,75b}, S. Pagan Griso^{17a},
 G. Palacino⁶⁸, A. Palazzo^{70a,70b}, J. Pampel²⁴, J. Pan¹⁷³, T. Pan^{64a}, D.K. Panchal¹¹,
 C.E. Pandini¹¹⁵, J.G. Panduro Vazquez¹³⁵, H.D. Pandya¹, H. Pang^{14b}, P. Pani⁴⁸,
 G. Panizzo^{69a,69c}, L. Panwar¹²⁸, L. Paolozzi⁵⁶, S. Parajuli¹⁶³, A. Paramonov⁶,
 C. Paraskevopoulos⁵³, D. Paredes Hernandez^{64b}, A. Pareti^{73a,73b}, K.R. Park⁴¹, T.H. Park¹⁵⁶,
 M.A. Parker³², F. Parodi^{57b,57a}, E.W. Parrish¹¹⁶, V.A. Parrish⁵², J.A. Parsons⁴¹,
 U. Parzefall⁵⁴, B. Pascual Dias¹⁰⁹, L. Pascual Dominguez¹⁰⁰, E. Pasqualucci^{75a},
 S. Passaggio^{57b}, F. Pastore⁹⁶, P. Patel⁸⁷, U.M. Patel⁵¹, J.R. Pater¹⁰², T. Pauly³⁶,
 C.I. Pazos¹⁵⁹, J. Pearkes¹⁴⁴, M. Pedersen¹²⁶, R. Pedro^{131a}, S.V. Peleganchuk³⁷, O. Penc³⁶,
 E.A. Pender⁵², G.D. Penn¹⁷³, K.E. Penski¹¹⁰, M. Penzin³⁷, B.S. Peralva^{83d},
 A.P. Pereira Peixoto¹³⁹, L. Pereira Sanchez¹⁴⁴, D.V. Perepelitsa^{29,af}, E. Perez Codina^{157a},
 M. Perganti¹⁰, H. Pernegger³⁶, O. Perrin⁴⁰, K. Peters⁴⁸, R.F.Y. Peters¹⁰², B.A. Petersen³⁶,
 T.C. Petersen⁴², E. Petit¹⁰³, V. Petousis¹³³, C. Petridou^{153,d}, T. Petru¹³⁴, A. Petrukhin¹⁴²,
 M. Pettee^{17a}, N.E. Pettersson³⁶, A. Petukhov³⁷, K. Petukhova¹³⁴, R. Pezoa^{138f},
 L. Pezzotti³⁶, G. Pezzullo¹⁷³, T.M. Pham¹⁷¹, T. Pham¹⁰⁶, P.W. Phillips¹³⁵, G. Piacquadio¹⁴⁶,
 E. Pianori^{17a}, F. Piazza¹²⁴, R. Piegai³⁰, D. Pietreanu^{27b}, A.D. Pilkington¹⁰²,
 M. Pinamonti^{69a,69c}, J.L. Pinfeld², B.C. Pinheiro Pereira^{131a}, A.E. Pinto Pinoargote^{136,136},
 L. Pintucci^{69a,69c}, K.M. Piper¹⁴⁷, A. Pirttikoski⁵⁶, D.A. Pizzi³⁴, L. Pizzimento^{64b},
 A. Pizzini¹¹⁵, M.-A. Pleier²⁹, V. Pleskot¹³⁴, E. Plotnikova³⁸, G. Poddar⁹⁵, R. Poettgen⁹⁹,
 L. Poggioli¹²⁸, I. Pokharel⁵⁵, S. Polacek¹³⁴, G. Polesello^{73a}, A. Poley^{143,157a}, A. Polini^{23b},
 C.S. Pollard¹⁶⁸, Z.B. Pollock¹²⁰, E. Pompa Pacchi^{75a,75b}, N.I. Pond⁹⁷, D. Ponomarenko¹¹⁴,
 L. Pontecorvo³⁶, S. Popa^{27a}, G.A. Popeneciu^{27d}, A. Poreba³⁶, D.M. Portillo Quintero^{157a},
 S. Pospisil¹³³, M.A. Postill¹⁴⁰, P. Postolache^{27c}, K. Potamianos¹⁶⁸, P.A. Potepa^{86a},

I.N. Potrap ³⁸, C.J. Potter ³², H. Potti ¹, J. Poveda ¹⁶⁴, M.E. Pozo Astigarraga ³⁶,
 A. Prades Ibanez ¹⁶⁴, J. Pretel ⁵⁴, D. Price ¹⁰², M. Primavera ^{70a}, M.A. Principe Martin ¹⁰⁰,
 R. Privara ¹²³, T. Procter ⁵⁹, M.L. Proffitt ¹³⁹, N. Proklova ¹²⁹, K. Prokofiev ^{64c}, G. Proto ¹¹¹,
 J. Proudfoot ⁶, M. Przybycien ^{86a}, W.W. Przygoda ^{86b}, A. Psallidas ⁴⁶, J.E. Puddefoot ¹⁴⁰,
 D. Pudzha ³⁷, D. Pyatiizbyantseva ³⁷, J. Qian ¹⁰⁷, D. Qichen ¹⁰², Y. Qin ¹³, T. Qiu ⁵²,
 A. Quadt ⁵⁵, M. Queitsch-Maitland ¹⁰², G. Quetant ⁵⁶, R.P. Quinn ¹⁶⁵, G. Rabanal Bolanos ⁶¹,
 D. Rafanoharana ⁵⁴, F. Raffaelli ^{76a,76b}, F. Ragusa ^{71a,71b}, J.L. Rainbolt ³⁹, J.A. Raine ⁵⁶,
 S. Rajagopalan ²⁹, E. Ramakoti ³⁷, I.A. Ramirez-Berend ³⁴, K. Ran ^{48,14e}, N.P. Rapheeha ^{33g},
 H. Rasheed ^{27b}, V. Raskina ¹²⁸, D.F. Rassloff ^{63a}, A. Rastogi ^{17a}, S. Rave ¹⁰¹, B. Ravina ⁵⁵,
 I. Ravinovich ¹⁷⁰, M. Raymond ³⁶, A.L. Read ¹²⁶, N.P. Readioff ¹⁴⁰, D.M. Rebuzzi ^{73a,73b},
 G. Redlinger ²⁹, A.S. Reed ¹¹¹, K. Reeves ²⁶, J.A. Reidelsturz ¹⁷², D. Reikher ¹⁵², A. Rej ⁴⁹,
 C. Rembser ³⁶, M. Renda ^{27b}, M.B. Rendel ¹¹¹, F. Renner ⁴⁸, A.G. Rennie ¹⁶⁰, A.L. Rescia ⁴⁸,
 S. Resconi ^{71a}, M. Ressegotti ^{57b,57a}, S. Rettie ³⁶, J.G. Reyes Rivera ¹⁰⁸, E. Reynolds ^{17a},
 O.L. Rezanova ³⁷, P. Reznicek ¹³⁴, H. Riani ^{35d}, N. Ribaric ⁹², E. Ricci ^{78a,78b}, R. Richter ¹¹¹,
 S. Richter ^{47a,47b}, E. Richter-Was ^{86b}, M. Ridel ¹²⁸, S. Ridouani ^{35d}, P. Rieck ¹¹⁸, P. Riedler ³⁶,
 E.M. Riefel ^{47a,47b}, J.O. Rieger ¹¹⁵, M. Rijssenbeek ¹⁴⁶, M. Rimoldi ³⁶, L. Rinaldi ^{23b,23a},
 T.T. Rinn ²⁹, M.P. Rinnagel ¹¹⁰, G. Ripellino ¹⁶², I. Riu ¹³, J.C. Rivera Vergara ¹⁶⁶,
 F. Rizatdinova ¹²², E. Rizvi ⁹⁵, B.R. Roberts ^{17a}, S.H. Robertson ^{105,v}, D. Robinson ³²,
 C.M. Robles Gajardo ^{138f}, M. Robles Manzano ¹⁰¹, A. Robson ⁵⁹, A. Rocchi ^{76a,76b}, C. Roda ^{74a,74b},
 S. Rodriguez Bosca ³⁶, Y. Rodriguez Garcia ^{22a}, A. Rodriguez Rodriguez ⁵⁴,
 A.M. Rodríguez Vera ¹¹⁶, S. Roe ³⁶, J.T. Roemer ¹⁶⁰, A.R. Roepe-Gier ¹³⁷, J. Roggel ¹⁷²,
 O. Røhne ¹²⁶, R.A. Rojas ¹⁰⁴, C.P.A. Roland ¹²⁸, J. Roloff ²⁹, A. Romaniouk ³⁷,
 E. Romano ^{73a,73b}, M. Romano ^{23b}, A.C. Romero Hernandez ¹⁶³, N. Rompotis ⁹³, L. Roos ¹²⁸,
 S. Rosati ^{75a}, B.J. Rosser ³⁹, E. Rossi ¹²⁷, E. Rossi ^{72a,72b}, L.P. Rossi ⁶¹, L. Rossini ⁵⁴,
 R. Rosten ¹²⁰, M. Rotaru ^{27b}, B. Rottler ⁵⁴, C. Rougier ⁹⁰, D. Rousseau ⁶⁶, D. Rousso ⁴⁸,
 A. Roy ¹⁶³, S. Roy-Garand ¹⁵⁶, A. Rozanov ¹⁰³, Z.M.A. Rozario ⁵⁹, Y. Rozen ¹⁵¹,
 A. Rubio Jimenez ¹⁶⁴, A.J. Ruby ⁹³, V.H. Ruelas Rivera ¹⁸, T.A. Ruggeri ¹, A. Ruggiero ¹²⁷,
 A. Ruiz-Martinez ¹⁶⁴, A. Rummler ³⁶, Z. Rurikova ⁵⁴, N.A. Rusakovich ³⁸, H.L. Russell ¹⁶⁶,
 G. Russo ^{75a,75b}, J.P. Rutherford ⁷, S. Rutherford Colmenares ³², M. Rybar ¹³⁴, E.B. Rye ¹²⁶,
 A. Ryzhov ⁴⁴, J.A. Sabater Iglesias ⁵⁶, P. Sabatini ¹⁶⁴, H.F.W. Sadrozinski ¹³⁷,
 F. Safai Tehrani ^{75a}, B. Safarzadeh Samani ¹³⁵, S. Saha ¹, M. Sahinsoy ¹¹¹, A. Saibel ¹⁶⁴,
 M. Saimpert ¹³⁶, M. Saito ¹⁵⁴, T. Saito ¹⁵⁴, A. Sala ^{71a,71b}, D. Salamani ³⁶, A. Salnikov ¹⁴⁴,
 J. Salt ¹⁶⁴, A. Salvador Salas ¹⁵², D. Salvatore ^{43b,43a}, F. Salvatore ¹⁴⁷, A. Salzburger ³⁶,
 D. Sammel ⁵⁴, E. Sampson ⁹², D. Sampsonidis ^{153,d}, D. Sampsonidou ¹²⁴, J. Sánchez ¹⁶⁴,
 V. Sanchez Sebastian ¹⁶⁴, H. Sandaker ¹²⁶, C.O. Sander ⁴⁸, J.A. Sandesara ¹⁰⁴, M. Sandhoff ¹⁷²,
 C. Sandoval ^{22b}, L. Sanfilippo ^{63a}, D.P.C. Sankey ¹³⁵, T. Sano ⁸⁸, A. Sansoni ⁵³, L. Santi ^{75a,75b},
 C. Santoni ⁴⁰, H. Santos ^{131a,131b}, A. Santra ¹⁷⁰, E. Sanzani ^{23b,23a}, K.A. Saoucha ¹⁶¹,
 J.G. Saraiva ^{131a,131d}, J. Sardain ⁷, O. Sasaki ⁸⁴, K. Sato ¹⁵⁸, C. Sauer ^{63b}, E. Sauvan ⁴,
 P. Savard ^{156,ad}, R. Sawada ¹⁵⁴, C. Sawyer ¹³⁵, L. Sawyer ⁹⁸, C. Sbarra ^{23b}, A. Sbrizzi ^{23b,23a},
 T. Scanlon ⁹⁷, J. Schaarschmidt ¹³⁹, U. Schäfer ¹⁰¹, A.C. Schaffer ^{66,44}, D. Schaile ¹¹⁰,
 R.D. Schamberger ¹⁴⁶, C. Scharf ¹⁸, M.M. Schefer ¹⁹, V.A. Schegelsky ³⁷, D. Scheirich ¹³⁴,
 M. Schernau ¹⁶⁰, C. Scheulen ⁵⁵, C. Schiavi ^{57b,57a}, M. Schioppa ^{43b,43a}, B. Schlag ^{144,1},
 K.E. Schleicher ⁵⁴, S. Schlenker ³⁶, J. Schmeing ¹⁷², M.A. Schmidt ¹⁷², K. Schmieden ¹⁰¹,
 C. Schmitt ¹⁰¹, N. Schmitt ¹⁰¹, S. Schmitt ⁴⁸, L. Schoeffel ¹³⁶, A. Schoening ^{63b},
 P.G. Scholer ³⁴, E. Schopf ¹²⁷, M. Schott ²⁴, J. Schovancova ³⁶, S. Schramm ⁵⁶, T. Schroer ⁵⁶,
 H-C. Schultz-Coulon ^{63a}, M. Schumacher ⁵⁴, B.A. Schumm ¹³⁷, Ph. Schune ¹³⁶, A.J. Schuy ¹³⁹,
 H.R. Schwartz ¹³⁷, A. Schwartzman ¹⁴⁴, T.A. Schwarz ¹⁰⁷, Ph. Schwemling ¹³⁶,

R. Schwienhorst ¹⁰⁸, A. Sciandra ²⁹, G. Sciolla ²⁶, F. Scuri ^{74a}, C.D. Sebastiani ⁹³,
 K. Sedlaczek ¹¹⁶, S.C. Seidel ¹¹³, A. Seiden ¹³⁷, B.D. Seidlitz ⁴¹, C. Seitz ⁴⁸, J.M. Seixas ^{83b},
 G. Sekhniaidze ^{72a}, L. Selem ⁶⁰, N. Semprini-Cesari ^{23b,23a}, D. Sengupta ⁵⁶, V. Senthilkumar ¹⁶⁴,
 L. Serin ⁶⁶, M. Sessa ^{76a,76b}, H. Severini ¹²¹, F. Sforza ^{57b,57a}, A. Sfyrla ⁵⁶, Q. Sha ^{14a},
 E. Shabalina ⁵⁵, A.H. Shah ³², R. Shaheen ¹⁴⁵, J.D. Shahinian ¹²⁹, D. Shaked Renous ¹⁷⁰,
 L.Y. Shan ^{14a}, M. Shapiro ^{17a}, A. Sharma ³⁶, A.S. Sharma ¹⁶⁵, P. Sharma ⁸⁰, P.B. Shatalov ³⁷,
 K. Shaw ¹⁴⁷, S.M. Shaw ¹⁰², Q. Shen ^{62c,5}, D.J. Sheppard ¹⁴³, P. Sherwood ⁹⁷, L. Shi ⁹⁷,
 X. Shi ^{14a}, C.O. Shimmin ¹⁷³, J.D. Shinner ⁹⁶, I.P.J. Shipsey ¹²⁷, S. Shirabe ⁸⁹,
 M. Shiyakova ^{38,t}, M.J. Shochet ³⁹, J. Shojaii ¹⁰⁶, D.R. Shope ¹²⁶, B. Shrestha ¹²¹,
 S. Shrestha ^{120,ag}, M.J. Shroff ¹⁶⁶, P. Sicho ¹³², A.M. Sickles ¹⁶³, E. Sideras Haddad ^{33g},
 A.C. Sidley ¹¹⁵, A. Sidoti ^{23b}, F. Siegert ⁵⁰, Dj. Sijacki ¹⁵, F. Sili ⁹¹, J.M. Silva ⁵²,
 M.V. Silva Oliveira ²⁹, S.B. Silverstein ^{47a}, S. Simion ⁶⁶, R. Simoniello ³⁶, E.L. Simpson ¹⁰²,
 H. Simpson ¹⁴⁷, L.R. Simpson ¹⁰⁷, N.D. Simpson ⁹⁹, S. Simsek ⁸², S. Sindhu ⁵⁵, P. Sinervo ¹⁵⁶,
 S. Singh ¹⁵⁶, S. Sinha ⁴⁸, S. Sinha ¹⁰², M. Sioli ^{23b,23a}, I. Siral ³⁶, E. Sitnikova ⁴⁸,
 J. Sjölin ^{47a,47b}, A. Skaf ⁵⁵, E. Skorda ²⁰, P. Skubic ¹²¹, M. Slawinska ⁸⁷, V. Smakhtin ¹⁷⁰,
 B.H. Smart ¹³⁵, S. Yu. Smirnov ³⁷, Y. Smirnov ³⁷, L.N. Smirnova ^{37,a}, O. Smirnova ⁹⁹,
 A.C. Smith ⁴¹, D.R. Smith ¹⁶⁰, E.A. Smith ³⁹, H.A. Smith ¹²⁷, J.L. Smith ¹⁰², R. Smith ¹⁴⁴,
 M. Smizanska ⁹², K. Smolek ¹³³, A.A. Snesarev ³⁷, S.R. Snider ¹⁵⁶, H.L. Snoek ¹¹⁵,
 S. Snyder ²⁹, R. Sobie ^{166,v}, A. Soffer ¹⁵², C.A. Solans Sanchez ³⁶, E. Yu. Soldatov ³⁷,
 U. Soldevila ¹⁶⁴, A.A. Solodkov ³⁷, S. Solomon ²⁶, A. Soloshenko ³⁸, K. Solovieva ⁵⁴,
 O.V. Solovyanov ⁴⁰, P. Sommer ³⁶, A. Sonay ¹³, W.Y. Song ^{157b}, A. Sopczak ¹³³, A.L. Soppio ⁹⁷,
 F. Sopkova ^{28b}, J.D. Sorenson ¹¹³, I.R. Sotarriva Alvarez ¹⁵⁵, V. Sothilingam ^{63a},
 O.J. Soto Sandoval ^{138c,138b}, S. Sottocornola ⁶⁸, R. Soualah ¹⁶¹, Z. Soumami ^{35e}, D. South ⁴⁸,
 N. Soybelman ¹⁷⁰, S. Spagnolo ^{70a,70b}, M. Spalla ¹¹¹, D. Sperlich ⁵⁴, G. Spigo ³⁶, S. Spinali ⁹²,
 D.P. Spiteri ⁵⁹, M. Spousta ¹³⁴, E.J. Staats ³⁴, R. Stamen ^{63a}, A. Stampeki ²⁰, M. Standke ²⁴,
 E. Stanecka ⁸⁷, W. Stanek-Maslouska ⁴⁸, M.V. Stange ⁵⁰, B. Stanislaus ^{17a}, M.M. Stanitzki ⁴⁸,
 B. Stapf ⁴⁸, E.A. Starchenko ³⁷, G.H. Stark ¹³⁷, J. Stark ⁹⁰, P. Staroba ¹³², P. Starovoitov ^{63a},
 S. Stärz ¹⁰⁵, R. Staszewski ⁸⁷, G. Stavropoulos ⁴⁶, J. Steentoft ¹⁶², P. Steinberg ²⁹,
 B. Stelzer ^{143,157a}, H.J. Stelzer ¹³⁰, O. Stelzer-Chilton ^{157a}, H. Stenzel ⁵⁸, T.J. Stevenson ¹⁴⁷,
 G.A. Stewart ³⁶, J.R. Stewart ¹²², M.C. Stockton ³⁶, G. Stoicea ^{27b}, M. Stolarski ^{131a},
 S. Stonjek ¹¹¹, A. Straessner ⁵⁰, J. Strandberg ¹⁴⁵, S. Strandberg ^{47a,47b}, M. Stratmann ¹⁷²,
 M. Strauss ¹²¹, T. Strebler ¹⁰³, P. Strizenec ^{28b}, R. Ströhmer ¹⁶⁷, D.M. Strom ¹²⁴,
 R. Stroynowski ⁴⁴, A. Strubig ^{47a,47b}, S.A. Stucci ²⁹, B. Stugu ¹⁶, J. Stupak ¹²¹, N.A. Styles ⁴⁸,
 D. Su ¹⁴⁴, S. Su ^{62a}, W. Su ^{62d}, X. Su ^{62a}, D. Suchy ^{28a}, K. Sugizaki ¹⁵⁴, V.V. Sulin ³⁷,
 M.J. Sullivan ⁹³, D.M.S. Sultan ¹²⁷, L. Sultanaliyeva ³⁷, S. Sultansoy ^{3b}, T. Sumida ⁸⁸,
 S. Sun ¹⁰⁷, S. Sun ¹⁷¹, O. Sunneborn Gudnadottir ¹⁶², N. Sur ¹⁰³, M.R. Sutton ¹⁴⁷,
 H. Suzuki ¹⁵⁸, M. Svatos ¹³², M. Swiatlowski ^{157a}, T. Swirski ¹⁶⁷, I. Sykora ^{28a}, M. Sykora ¹³⁴,
 T. Sykora ¹³⁴, D. Ta ¹⁰¹, K. Tackmann ^{48,s}, A. Taffard ¹⁶⁰, R. Tafirout ^{157a},
 J.S. Tafoya Vargas ⁶⁶, Y. Takubo ⁸⁴, M. Talby ¹⁰³, A.A. Talyshv ³⁷, K.C. Tam ^{64b},
 N.M. Tamir ¹⁵², A. Tanaka ¹⁵⁴, J. Tanaka ¹⁵⁴, R. Tanaka ⁶⁶, M. Tanasini ¹⁴⁶, Z. Tao ¹⁶⁵,
 S. Tapia Araya ^{138f}, S. Tapprogge ¹⁰¹, A. Tarek Abouelfadl Mohamed ¹⁰⁸, S. Tarem ¹⁵¹,
 K. Tariq ^{14a}, G. Tarna ^{27b}, G.F. Tartarelli ^{71a}, M.J. Tartarin ⁹⁰, P. Tas ¹³⁴, M. Tasevsky ¹³²,
 E. Tassi ^{43b,43a}, A.C. Tate ¹⁶³, G. Tateno ¹⁵⁴, Y. Tayalati ^{35e,u}, G.N. Taylor ¹⁰⁶, W. Taylor ^{157b},
 A.S. Tee ¹⁷¹, R. Teixeira De Lima ¹⁴⁴, P. Teixeira-Dias ⁹⁶, J.J. Teoh ¹⁵⁶, K. Terashi ¹⁵⁴,
 J. Terron ¹⁰⁰, S. Terzo ¹³, M. Testa ⁵³, R.J. Teuscher ^{156,v}, A. Thaler ⁷⁹, O. Theiner ⁵⁶,
 N. Themistokleous ⁵², T. Thevenaux-Pelzer ¹⁰³, O. Thielmann ¹⁷², D.W. Thomas ⁹⁶,
 J.P. Thomas ²⁰, E.A. Thompson ^{17a}, P.D. Thompson ²⁰, E. Thomson ¹²⁹, R.E. Thornberry ⁴⁴,

C. Tian ^{62a}, Y. Tian ⁵⁵, V. Tikhomirov ^{37,a}, Yu.A. Tikhonov ³⁷, S. Timoshenko ³⁷,
 D. Timoshyn ¹³⁴, E.X.L. Ting ¹, P. Tipton ¹⁷³, A. Tishelman-Charny ²⁹, S.H. Tlou ^{33g},
 K. Todome ¹⁵⁵, S. Todorova-Nova ¹³⁴, S. Todt ⁵⁰, L. Toffolin ^{69a,69c}, M. Togawa ⁸⁴, J. Tojo ⁸⁹,
 S. Tokár ^{28a}, K. Tokushuku ⁸⁴, O. Toldaiev ⁶⁸, R. Tombs ³², M. Tomoto ^{84,112},
 L. Tompkins ^{144,1}, K.W. Topolnicki ^{86b}, E. Torrence ¹²⁴, H. Torres ⁹⁰, E. Torró Pastor ¹⁶⁴,
 M. Toscani ³⁰, C. Tosciri ³⁹, M. Tost ¹¹, D.R. Tovey ¹⁴⁰, A. Traet ¹⁶, I.S. Trandafir ^{27b},
 T. Trefzger ¹⁶⁷, A. Tricoli ²⁹, I.M. Trigger ^{157a}, S. Trincaz-Duvoid ¹²⁸, D.A. Trischuk ²⁶,
 B. Trocmé ⁶⁰, L. Truong ^{33c}, M. Trzebinski ⁸⁷, A. Trzupiek ⁸⁷, F. Tsai ¹⁴⁶, M. Tsai ¹⁰⁷,
 A. Tsiamis ^{153,d}, P.V. Tsiarehka ³⁷, S. Tsigaridas ^{157a}, A. Tsirigotis ^{153,q}, V. Tsiskaridze ¹⁵⁶,
 E.G. Tskhadadze ^{150a}, M. Tsopoulou ¹⁵³, Y. Tsujikawa ⁸⁸, I.I. Tsukerman ³⁷, V. Tsulaia ^{17a},
 S. Tsuno ⁸⁴, K. Tsuru ¹¹⁹, D. Tsybychev ¹⁴⁶, Y. Tu ^{64b}, A. Tudorache ^{27b}, V. Tudorache ^{27b},
 A.N. Tuna ⁶¹, S. Turchikhin ^{57b,57a}, I. Turk Cakir ^{3a}, R. Turra ^{71a}, T. Turtuvshin ^{38,w},
 P.M. Tuts ⁴¹, S. Tzamarias ^{153,d}, E. Tzovara ¹⁰¹, F. Ukegawa ¹⁵⁸, P.A. Ulloa Poblete ^{138c,138b},
 E.N. Umaka ²⁹, G. Unal ³⁶, A. Undrus ²⁹, G. Unel ¹⁶⁰, J. Urban ^{28b}, P. Urrejola ^{138a},
 G. Usai ⁸, R. Ushioda ¹⁵⁵, M. Usman ¹⁰⁹, Z. Uysal ⁸², V. Vacek ¹³³, B. Vachon ¹⁰⁵,
 T. Vafeiadis ³⁶, A. Vaitkus ⁹⁷, C. Valderanis ¹¹⁰, E. Valdes Santurio ^{47a,47b}, M. Valente ^{157a},
 S. Valentinetti ^{23b,23a}, A. Valero ¹⁶⁴, E. Valiente Moreno ¹⁶⁴, A. Vallier ⁹⁰, J.A. Valls Ferrer ¹⁶⁴,
 D.R. Van Arneman ¹¹⁵, T.R. Van Daalen ¹³⁹, A. Van Der Graaf ⁴⁹, P. Van Gemmeren ⁶,
 M. Van Rijnbach ³⁶, S. Van Stroud ⁹⁷, I. Van Vulpen ¹¹⁵, P. Vana ¹³⁴, M. Vanadia ^{76a,76b},
 W. Vandelli ³⁶, E.R. Vandewall ¹²², D. Vannicola ¹⁵², L. Vannoli ⁵³, R. Vari ^{75a}, E.W. Varnes ⁷,
 C. Varni ^{17b}, T. Varol ¹⁴⁹, D. Varouchas ⁶⁶, L. Varriale ¹⁶⁴, K.E. Varvell ¹⁴⁸, M.E. Vasile ^{27b},
 L. Vaslin ⁸⁴, G.A. Vasquez ¹⁶⁶, A. Vasyukov ³⁸, R. Vavricka ¹⁰¹, T. Vazquez Schroeder ³⁶,
 J. Veatch ³¹, V. Vecchio ¹⁰², M.J. Veen ¹⁰⁴, I. Veliscek ²⁹, L.M. Veloce ¹⁵⁶, F. Veloso ^{131a,131c},
 S. Veneziano ^{75a}, A. Ventura ^{70a,70b}, S. Ventura Gonzalez ¹³⁶, A. Verbytskyi ¹¹¹,
 M. Verducci ^{74a,74b}, C. Vergis ⁹⁵, M. Verissimo De Araujo ^{83b}, W. Verkerke ¹¹⁵,
 J.C. Vermeulen ¹¹⁵, C. Vernieri ¹⁴⁴, M. Vessella ¹⁰⁴, M.C. Vetterli ^{143,ad}, A. Vgenopoulos ^{153,d},
 N. Viaux Maira ^{138f}, T. Vickey ¹⁴⁰, O.E. Vickey Boeriu ¹⁴⁰, G.H.A. Viehhauser ¹²⁷, L. Vignani ^{63b},
 M. Villa ^{23b,23a}, M. Villaplana Perez ¹⁶⁴, E.M. Villhauer ⁵², E. Vilucchi ⁵³, M.G. Vincter ³⁴,
 A. Visibile ¹¹⁵, C. Vittori ³⁶, I. Vivarelli ^{23b,23a}, E. Voevodina ¹¹¹, F. Vogel ¹¹⁰, J.C. Voigt ⁵⁰,
 P. Vokac ¹³³, Yu. Volkotrub ^{86b}, J. Von Ahnen ⁴⁸, E. Von Toerne ²⁴, B. Vormwald ³⁶,
 V. Vorobel ¹³⁴, K. Vorobev ³⁷, M. Vos ¹⁶⁴, K. Voss ¹⁴², M. Vozak ¹¹⁵, L. Vozdecky ¹²¹,
 N. Vranjes ¹⁵, M. Vranjes Milosavljevic ¹⁵, M. Vreeswijk ¹¹⁵, N.K. Vu ^{62d,62c}, R. Vuillermet ³⁶,
 O. Vujinovic ¹⁰¹, I. Vukotic ³⁹, S. Wada ¹⁵⁸, C. Wagner ¹⁰⁴, J.M. Wagner ^{17a}, W. Wagner ¹⁷²,
 S. Wahdan ¹⁷², H. Wahlberg ⁹¹, M. Wakida ¹¹², J. Walder ¹³⁵, R. Walker ¹¹⁰, W. Walkowiak ¹⁴²,
 A. Wall ¹²⁹, E.J. Wallin ⁹⁹, T. Wamorkar ⁶, A.Z. Wang ¹³⁷, C. Wang ¹⁰¹, C. Wang ¹¹,
 H. Wang ^{17a}, J. Wang ^{64c}, R. Wang ⁶¹, R. Wang ⁶, S.M. Wang ¹⁴⁹, S. Wang ^{62b}, S. Wang ^{14a},
 T. Wang ^{62a}, W.T. Wang ⁸⁰, W. Wang ^{14a}, X. Wang ^{14c}, X. Wang ¹⁶³, X. Wang ^{62c},
 Y. Wang ^{62d}, Y. Wang ^{14c}, Z. Wang ¹⁰⁷, Z. Wang ^{62d,51,62c}, Z. Wang ¹⁰⁷, A. Warburton ¹⁰⁵,
 R.J. Ward ²⁰, N. Warrack ⁵⁹, S. Waterhouse ⁹⁶, A.T. Watson ²⁰, H. Watson ⁵⁹, M.F. Watson ²⁰,
 E. Watton ^{59,135}, G. Watts ¹³⁹, B.M. Waugh ⁹⁷, J.M. Webb ⁵⁴, C. Weber ²⁹, H.A. Weber ¹⁸,
 M.S. Weber ¹⁹, S.M. Weber ^{63a}, C. Wei ^{62a}, Y. Wei ⁵⁴, A.R. Weidberg ¹²⁷, E.J. Weik ¹¹⁸,
 J. Weingarten ⁴⁹, C. Weiser ⁵⁴, C.J. Wells ⁴⁸, T. Wenaus ²⁹, B. Wendland ⁴⁹, T. Wengler ³⁶,
 N.S. Wenke ¹¹¹, N. Wermes ²⁴, M. Wessels ^{63a}, A.M. Wharton ⁹², A.S. White ⁶¹, A. White ⁸,
 M.J. White ¹, D. Whiteson ¹⁶⁰, L. Wickremasinghe ¹²⁵, W. Wiedenmann ¹⁷¹, M. Wielers ¹³⁵,
 C. Wiglesworth ⁴², D.J. Wilbern ¹²¹, H.G. Wilkens ³⁶, J.J.H. Wilkinson ³², D.M. Williams ⁴¹,
 H.H. Williams ¹²⁹, S. Williams ³², S. Willocq ¹⁰⁴, B.J. Wilson ¹⁰², P.J. Windischhofer ³⁹,
 F.I. Winkel ³⁰, F. Winklmeier ¹²⁴, B.T. Winter ⁵⁴, J.K. Winter ¹⁰², M. Wittgen ¹⁴⁴, M. Wobisch ⁹⁸,

T. Wojtkowski⁶⁰, Z. Wolffs¹¹⁵, J. Wollrath¹⁶⁰, M.W. Wolter⁸⁷, H. Wolters^{131a,131c}, M.C. Wong¹³⁷, E.L. Woodward⁴¹, S.D. Worm⁴⁸, B.K. Wosiek⁸⁷, K.W. Woźniak⁸⁷, S. Wozniowski⁵⁵, K. Wraight⁵⁹, C. Wu²⁰, M. Wu^{14d}, M. Wu¹¹⁴, S.L. Wu¹⁷¹, X. Wu⁵⁶, Y. Wu^{62a}, Z. Wu⁴, J. Wuerzinger^{111,ab}, T.R. Wyatt¹⁰², B.M. Wynne⁵², S. Xella⁴², L. Xia^{14c}, M. Xia^{14b}, J. Xiang^{64c}, M. Xie^{62a}, S. Xin^{14a,14e}, A. Xiong¹²⁴, J. Xiong^{17a}, D. Xu^{14a}, H. Xu^{62a}, L. Xu^{62a}, R. Xu¹²⁹, T. Xu¹⁰⁷, Y. Xu^{14b}, Z. Xu⁵², Z. Xu^{14c}, B. Yabsley¹⁴⁸, S. Yacoob^{33a}, Y. Yamaguchi¹⁵⁵, E. Yamashita¹⁵⁴, H. Yamauchi¹⁵⁸, T. Yamazaki^{17a}, Y. Yamazaki⁸⁵, J. Yan^{62c}, S. Yan⁵⁹, Z. Yan¹⁰⁴, H.J. Yang^{62c,62d}, H.T. Yang^{62a}, S. Yang^{62a}, T. Yang^{64c}, X. Yang³⁶, X. Yang^{14a}, Y. Yang⁴⁴, Y. Yang^{62a}, Z. Yang^{62a}, W-M. Yao^{17a}, H. Ye^{14c}, H. Ye⁵⁵, J. Ye^{14a}, S. Ye²⁹, X. Ye^{62a}, Y. Yeh⁹⁷, I. Yeletsikh³⁸, B.K. Yeo^{17b}, M.R. Yexley⁹⁷, T.P. Yildirim¹²⁷, P. Yin⁴¹, K. Yorita¹⁶⁹, S. Younas^{27b}, C.J.S. Young³⁶, C. Young¹⁴⁴, C. Yu^{14a,14e}, Y. Yu^{62a}, M. Yuan¹⁰⁷, R. Yuan^{62d,62c}, L. Yue⁹⁷, M. Zaazoua^{62a}, B. Zabinski⁸⁷, E. Zaid⁵², Z.K. Zak⁸⁷, T. Zakareishvili¹⁶⁴, N. Zakharchuk³⁴, S. Zambito⁵⁶, J.A. Zamora Saa^{138d,138b}, J. Zang¹⁵⁴, D. Zanzi⁵⁴, O. Zaplatilek¹³³, C. Zeitnitz¹⁷², H. Zeng^{14a}, J.C. Zeng¹⁶³, D.T. Zenger Jr²⁶, O. Zenin³⁷, T. Ženiš^{28a}, S. Zenz⁹⁵, S. Zerradi^{35a}, D. Zerwas⁶⁶, M. Zhai^{14a,14e}, D.F. Zhang¹⁴⁰, J. Zhang^{62b}, J. Zhang⁶, K. Zhang^{14a,14e}, L. Zhang^{62a}, L. Zhang^{14c}, P. Zhang^{14a,14e}, R. Zhang¹⁷¹, S. Zhang¹⁰⁷, S. Zhang⁹⁰, T. Zhang¹⁵⁴, X. Zhang^{62c}, X. Zhang^{62b}, Y. Zhang^{62c}, Y. Zhang⁹⁷, Y. Zhang^{14c}, Z. Zhang^{17a}, Z. Zhang^{62b}, Z. Zhang⁶⁶, H. Zhao¹³⁹, T. Zhao^{62b}, Y. Zhao¹³⁷, Z. Zhao^{62a}, Z. Zhao^{62a}, A. Zhemchugov³⁸, J. Zheng^{14c}, K. Zheng¹⁶³, X. Zheng^{62a}, Z. Zheng¹⁴⁴, D. Zhong¹⁶³, B. Zhou¹⁰⁷, H. Zhou⁷, N. Zhou^{62c}, Y. Zhou^{14b}, Y. Zhou^{14c}, Y. Zhou⁷, C.G. Zhu^{62b}, J. Zhu¹⁰⁷, X. Zhu^{62d}, Y. Zhu^{62c}, Y. Zhu^{62a}, X. Zhuang^{14a}, K. Zhukov³⁷, N.I. Zimine³⁸, J. Zinsser^{63b}, M. Ziolkowski¹⁴², L. Živković¹⁵, A. Zoccoli^{23b,23a}, K. Zoch⁶¹, T.G. Zorbas¹⁴⁰, O. Zormpa⁴⁶, W. Zou⁴¹, L. Zwalinski³⁶.

¹Department of Physics, University of Adelaide, Adelaide; Australia.

²Department of Physics, University of Alberta, Edmonton AB; Canada.

³(^a)Department of Physics, Ankara University, Ankara; (^b)Division of Physics, TOBB University of Economics and Technology, Ankara; Türkiye.

⁴LAPP, Université Savoie Mont Blanc, CNRS/IN2P3, Annecy; France.

⁵APC, Université Paris Cité, CNRS/IN2P3, Paris; France.

⁶High Energy Physics Division, Argonne National Laboratory, Argonne IL; United States of America.

⁷Department of Physics, University of Arizona, Tucson AZ; United States of America.

⁸Department of Physics, University of Texas at Arlington, Arlington TX; United States of America.

⁹Physics Department, National and Kapodistrian University of Athens, Athens; Greece.

¹⁰Physics Department, National Technical University of Athens, Zografou; Greece.

¹¹Department of Physics, University of Texas at Austin, Austin TX; United States of America.

¹²Institute of Physics, Azerbaijan Academy of Sciences, Baku; Azerbaijan.

¹³Institut de Física d'Altes Energies (IFAE), Barcelona Institute of Science and Technology, Barcelona; Spain.

¹⁴(^a)Institute of High Energy Physics, Chinese Academy of Sciences, Beijing; (^b)Physics Department, Tsinghua University, Beijing; (^c)Department of Physics, Nanjing University, Nanjing; (^d)School of Science, Shenzhen Campus of Sun Yat-sen University; (^e)University of Chinese Academy of Science (UCAS), Beijing; China.

¹⁵Institute of Physics, University of Belgrade, Belgrade; Serbia.

¹⁶Department for Physics and Technology, University of Bergen, Bergen; Norway.

¹⁷(^a)Physics Division, Lawrence Berkeley National Laboratory, Berkeley CA; (^b)University of California,

Berkeley CA; United States of America.

¹⁸Institut für Physik, Humboldt Universität zu Berlin, Berlin; Germany.

¹⁹Albert Einstein Center for Fundamental Physics and Laboratory for High Energy Physics, University of Bern, Bern; Switzerland.

²⁰School of Physics and Astronomy, University of Birmingham, Birmingham; United Kingdom.

²¹(^a) Department of Physics, Bogazici University, Istanbul; (^b) Department of Physics Engineering, Gaziantep University, Gaziantep; (^c) Department of Physics, Istanbul University, Istanbul; Türkiye.

²²(^a) Facultad de Ciencias y Centro de Investigaciones, Universidad Antonio Nariño,

Bogotá; (^b) Departamento de Física, Universidad Nacional de Colombia, Bogotá; Colombia.

²³(^a) Dipartimento di Fisica e Astronomia A. Righi, Università di Bologna, Bologna; (^b) INFN Sezione di Bologna; Italy.

²⁴Physikalisches Institut, Universität Bonn, Bonn; Germany.

²⁵Department of Physics, Boston University, Boston MA; United States of America.

²⁶Department of Physics, Brandeis University, Waltham MA; United States of America.

²⁷(^a) Transilvania University of Brasov, Brasov; (^b) Horia Hulubei National Institute of Physics and Nuclear Engineering, Bucharest; (^c) Department of Physics, Alexandru Ioan Cuza University of Iasi, Iasi; (^d) National Institute for Research and Development of Isotopic and Molecular Technologies, Physics Department, Cluj-Napoca; (^e) National University of Science and Technology Politehnica, Bucharest; (^f) West University in Timisoara, Timisoara; (^g) Faculty of Physics, University of Bucharest, Bucharest; Romania.

²⁸(^a) Faculty of Mathematics, Physics and Informatics, Comenius University, Bratislava; (^b) Department of Subnuclear Physics, Institute of Experimental Physics of the Slovak Academy of Sciences, Kosice; Slovak Republic.

²⁹Physics Department, Brookhaven National Laboratory, Upton NY; United States of America.

³⁰Universidad de Buenos Aires, Facultad de Ciencias Exactas y Naturales, Departamento de Física, y CONICET, Instituto de Física de Buenos Aires (IFIBA), Buenos Aires; Argentina.

³¹California State University, CA; United States of America.

³²Cavendish Laboratory, University of Cambridge, Cambridge; United Kingdom.

³³(^a) Department of Physics, University of Cape Town, Cape Town; (^b) iThemba Labs, Western Cape; (^c) Department of Mechanical Engineering Science, University of Johannesburg,

Johannesburg; (^d) National Institute of Physics, University of the Philippines Diliman

(Philippines); (^e) University of South Africa, Department of Physics, Pretoria; (^f) University of Zululand, KwaDlangezwa; (^g) School of Physics, University of the Witwatersrand, Johannesburg; South Africa.

³⁴Department of Physics, Carleton University, Ottawa ON; Canada.

³⁵(^a) Faculté des Sciences Ain Chock, Réseau Universitaire de Physique des Hautes Energies - Université Hassan II, Casablanca; (^b) Faculté des Sciences, Université Ibn-Tofail, Kénitra; (^c) Faculté des Sciences Semlalia, Université Cadi Ayyad, LPHEA-Marrakech; (^d) LPMR, Faculté des Sciences, Université Mohamed Premier, Oujda; (^e) Faculté des sciences, Université Mohammed V, Rabat; (^f) Institute of Applied Physics, Mohammed VI Polytechnic University, Ben Guerir; Morocco.

³⁶CERN, Geneva; Switzerland.

³⁷Affiliated with an institute covered by a cooperation agreement with CERN.

³⁸Affiliated with an international laboratory covered by a cooperation agreement with CERN.

³⁹Enrico Fermi Institute, University of Chicago, Chicago IL; United States of America.

⁴⁰LPC, Université Clermont Auvergne, CNRS/IN2P3, Clermont-Ferrand; France.

⁴¹Nevis Laboratory, Columbia University, Irvington NY; United States of America.

⁴²Niels Bohr Institute, University of Copenhagen, Copenhagen; Denmark.

⁴³(^a) Dipartimento di Fisica, Università della Calabria, Rende; (^b) INFN Gruppo Collegato di Cosenza, Laboratori Nazionali di Frascati; Italy.

- ⁴⁴Physics Department, Southern Methodist University, Dallas TX; United States of America.
- ⁴⁵Physics Department, University of Texas at Dallas, Richardson TX; United States of America.
- ⁴⁶National Centre for Scientific Research "Demokritos", Agia Paraskevi; Greece.
- ⁴⁷(^a) Department of Physics, Stockholm University; (^b) Oskar Klein Centre, Stockholm; Sweden.
- ⁴⁸Deutsches Elektronen-Synchrotron DESY, Hamburg and Zeuthen; Germany.
- ⁴⁹Fakultät Physik, Technische Universität Dortmund, Dortmund; Germany.
- ⁵⁰Institut für Kern- und Teilchenphysik, Technische Universität Dresden, Dresden; Germany.
- ⁵¹Department of Physics, Duke University, Durham NC; United States of America.
- ⁵²SUPA - School of Physics and Astronomy, University of Edinburgh, Edinburgh; United Kingdom.
- ⁵³INFN e Laboratori Nazionali di Frascati, Frascati; Italy.
- ⁵⁴Physikalisches Institut, Albert-Ludwigs-Universität Freiburg, Freiburg; Germany.
- ⁵⁵II. Physikalisches Institut, Georg-August-Universität Göttingen, Göttingen; Germany.
- ⁵⁶Département de Physique Nucléaire et Corpusculaire, Université de Genève, Genève; Switzerland.
- ⁵⁷(^a) Dipartimento di Fisica, Università di Genova, Genova; (^b) INFN Sezione di Genova; Italy.
- ⁵⁸II. Physikalisches Institut, Justus-Liebig-Universität Giessen, Giessen; Germany.
- ⁵⁹SUPA - School of Physics and Astronomy, University of Glasgow, Glasgow; United Kingdom.
- ⁶⁰LPSC, Université Grenoble Alpes, CNRS/IN2P3, Grenoble INP, Grenoble; France.
- ⁶¹Laboratory for Particle Physics and Cosmology, Harvard University, Cambridge MA; United States of America.
- ⁶²(^a) Department of Modern Physics and State Key Laboratory of Particle Detection and Electronics, University of Science and Technology of China, Hefei; (^b) Institute of Frontier and Interdisciplinary Science and Key Laboratory of Particle Physics and Particle Irradiation (MOE), Shandong University, Qingdao; (^c) School of Physics and Astronomy, Shanghai Jiao Tong University, Key Laboratory for Particle Astrophysics and Cosmology (MOE), SKLPPC, Shanghai; (^d) Tsung-Dao Lee Institute, Shanghai; (^e) School of Physics and Microelectronics, Zhengzhou University; China.
- ⁶³(^a) Kirchhoff-Institut für Physik, Ruprecht-Karls-Universität Heidelberg, Heidelberg; (^b) Physikalisches Institut, Ruprecht-Karls-Universität Heidelberg, Heidelberg; Germany.
- ⁶⁴(^a) Department of Physics, Chinese University of Hong Kong, Shatin, N.T., Hong Kong; (^b) Department of Physics, University of Hong Kong, Hong Kong; (^c) Department of Physics and Institute for Advanced Study, Hong Kong University of Science and Technology, Clear Water Bay, Kowloon, Hong Kong; China.
- ⁶⁵Department of Physics, National Tsing Hua University, Hsinchu; Taiwan.
- ⁶⁶IJCLab, Université Paris-Saclay, CNRS/IN2P3, 91405, Orsay; France.
- ⁶⁷Centro Nacional de Microelectrónica (IMB-CNM-CSIC), Barcelona; Spain.
- ⁶⁸Department of Physics, Indiana University, Bloomington IN; United States of America.
- ⁶⁹(^a) INFN Gruppo Collegato di Udine, Sezione di Trieste, Udine; (^b) ICTP, Trieste; (^c) Dipartimento Politecnico di Ingegneria e Architettura, Università di Udine, Udine; Italy.
- ⁷⁰(^a) INFN Sezione di Lecce; (^b) Dipartimento di Matematica e Fisica, Università del Salento, Lecce; Italy.
- ⁷¹(^a) INFN Sezione di Milano; (^b) Dipartimento di Fisica, Università di Milano, Milano; Italy.
- ⁷²(^a) INFN Sezione di Napoli; (^b) Dipartimento di Fisica, Università di Napoli, Napoli; Italy.
- ⁷³(^a) INFN Sezione di Pavia; (^b) Dipartimento di Fisica, Università di Pavia, Pavia; Italy.
- ⁷⁴(^a) INFN Sezione di Pisa; (^b) Dipartimento di Fisica E. Fermi, Università di Pisa, Pisa; Italy.
- ⁷⁵(^a) INFN Sezione di Roma; (^b) Dipartimento di Fisica, Sapienza Università di Roma, Roma; Italy.
- ⁷⁶(^a) INFN Sezione di Roma Tor Vergata; (^b) Dipartimento di Fisica, Università di Roma Tor Vergata, Roma; Italy.
- ⁷⁷(^a) INFN Sezione di Roma Tre; (^b) Dipartimento di Matematica e Fisica, Università Roma Tre, Roma; Italy.
- ⁷⁸(^a) INFN-TIFPA; (^b) Università degli Studi di Trento, Trento; Italy.

- ⁷⁹Universität Innsbruck, Department of Astro and Particle Physics, Innsbruck; Austria.
- ⁸⁰University of Iowa, Iowa City IA; United States of America.
- ⁸¹Department of Physics and Astronomy, Iowa State University, Ames IA; United States of America.
- ⁸²Istinye University, Sariyer, Istanbul; Türkiye.
- ⁸³(^a) Departamento de Engenharia Elétrica, Universidade Federal de Juiz de Fora (UFJF), Juiz de Fora; (^b) Universidade Federal do Rio De Janeiro COPPE/EE/IF, Rio de Janeiro; (^c) Instituto de Física, Universidade de São Paulo, São Paulo; (^d) Rio de Janeiro State University, Rio de Janeiro; (^e) Federal University of Bahia, Bahia; Brazil.
- ⁸⁴KEK, High Energy Accelerator Research Organization, Tsukuba; Japan.
- ⁸⁵Graduate School of Science, Kobe University, Kobe; Japan.
- ⁸⁶(^a) AGH University of Krakow, Faculty of Physics and Applied Computer Science, Krakow; (^b) Marian Smoluchowski Institute of Physics, Jagiellonian University, Krakow; Poland.
- ⁸⁷Institute of Nuclear Physics Polish Academy of Sciences, Krakow; Poland.
- ⁸⁸Faculty of Science, Kyoto University, Kyoto; Japan.
- ⁸⁹Research Center for Advanced Particle Physics and Department of Physics, Kyushu University, Fukuoka ; Japan.
- ⁹⁰L2IT, Université de Toulouse, CNRS/IN2P3, UPS, Toulouse; France.
- ⁹¹Instituto de Física La Plata, Universidad Nacional de La Plata and CONICET, La Plata; Argentina.
- ⁹²Physics Department, Lancaster University, Lancaster; United Kingdom.
- ⁹³Oliver Lodge Laboratory, University of Liverpool, Liverpool; United Kingdom.
- ⁹⁴Department of Experimental Particle Physics, Jožef Stefan Institute and Department of Physics, University of Ljubljana, Ljubljana; Slovenia.
- ⁹⁵School of Physics and Astronomy, Queen Mary University of London, London; United Kingdom.
- ⁹⁶Department of Physics, Royal Holloway University of London, Egham; United Kingdom.
- ⁹⁷Department of Physics and Astronomy, University College London, London; United Kingdom.
- ⁹⁸Louisiana Tech University, Ruston LA; United States of America.
- ⁹⁹Fysiska institutionen, Lunds universitet, Lund; Sweden.
- ¹⁰⁰Departamento de Física Teórica C-15 and CIAFF, Universidad Autónoma de Madrid, Madrid; Spain.
- ¹⁰¹Institut für Physik, Universität Mainz, Mainz; Germany.
- ¹⁰²School of Physics and Astronomy, University of Manchester, Manchester; United Kingdom.
- ¹⁰³CPPM, Aix-Marseille Université, CNRS/IN2P3, Marseille; France.
- ¹⁰⁴Department of Physics, University of Massachusetts, Amherst MA; United States of America.
- ¹⁰⁵Department of Physics, McGill University, Montreal QC; Canada.
- ¹⁰⁶School of Physics, University of Melbourne, Victoria; Australia.
- ¹⁰⁷Department of Physics, University of Michigan, Ann Arbor MI; United States of America.
- ¹⁰⁸Department of Physics and Astronomy, Michigan State University, East Lansing MI; United States of America.
- ¹⁰⁹Group of Particle Physics, University of Montreal, Montreal QC; Canada.
- ¹¹⁰Fakultät für Physik, Ludwig-Maximilians-Universität München, München; Germany.
- ¹¹¹Max-Planck-Institut für Physik (Werner-Heisenberg-Institut), München; Germany.
- ¹¹²Graduate School of Science and Kobayashi-Maskawa Institute, Nagoya University, Nagoya; Japan.
- ¹¹³Department of Physics and Astronomy, University of New Mexico, Albuquerque NM; United States of America.
- ¹¹⁴Institute for Mathematics, Astrophysics and Particle Physics, Radboud University/Nikhef, Nijmegen; Netherlands.
- ¹¹⁵Nikhef National Institute for Subatomic Physics and University of Amsterdam, Amsterdam; Netherlands.

- ¹¹⁶Department of Physics, Northern Illinois University, DeKalb IL; United States of America.
- ¹¹⁷^(a)New York University Abu Dhabi, Abu Dhabi;^(b)United Arab Emirates University, Al Ain; United Arab Emirates.
- ¹¹⁸Department of Physics, New York University, New York NY; United States of America.
- ¹¹⁹Ochanomizu University, Otsuka, Bunkyo-ku, Tokyo; Japan.
- ¹²⁰Ohio State University, Columbus OH; United States of America.
- ¹²¹Homer L. Dodge Department of Physics and Astronomy, University of Oklahoma, Norman OK; United States of America.
- ¹²²Department of Physics, Oklahoma State University, Stillwater OK; United States of America.
- ¹²³Palacký University, Joint Laboratory of Optics, Olomouc; Czech Republic.
- ¹²⁴Institute for Fundamental Science, University of Oregon, Eugene, OR; United States of America.
- ¹²⁵Graduate School of Science, Osaka University, Osaka; Japan.
- ¹²⁶Department of Physics, University of Oslo, Oslo; Norway.
- ¹²⁷Department of Physics, Oxford University, Oxford; United Kingdom.
- ¹²⁸LPNHE, Sorbonne Université, Université Paris Cité, CNRS/IN2P3, Paris; France.
- ¹²⁹Department of Physics, University of Pennsylvania, Philadelphia PA; United States of America.
- ¹³⁰Department of Physics and Astronomy, University of Pittsburgh, Pittsburgh PA; United States of America.
- ¹³¹^(a)Laboratório de Instrumentação e Física Experimental de Partículas - LIP, Lisboa;^(b)Departamento de Física, Faculdade de Ciências, Universidade de Lisboa, Lisboa;^(c)Departamento de Física, Universidade de Coimbra, Coimbra;^(d)Centro de Física Nuclear da Universidade de Lisboa, Lisboa;^(e)Departamento de Física, Universidade do Minho, Braga;^(f)Departamento de Física Teórica y del Cosmos, Universidad de Granada, Granada (Spain);^(g)Departamento de Física, Instituto Superior Técnico, Universidade de Lisboa, Lisboa; Portugal.
- ¹³²Institute of Physics of the Czech Academy of Sciences, Prague; Czech Republic.
- ¹³³Czech Technical University in Prague, Prague; Czech Republic.
- ¹³⁴Charles University, Faculty of Mathematics and Physics, Prague; Czech Republic.
- ¹³⁵Particle Physics Department, Rutherford Appleton Laboratory, Didcot; United Kingdom.
- ¹³⁶IRFU, CEA, Université Paris-Saclay, Gif-sur-Yvette; France.
- ¹³⁷Santa Cruz Institute for Particle Physics, University of California Santa Cruz, Santa Cruz CA; United States of America.
- ¹³⁸^(a)Departamento de Física, Pontificia Universidad Católica de Chile, Santiago;^(b)Millennium Institute for Subatomic physics at high energy frontier (SAPHIR), Santiago;^(c)Instituto de Investigación Multidisciplinario en Ciencia y Tecnología, y Departamento de Física, Universidad de La Serena;^(d)Universidad Andres Bello, Department of Physics, Santiago;^(e)Instituto de Alta Investigación, Universidad de Tarapacá, Arica;^(f)Departamento de Física, Universidad Técnica Federico Santa María, Valparaíso; Chile.
- ¹³⁹Department of Physics, University of Washington, Seattle WA; United States of America.
- ¹⁴⁰Department of Physics and Astronomy, University of Sheffield, Sheffield; United Kingdom.
- ¹⁴¹Department of Physics, Shinshu University, Nagano; Japan.
- ¹⁴²Department Physik, Universität Siegen, Siegen; Germany.
- ¹⁴³Department of Physics, Simon Fraser University, Burnaby BC; Canada.
- ¹⁴⁴SLAC National Accelerator Laboratory, Stanford CA; United States of America.
- ¹⁴⁵Department of Physics, Royal Institute of Technology, Stockholm; Sweden.
- ¹⁴⁶Departments of Physics and Astronomy, Stony Brook University, Stony Brook NY; United States of America.
- ¹⁴⁷Department of Physics and Astronomy, University of Sussex, Brighton; United Kingdom.

- ¹⁴⁸School of Physics, University of Sydney, Sydney; Australia.
- ¹⁴⁹Institute of Physics, Academia Sinica, Taipei; Taiwan.
- ¹⁵⁰^(a)E. Andronikashvili Institute of Physics, Iv. Javakhishvili Tbilisi State University, Tbilisi; ^(b)High Energy Physics Institute, Tbilisi State University, Tbilisi; ^(c)University of Georgia, Tbilisi; Georgia.
- ¹⁵¹Department of Physics, Technion, Israel Institute of Technology, Haifa; Israel.
- ¹⁵²Raymond and Beverly Sackler School of Physics and Astronomy, Tel Aviv University, Tel Aviv; Israel.
- ¹⁵³Department of Physics, Aristotle University of Thessaloniki, Thessaloniki; Greece.
- ¹⁵⁴International Center for Elementary Particle Physics and Department of Physics, University of Tokyo, Tokyo; Japan.
- ¹⁵⁵Department of Physics, Tokyo Institute of Technology, Tokyo; Japan.
- ¹⁵⁶Department of Physics, University of Toronto, Toronto ON; Canada.
- ¹⁵⁷^(a)TRIUMF, Vancouver BC; ^(b)Department of Physics and Astronomy, York University, Toronto ON; Canada.
- ¹⁵⁸Division of Physics and Tomonaga Center for the History of the Universe, Faculty of Pure and Applied Sciences, University of Tsukuba, Tsukuba; Japan.
- ¹⁵⁹Department of Physics and Astronomy, Tufts University, Medford MA; United States of America.
- ¹⁶⁰Department of Physics and Astronomy, University of California Irvine, Irvine CA; United States of America.
- ¹⁶¹University of Sharjah, Sharjah; United Arab Emirates.
- ¹⁶²Department of Physics and Astronomy, University of Uppsala, Uppsala; Sweden.
- ¹⁶³Department of Physics, University of Illinois, Urbana IL; United States of America.
- ¹⁶⁴Instituto de Física Corpuscular (IFIC), Centro Mixto Universidad de Valencia - CSIC, Valencia; Spain.
- ¹⁶⁵Department of Physics, University of British Columbia, Vancouver BC; Canada.
- ¹⁶⁶Department of Physics and Astronomy, University of Victoria, Victoria BC; Canada.
- ¹⁶⁷Fakultät für Physik und Astronomie, Julius-Maximilians-Universität Würzburg, Würzburg; Germany.
- ¹⁶⁸Department of Physics, University of Warwick, Coventry; United Kingdom.
- ¹⁶⁹Waseda University, Tokyo; Japan.
- ¹⁷⁰Department of Particle Physics and Astrophysics, Weizmann Institute of Science, Rehovot; Israel.
- ¹⁷¹Department of Physics, University of Wisconsin, Madison WI; United States of America.
- ¹⁷²Fakultät für Mathematik und Naturwissenschaften, Fachgruppe Physik, Bergische Universität Wuppertal, Wuppertal; Germany.
- ¹⁷³Department of Physics, Yale University, New Haven CT; United States of America.
- ^a Also Affiliated with an institute covered by a cooperation agreement with CERN.
- ^b Also at An-Najah National University, Nablus; Palestine.
- ^c Also at Borough of Manhattan Community College, City University of New York, New York NY; United States of America.
- ^d Also at Center for Interdisciplinary Research and Innovation (CIRI-AUTH), Thessaloniki; Greece.
- ^e Also at Centro Studi e Ricerche Enrico Fermi; Italy.
- ^f Also at CERN, Geneva; Switzerland.
- ^g Also at Département de Physique Nucléaire et Corpusculaire, Université de Genève, Genève; Switzerland.
- ^h Also at Departament de Física de la Universitat Autònoma de Barcelona, Barcelona; Spain.
- ⁱ Also at Department of Financial and Management Engineering, University of the Aegean, Chios; Greece.
- ^j Also at Department of Physics, California State University, Sacramento; United States of America.
- ^k Also at Department of Physics, King's College London, London; United Kingdom.
- ^l Also at Department of Physics, Stanford University, Stanford CA; United States of America.
- ^m Also at Department of Physics, Stellenbosch University; South Africa.

- ⁿ Also at Department of Physics, University of Fribourg, Fribourg; Switzerland.
- ^o Also at Department of Physics, University of Thessaly; Greece.
- ^p Also at Department of Physics, Westmont College, Santa Barbara; United States of America.
- ^q Also at Hellenic Open University, Patras; Greece.
- ^r Also at Institutio Catalana de Recerca i Estudis Avancats, ICREA, Barcelona; Spain.
- ^s Also at Institut für Experimentalphysik, Universität Hamburg, Hamburg; Germany.
- ^t Also at Institute for Nuclear Research and Nuclear Energy (INRNE) of the Bulgarian Academy of Sciences, Sofia; Bulgaria.
- ^u Also at Institute of Applied Physics, Mohammed VI Polytechnic University, Ben Guerir; Morocco.
- ^v Also at Institute of Particle Physics (IPP); Canada.
- ^w Also at Institute of Physics and Technology, Mongolian Academy of Sciences, Ulaanbaatar; Mongolia.
- ^x Also at Institute of Physics, Azerbaijan Academy of Sciences, Baku; Azerbaijan.
- ^y Also at Institute of Theoretical Physics, Ilia State University, Tbilisi; Georgia.
- ^z Also at Lawrence Livermore National Laboratory, Livermore; United States of America.
- ^{aa} Also at National Institute of Physics, University of the Philippines Diliman (Philippines); Philippines.
- ^{ab} Also at Technical University of Munich, Munich; Germany.
- ^{ac} Also at The Collaborative Innovation Center of Quantum Matter (CICQM), Beijing; China.
- ^{ad} Also at TRIUMF, Vancouver BC; Canada.
- ^{ae} Also at Università di Napoli Parthenope, Napoli; Italy.
- ^{af} Also at University of Colorado Boulder, Department of Physics, Colorado; United States of America.
- ^{ag} Also at Washington College, Chestertown, MD; United States of America.
- ^{ah} Also at Yeditepe University, Physics Department, Istanbul; Türkiye.
- * Deceased